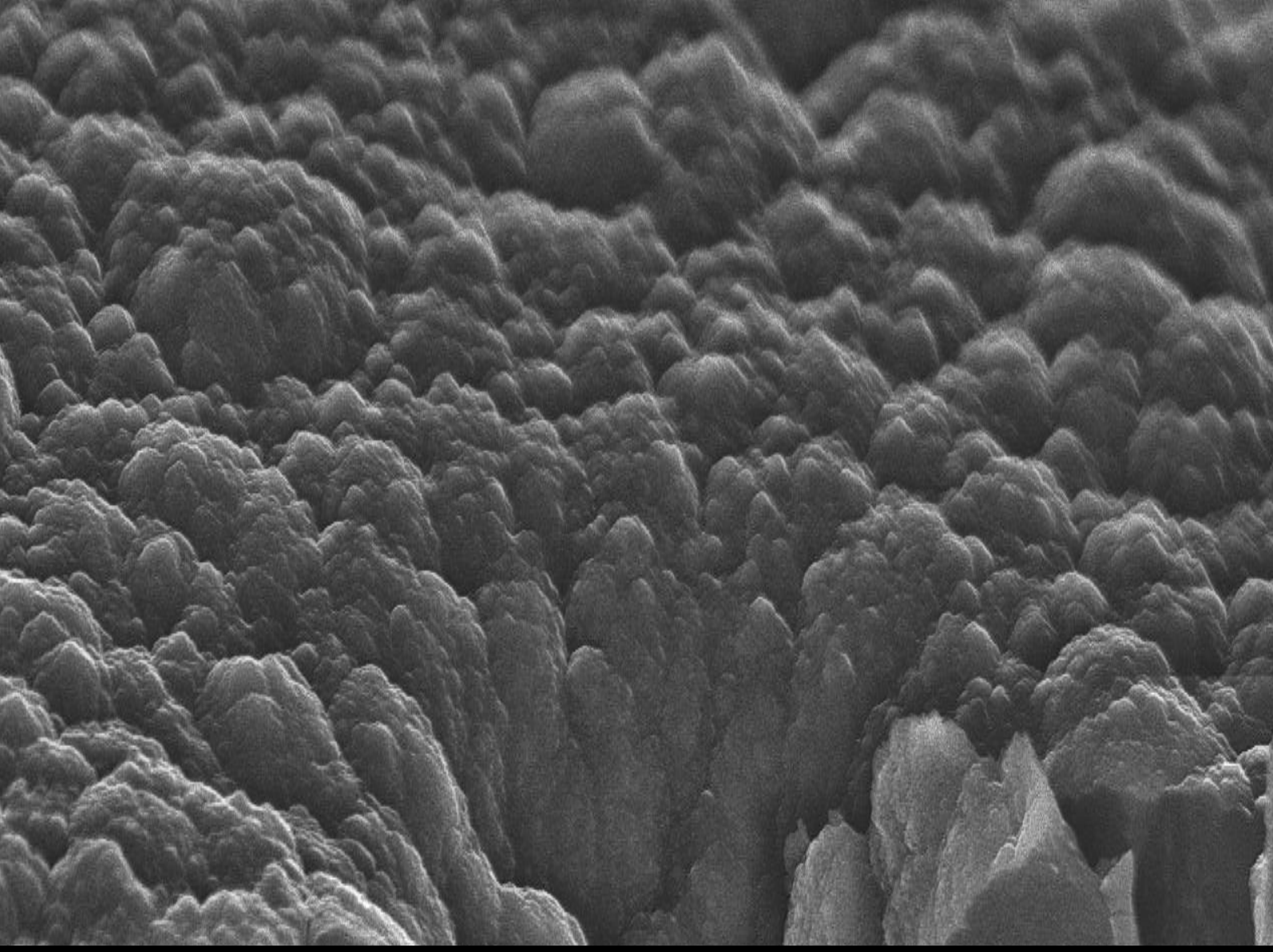

Thin-film silicon solar cells

Optimization of material, architecture and texture

Sriram Sambamurthy

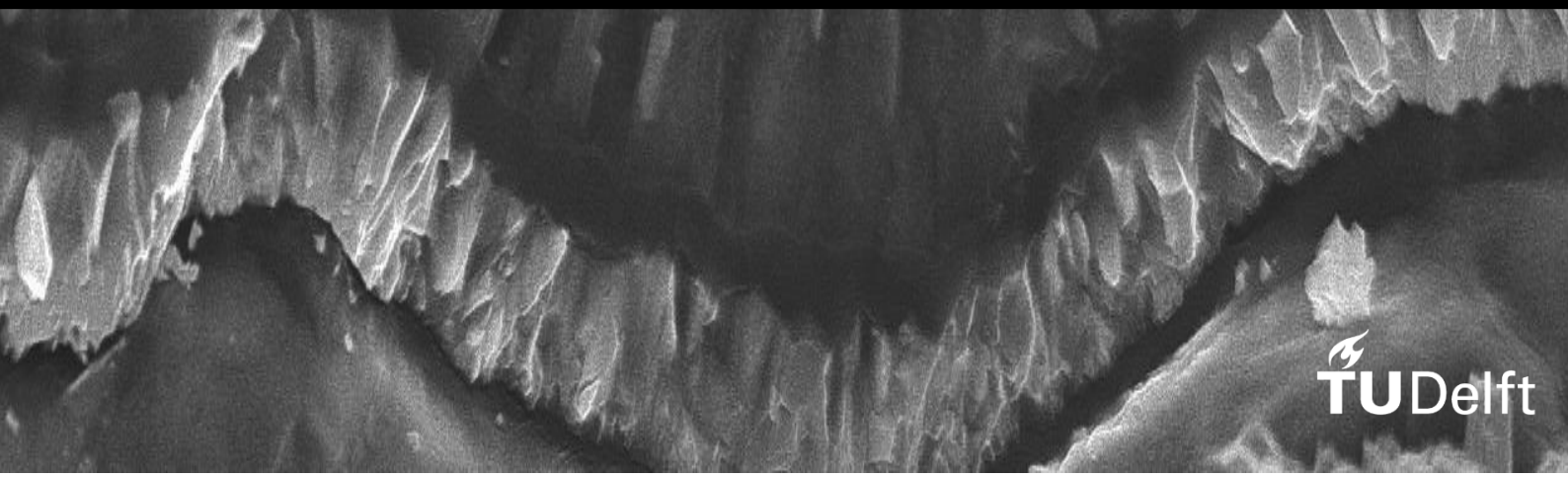

Thin-film silicon solar cells: Optimization of material, architecture and texture

by

Sriram Sambamurthy

to obtain the degree of Master of Science
at the Delft University of Technology,

Student number:	5245125	
Project duration:	November 8, 2021 – August 17, 2022	
Thesis committee:	Prof. Dr. A.H.M. Smets,	TU Delft, PVMD supervisor
	Prof. Dr. Luana Mazzarella,	TU Delft, ESE - PVMD
	Dr. ir.. R. Chandra Mouli,	TU Delft, DCE&S
	Dr. Thierry de Vrijer,	TU Delft, daily supervisor
	Dr. G. Limodio,	TU Delft, daily supervisor

An electronic version of this thesis is available at `http://repository.tudelft.nl/`.

TU Delft Delft University of Technology

PVMD Delft University of Technology

HyET Solar Flexible light weight solar modules

Abstract

The world is in need for an energy transition from the usage of fossil fuels to renewable energy source to reduce the harmful effects climate and health. Focusing on accelerating the research and development of photovoltaic technologies is an important step towards energy transition. The thin-film silicon solar modules has shown a great potential and a high market prospect. It is flexible, light-weight and also has a low manufacturing and installation cost. It is used for solar pumps and building integration. However, the highest initial conversion efficiency for a micromorph is 14.8%. Thus, we focus on further optimizing the multi-junction solar cells to reach higher efficiency by focusing on the improving the p-layer, texturing and silicon oxide intermediate reflector(SOIR). Further, standardised and error-free external quantum efficiency (EQE) measurement was done to obtain reliable J_{sc} values.
This work introduces deposition of single, micromorph and triple-junction thin-film solar cells on glass and wafers. The experiments were designed to study the effects of varying the material, thickness of the p-layer and n-SiOx reflective layer and textures of the solar cells. The J_{sc} from the EQE, V_{oc}, FF and efficiency were the main parameters used to analyse the results.

The J_{sc} from the EQE measurement was not reliable as the EQE had an artifact while measuring micromorph devices. It was solved by increasing the bias light intensity and decreasing probe light intensity. The forward voltage bias was also found to be important for a cell with low shunt resistance and to measure the target cell in short circuit condition. The standard bias lights to be used are 1-3 to bias the top cell and 7-8 to bias the bottom cell combined with 50% reduction in the probe light intensity.

After correcting the EQE, the optimization of the top cell p-layer was performed on a-Si single junction solar cells on Asahi substrates. It was found that both the contact layer and the window layer of the p-layer have a high influence on the performance of the solar cell. A maximum conversion efficiency of 10% and V_{oc} of 910mV were achieved for the a-Si single junction solar cells. Further, it was also found that there is more than one way to reach high efficiency with an optimal p layer by changing the material composition and thickness of both the contact and window layer. Additionally, the insertion of the buffer layer in the i/p interface showed no significant improvement in the performance of the solar cell.

Furthermore, comparison of the performance of textures of different feature sizes was done on solar cells in p-i-n and n-i-p architecture. It was found that the best optoelectronic performance was obtained from asahi and smooth pyramidal textured solar cell in p-i-n and n-i-p configuration repectively in both double and triple junction solar cell. Further, the honeycomb textured substrate with R_{rms} around 270nm is not suitable to deposit on double and triple junction solar cell as it resulted in shunted cells.

Finally, the SOIR can be used in a-Si/nc-Si/nc-Si triple junction solar cell to divide current within middle and bottom junctions. The reflection of light in the infrared region increases with the thickness of the SOIR layer. A thick 90nm n-SiOx layer with F_{B2H6}=3.2sccm gives the best electrical performance and current distribution property for a micromorph.

Acknowledgement

"Full maturity is to find what you lost as a child and regain it." *(some wise guy)*

It has been a two-year long journey. I have learned a lot during this journey. The main aspect that kept me invested in this master's program is the curiosity to learn and acquire new knowledge. I realized how fun science is and to find out why some things happen or work. This master's program has helped me get a deeper understanding of science.

I would like to thank the Delft University of Technology for giving me this wonderful opportunity to explore and learn. I would also like to thank Prof. Dr. Arno Smets for being my supervisor, I love that you are always excited and inquisitive about science and solar cells. Your energy is contagious and has kept me motivated throughout the thesis.

Dr. Thierry de Vrijer, I always enjoyed the conversations with you as you tend to spill some knowledge from your vast reservoir and I always try to stay attentive to grab at least 20% of what you spill. Thank you for being an inspiration, and thank you for supporting me and guiding me till the end. I still have a lot to learn from you.

Dr. Gianluca Limodio, thank you for always being kind and supportive throughout the journey. Thank you for teaching me and making me understand the concepts involved in my thesis. I am thankful for a wonderful collaboration with Govind Padmakumar during my thesis. Thank you Govind and Federica, you were always helpful and very approachable. I always enjoyed our discussions. I would also like to thank the members of HyET company, EKL, and ESP laboratory staff. Working with you was a pleasure.

Sriram Sambamurthy,
Delft, August 2022

Contents

Abstract i

Acknowledgement iii

List of Figures vii

List of Tables xi

1 Introduction 1
- 1.1 Why sustainable energy . . . 1
- 1.2 Thin-film solar cells . . . 2
  - 1.2.1 Amorphous and nanocrystalline silicon . . . 3
- 1.3 Collaboration with HyET solar . . . 4
- 1.4 Research gaps . . . 4
- 1.5 Research questions . . . 5
- 1.6 Report Outline . . . 6

2 Fundamentals 7
- 2.1 Solar cell . . . 7
  - 2.1.1 Energy band formation in semiconductors . . . 7
  - 2.1.2 Generation of charge carriers . . . 8
  - 2.1.3 Separation of charge carriers . . . 8
  - 2.1.4 Collection of charge carriers . . . 8
- 2.2 Optics of flat interfaces . . . 9
- 2.3 Current and voltage characteristics of a solar cell . . . 10
- 2.4 Losses in solar cells . . . 12
- 2.5 Transparent conductive oxide . . . 12
- 2.6 Hydrogenrated Amorphous silicon and nano crystalline silicon . . . 13
- 2.7 Multijunction thin film solar cell . . . 14

3 Deposition and measurement of thin film silicon solar cell 16
- 3.1 Deposition of solar cell layers . . . 16
  - 3.1.1 AMIGO . . . 16
  - 3.1.2 PROVAC . . . 17
- 3.2 Measurement of solar cells . . . 17
  - 3.2.1 WACOM . . . 17
  - 3.2.2 External quantum efficiency setup . . . 17
  - 3.2.3 LAMBDA . . . 18

4 Methodology 19
- 4.1 Substrate configuration . . . 19
  - 4.1.1 Back contact deposition . . . 19
  - 4.1.2 Photo active stack and front contacts . . . 20
- 4.2 Superstrate configuration . . . 21
- 4.3 Texturing of substrates . . . 22

5 EQE study **25**
5.1 The artifact . . . 25
5.2 Measuring the EQE of a micromorph tandem device . . . 25
5.3 The problem . . . 26
5.4 Solutions . . . 27
5.4.1 Bias light experiment . . . 28
5.4.2 Probe light intensity reduction . . . 28
5.4.3 Voltage biasing . . . 29
5.5 Implementation . . . 31

6 Optimization of p-layer **33**
6.1 Introduction of p-layer . . . 33
6.2 Configuration of p-layer and materials used . . . 33
6.3 Experimental details . . . 34
6.4 Results . . . 35
6.4.1 Contact layer thickness and material variation . . . 35
6.4.2 Buffer layer . . . 37
6.4.3 Diborane doping of window layer . . . 38
6.4.4 CO_2 flow rate of window layer . . . 40
6.5 Further optimization of p-layer . . . 43
6.5.1 Contact layer doping series . . . 43

7 Comparison of textures **48**
7.1 Introduction to the textures used . . . 48
7.2 Experimental details . . . 49
7.3 Results . . . 50
7.3.1 p-i-n tandem devices . . . 50
7.3.2 p-i-n triple junction devices . . . 52
7.3.3 n-i-p tandem devices . . . 54
7.3.4 n-i-p triple junction devices . . . 56

8 Silicon oxide intermediate reflector **58**
8.1 Introduction to silicon oxide intermidiate reflector . . . 58
8.2 Results of SOIR study . . . 58
8.2.1 Micromorphs with honeycomb texture . . . 58
8.2.2 Micromorph with smoothened pyramidal texture . . . 60

9 Conclusions and Outlooks **63**
9.1 Conclusions . . . 63
9.2 Future Outlooks . . . 64

Appendices **65**

A Experimental values **66**

Bibliography **73**

List of Figures

1.1 The change in global surface temperature relative to 1951-1980 average temperatures 2
1.2 The energy generated from different renewable sources throughout the world [1] . . . 2
1.3 Architecture of micromorph solar cell 4

2.1 (a) Electron orbitals of silicon atom (b) Band gap states formation in silicon [2] 7
2.2 Generation of electron and hole pair in a solar cell [3] 8
2.3 Collection of photo generated charge carriers from the solar cell[3] 9
2.4 The incident, reflected and transmitted light between two optical interface [3] 9
2.5 IV characteristic curves (red) and Power voltage curve (blue). Isc denotes the short circuit current and Voc denotes the open circuit voltage [4] 10
2.6 Change in current density and voltage with respect to change in series resistance of a solar cell[3] 11
2.7 Change in current density and voltage with respect to change in shunt resistance of a solar cell[3] 11
2.8 Absorption, transmittance and reflection of TCO with respect to wavelength [5] 12
2.9 Phase transition from a-Si to nc-Si with hydrogen dilution [6] 13
2.10 Absorption coefficient of nc-Si, c-Si and a-Si against energy[7] 13

3.1 Schematic diagram of RF magnetron sputtering machine [8] 17
3.2 Schematic diagram of the EQE setup [9] 18
3.3 Integrating sphere inside the Lambda machine[10] 18

4.1 superstrate configuration deposition order 19
4.2 substrate configuration deposition order 19
4.3 tandem n-i-p device 20
4.4 solar cells on wafer and glass in n-i-p configuration 21
4.5 tandem p-i-n device on asahi 22
4.6 A figure with two subfigures 22
4.7 The AFM images of ITO, AZO etched and Hairen tan's substrates 23
4.8 TEM image of a asahi textured glass 24

5.1 The artifacts in EQE measurement of the bottom and top cell of micromorph 25
5.2 The photon flux of each of the bias lights in the EQE setup. 1-8 is the number on the bias light 26
5.3 The photon flux and power of the probe light of the in house EQE setup 27
5.4 Measuring the EQE of the top and bottom junctions of a micromorph solar cell in various bias light combinations 28
5.5 EQE with varying the probe light intensity with bias light 8 for top cell and 1-2 bias light for bottom 28
5.6 EQE measurements with variation in probe light intensity from 10% to 100% with 7-8 bias lights switched on for top cell and 1-2 bias lights switched on for bottom cell . . . 29

5.7 V_{tan} and I_{tan} are the voltage and current of tandem cell. Y-axis is current density(mA/cm^2) and x-axis is the voltage(V). The IV characteristics of micromorph cell Under blue bias light (a) top cell with blue probe light (b) bottom cell with blue probe light (c) top cell with red probe light (d) bottom cell with red probe light.[11] 30
5.8 top and bottom junction EQE measured across various bias voltages with turning on 1-3 bias lights for top junction and 7-8 bias lights for bottom junction 31
5.9 EQE of the top cell(a-Si) with variation in bias light and probe light. The probe light intensity of 30%,50% and 100% is used and bias light turned on are 7-8 and 6-8 for the graph in left and right respectively 31
5.10 EQE of the bottom cell(nc-Si) with variation in probe light intensity and bias lights. The probe light intensities used are 30%,50%,80% and 100% and, bias lights 1-2 and 1-3 are used for the graph in left and right respectively. 32

6.1 p-layer configuration consisting the contact layer, window layer and the buffer layer . 34
6.2 V_{oc}, *FF*, J_{sc} and efficiency with variation in material of contact layer and contact layer thickness (d_con) of 3,6 and 9 nm. The buffer layer is 3nm thick i-Siox and the window layer is p-SiOx with d_{win}=12nm thickness, F_{CO2}=2.2sccm and F_{B2H6}=10sccm 36
6.3 EQE of the single junction amorphous silicons with varying contact layer thickness and material 37
6.4 The photovoltaic optical and electrical performance with variation in buffer layer thickness(d_{buf}) of 3, 6 and 9nm is shown for both intrinsic silicon oxide(i-SiOx) and nano crystalline silicon(i-nc-Si). The contact layer is 3nm thick p-nc-Si the window layer is p-SiOx with d_{win}=12nm thickness, F_{CO2}=2.2sccm and F_{B2H6}=10sccm 38
6.5 The photovoltaic electrical and optical performance of the solar cell with change in the p doping of the window layer, window layer thickness and contact layer thickness. The contact layer is p-nc-Si and $^{win}F_{CO2}$=2.2sccm. The buffer layer is 3nm thick i-Siox. $^{win}F_{B2H6}$ is the diborane flow rate in the window layer and d_{con} and d_{win} are the thicknesses of the contact layer and window layer. 39
6.6 The EQE of the solar cell with varying doping flow rate and thickness of the window layer at constant thickness of buffer and contact layer of 3nm. The buffer and contact layer material used is i-Siox and p-nc-Si. $^{win}F_{B2h6}$ is the dibroane flow rate in the window layer and d_{win} is the thickness of the window layer. 39
6.7 The electrical and optical performance of the solar with change in the p doping of the window layer, window layer thickness and contact layer thickness. The contact layer is p-SiOx and $^{win}F_{CO2}$=2.2sccm. The buffer layer is 3nm thick i-Siox. $^{win}F_{B2H6}$ is the diborane flow rate in the window layer and d_{con} and d_{win} are the thicknesses of the contact layer and window layer. 40
6.8 The variation in the Co_2 flow rate in the window layer with the window layer thickness at $^{win}F_{B2H6}$=10sccm. The buffer layer is 3nm thick i-Siox and the contact layer is p-nc-Si with 3nm thickness. $^{win}F_{CO2}$ is the CO_2 flow rate in the window layer and d_{win} is the thickness of the window layer. 41
6.9 The variation in the Co_2 flow rate of the window layer with the window layer thickness at $^{win}F_{B2H6}$= 30sccm. The seed layer is 3nm thick i-Siox and the contact layer is p-nc-Si with 3nm thickness. $^{win}F_{CO2}$ is the CO_2 flow rate in the window layer and d_{win} is the thickness of the window layer. 42
6.10 EQE of single junction amaorphous silicon cells with varying CO_2 flow rate and thickness of the window layer. Constant diborane flow rate of 30sccm in the window layer and p-Siox as the contact layer. $^{win}F_{CO2}$ is the CO_2 flow rate in the window layer and d_{win} is the thickness of the window layer. 43

6.11 ${}^{win}F_{B2H6}$ and ${}^{con}F_{B2H6}$ are the diborane flowrate in the window layer and contact layer respectively. Variation of ${}^{win}F_{B2H6}$ and ${}^{con}F_{B2H6}$ with optical and electrical performance of the solar cell. d_{con}=3nm and d_{win}=13nm 44
6.12 EQE and absorptance curve of the solar cells with variation in dibronae flow rate of the window and the contact layer. d_{con}=3nm and d_{win}=13nm 44
6.13 ${}^{win}F_{B2H6}$ and ${}^{con}F_{B2H6}$ are the diborane flowrate in the window layer and contact layer respectively. Variation of ${}^{win}F_{B2H6}$ and ${}^{con}F_{B2H6}$ with optical and electrical performance of the solar cell. d_{con}=6nm and d_{win}=10nm 45
6.14 ${}^{win}F_{B2H6}$ and ${}^{con}F_{B2H6}$ are the diborane flowrate in the window layer and contact layer respectively. Variation of ${}^{win}F_{B2H6}$ and ${}^{con}F_{B2H6}$ with optical and electrical performance of the solar cell. d_{con}=8nm and d_{win}=8nm. 46
6.15 EQE and absorptance curve of different thickness fraction of the p-layer with a constant doping flow rate of 30sccm and 60sccm for the window and contact layer respectively 46

7.1 The variation of optical and electronic performance of the miromorph solar cell with Asahi texture, Hairen tan's texture(Ht), ITO etched and AZO etched on glass textures in p-i-n configuration for bottom cell thickness of 1.5μm and 2.5μm 51
7.2 EQE of micromorphs in p-i-n configuration with 1.5μm thick absorber layer of bottom cell on various textures 51
7.3 EQE of micromorphs in p-i-n configuration with 2.5μm thick absorber layer of bottom cell on various textures 52
7.4 The variation in performance of the triple junction solar cell(a-Si/nc-Si/nc-Si) with Asahi, Hairen tan(Ht), ITO etched and AZO etched on glass textures in p-i-n configuration 53
7.5 Comparing the EQE of a-Si/nc-Si/nc-Si solar cells on Asahi, HT, AZO and ITO textured substrates. 53
7.6 The variation in performance of the micromorph solar cell with honeycomb of small period with 12 minutes etched(h12S), honeycomb of large period with 16 minutes etched(h16L), smooth pyramidal with ecthing time of 5(S5), 8(S8) and 11(S11), Hairen tan(Ht), ITO etched and AZO etched on glass textures in n-i-p configuration for bottom cell thickness of 1.5μm and 2.5μm 55
7.7 Comparing the EQE of micromorph solar cells on honeycomb textured substrates with small period etched for 12mins and large period etched for 16mins for i-nc-Si thicknesses of 1.5μm and 2.5μm 55
7.8 Comparing the EQE of micromorph solar cells on honeycomb(H16L), smooth pyramidal(S5,S11) and ITO textured substrates for i-nc-Si thicknesses of 1.5μm and 2.5μm . 56
7.9 The variation in photovoltaic performance of the a-Si/nc-Si/nc-Si triple junction solar cell with honeycomb of small period with 12 minutes etched(h12S), honeycomb of large period with 16 minutes etched(h16L), smooth pyramidal with ecthing time of 5(S5), 8(S8) and 11(S11), Hairen tan textured glass(Ht), ITO etched and AZO etched on glass textures in n-i-p configuration 57

8.1 The variation in photovoltaic performance of the micromorph solar cell on honeycomb textured substrate with CO_2 flow rates of n-SiOx layer of the top cell. Thicknesses of the SOIR layer are 90,30 and 60nm. F_{CO2} is the CO_2 flow rate of the SOIR layer 59
8.2 Comparing the EQEs of micromph solar cell on honeycomb texture having 90nm,60nm and 30nm thick SOIR layer with constant CO_2 flow rate of 2.6sccm 60

8.3 The variation in photovoltaic performance of the micromorph solar cell on smooth pyramidal textured substrate with CO_2 flow rates of n-SiOx layer of the top cell. Thicknesses of the SOIR layer are 90,30 and 60nm. F_{CO2} is the CO_2 flow rate of the SOIR layer 61
8.4 Comparing the EQEs of micromph solar cell on honeycomb texture having 90nm,60nm and 30nm thick SOIR layer with constant CO_2 flow rate of 2.6sccm 62

List of Tables

6.1 The standard deposition conditions of p-layer 34

7.1 The Root-mean-square roughness(R_{rms}) for the Honeycomb texture with large period and 12 minutes etched(H L12), smooth pyramidal texture with etching time of 5, 8 and 11 minutes and ITO and AZO sacrificial texture and the Hairen tan's textured substrate(HT) 50

A.1 solar cell performance of single junction a-Si with different thicknesses(nm), material and flow rate of CO2 and B2H6 (sccm) of contact layer, window layer and buffer layer. The p-SiOx conditions is the conditions of the window layer of the p-layer 67

A.2 shows the values of performance of tandem and triple junction of the solar cell in n-i-p configuration with the textures AZO, ITO, HT, Honeycomb with large period etched for 16min and small period etched for 12mins and smooth pyramidal etched for 5, 8 and 11 mins. The a-si absorber layer thickness is given in 'nm',the i-nc-Si thickness is given in 'μm', the Jsc is given in 'mA/cm^2' and the Rs is the series resitance and Rsh is the shunt resistance and is given in $\Omega.cm^2$ 68

A.3 shows the values of performance of tandem and triple junction the solar cell in p-i-n configuration with the textures AZO, ITO, HT, and asshi glass. The a-si absorber layer thickness is given in 'nm',the i-nc-Si thickness is given in 'μm', the Jsc is given in 'mA/cm^2' and the Rs is the series resitance and Rsh is the shunt resistance and is given in $\Omega.cm^2$ 69

A.4 Photovoltaic performance of micromorph with honeycomb texture. a-Si, nc-Si absorber layer and n-SiOx thickness are given in nm, F_{CO2} is given sccm, Jsc is given in mA/cm^2, Voc is given V, Rs and Rsh are the series and shunt resistance of the cell given in $\Omega.cm^2$ 70

A.5 photovoltaic performance of micromorph with smooth pyramidal texture. a-Si, nc-Si and n-SiOx absorber thickness are given in nm, F_{CO2} is given sccm, Jsc is given in mA/cm^2, Voc is given V, Rs and Rsh are the series and shunt resistance of the cell given in $\Omega.cm^2$ 71

A.6 The total p layer thickness is 16nm,i-a-Si thickness is 280nm and the contact layer p-$SiOx^+$. The contact layer and window layer thickness are given in 'nm',the contact layer diborane flow rate and window layer diborane flow rate are givein in 'sccm', the Voc is given in volts, the Jsc is given in 'mA/cm^2' and the Rs is the series resitance and Rsh is the shunt resistance and is given in $\Omega.cm^2$ 72

1 Introduction

1.1. Why sustainable energy

According to the united nations, the world population will grow from 7 billion in 2011 to 9.3 billion in 2050 [12]. This is approximately a 23% percent increase in population. This increase in population will lead to an alarming increase in energy consumption. In 2022, we are majorly dependent on fossil fuels for energy. Around 80% of the energy demand of the world is still satisfied using fossil fuels[1].

When fossil fuels are burned to acquire energy they emit harmful gases such as carbon dioxide and monoxide and other volatile organic compounds. Globally, almost an excess mortality rate of approximately 3.61 million per year is due to air pollution caused by the usage of fossil fuels [13]. Additionally, the CO_2 and N_2O emitted by the burning of fossil fuels are greenhouse gases. Increase in the concentration of greenhouse gases leads to an increase in the surface temperature of the earth [14]. The greenhouse gases have the property to absorb the radiation in the infrared region, which other elements of the atmosphere do not have [15]. Also, fossil fuels are not renewable, i.e. the material will eventually get depleted after a certain time [16]. To limit the increase in surface temperature caused by fossil fuels there was an agreement between all major nations of the world in 2005. The agreement was to limit the global temperature to $2°C$. However, the Figure 1.1 from NASA, shows the difference in global temperature compared to 1951-1980 temperatures. We can notice a steady increase in temperature from 2000 till 2020. The temperature increase has already reached close to $1\,\mathrm{deg}C$ in 2020. Hence, there is an urgent need to find an alternative source of energy which is sustainable. To reduce or contain the harmful effects on health and climate.

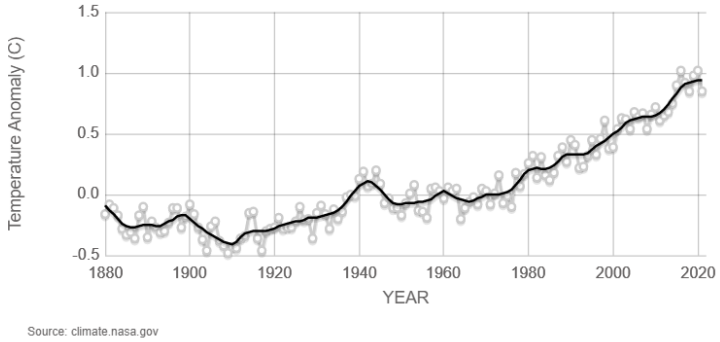

Figure 1.1: The change in global surface temperature relative to 1951-1980 average temperatures

This calls for an energy transition from the usage of fossil fuels to renewable energy source. The main renewable energy sources are solar energy, geothermal energy, wind energy, biomass, Hydropower. Several technologies are being used to utilize renewable energy to change them into a useful form. According to the global energy projections in 2009, wind energy and photovoltaic(PV) will be the most important technologies for renewable energy production by 2040. It was also projected that PV will be the largest source of renewable electricity by 2040 [17]. In Figure 1.2, the energy generation by each renewable source is given. It can be seen that the hydropower slope is decreasing, but usage of solar has just started to increase exponentially near 2008. This is due to an increase in research and a decrease in the cost of Photovoltaic panels per KWh. Hence, focusing on accelerating the installation and research and development of photovoltaic technologies is an important step towards energy transition.

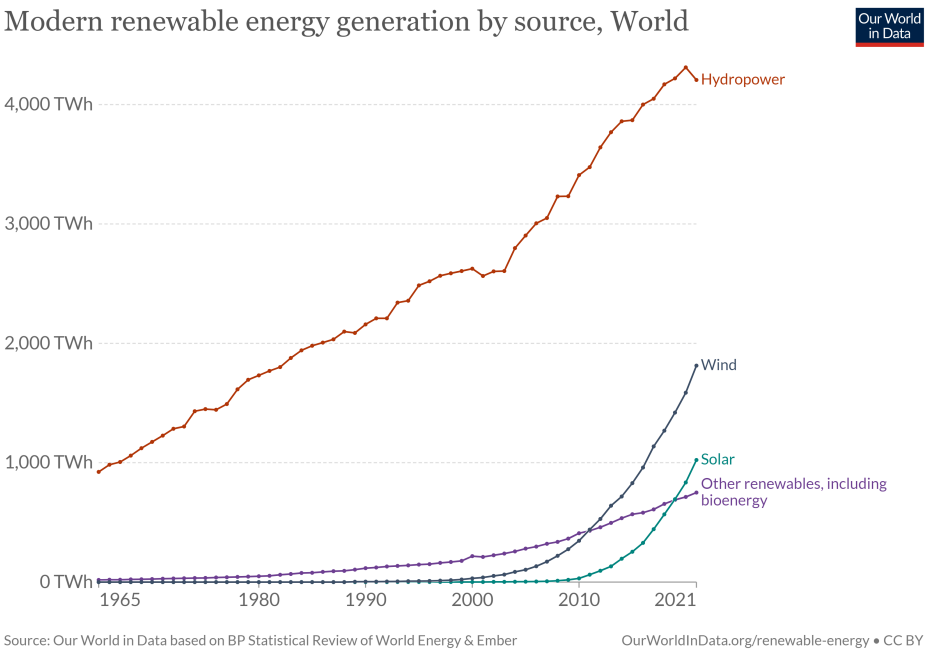

Figure 1.2: The energy generated from different renewable sources throughout the world [1]

1.2. Thin-film solar cells

The thin-film solar cell(TFSC) is a solar cell with thin layers approximately ranging from 1nm to 500nm on a substrate. The TFSC is lightweight and flexible solar cells. The cost of fabricating a thin-film solar module is less than a crystalline silicon module according to Roger G. Little et.al 1997.

Nonetheless, the module cost per watt increases by 6% due to TFCS's low efficiency. The efficiency was assumed to be 8% for the TFSC[18]. Therefore thin film silicon has the potential to reduce the cost further with increase in efficiency. In 2020, the global TFSC market was worth $11.3 billion and is expected to still increase to $25.3 billion by 2030, with a compound annual growth rate of 8.4% between 2020 and 2030 [19]. This shows the great potential of thin-films solar cells technology that was there 10 years back that can be developed on a large scale and still have great potential for improving production.

The most widely used absorber materials used to make thin film-solar are amorphous silicon(a-Si), cadmium telluride(CdTe) and copper indium gallium diselenide (CIGS) [20]. TFSCs were explored by industries and companies from 2005 to 2008 due shortage of pure poly silicon material which was needed to make the crystalline solar cell. However, it was difficult to reach highly efficient thin-film modules produced on a large scale even with cheap production costs. A lab-scale CIGS solar cell achieved comparable conversion efficiency with crystalline silicon solar cells of 22.8% in 2017 [21]. However, this could not be reproduced in large-area solar modules due to the dynamic deposition process used in mass production. This creates a difference in growth kinetics between large-area solar modules and the lab-scale solar cells which uses a static deposition process[21]. Additionally, elements like gallium and indium have limited availability [22]. In the case of CdTe, it was considered an environmental hazard and also has safety issues. The recycling of CdTe modules and the emission of cadmium into the atmosphere in the event of a fire were the major issues[23]. Due to these reasons, large-scale production of CIGS and CdTe modules was a great hurdle for the industry. On the other hand, the material available for the Amorphous silicon solar cell is abundant. Nonetheless, the material structure of amorphous silicon results in meta-stable behaviour under influence of light that is known as the Staebler-Wronski effect. It is a light-induced degradation that reduces the performance of the solar cell upon exposure to light to an unknown extent before attaining a stable efficiency [24].

A Company like HyET solar is a great example of the progress of thin-film silicon solar cell. In 2022 according to hyET solar, a thin film solar module manufacturing company, the lowest levelized cost of energy of thin-film solar module on foil is approximately 0.036$/kWh, which is less than crystalline solar panel which has 0.063$/kWh for residential applications. This comparison is between an 18% efficiecnt crystalline silicon solar module and 12% efficient thin-film silicon solar module on foil. This price difference is attributed to the lower installation cost and the high efficiencies of the the thin-film silicon solar module. For those PV applications where low cost is more important than high efficiency, amorphous silicon modules appear to be the best long-term option. When a sufficient surface area can be made accessible without incurring significant additional costs, they are particularly well suited for solar pumps and building integration. Amorphous silicon now holds a strong position in the market for power supplies for small instruments and is unlikely to be replaced [23]. Thin-film silicon technology will thrive through the coming years.

1.2.1. Amorphous and nanocrystalline silicon

The amorphous and nanocrystalline silicon are together used to make multi-junction solar cells. In Figure 1.3 shows an a-Si/nc-Si tandem solar cell which is also called a micromorph. The light comes through the substrate which is the glass in this case. In the case of TFSSC the glass substrate will be textured to increase the path length of light by scattering. Ideally, the light should pass through the glass, transparent conductive oxide(TCO) and the doped layers to reach the a-Si and nc-Si absorber layers. The intrinsic silicon layer in the middle of the doped layers absorbs the photon to generate electron and hole pairs. The holes travel through the p doped layer which has holes as the majority carries. The electrons travel through n doped layer which has electrons as the majority carriers.

The holes and electrons are separated in the absorber layer by an electric field generated due to the doped layers.

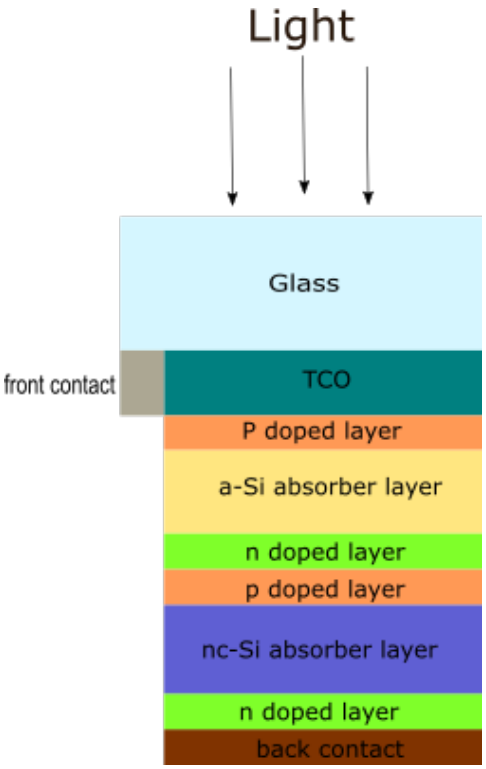

Figure 1.3: Architecture of micromorph solar cell

In the region between the absorber layer, there are two doped layers in contact. This is the recombination junction, where the electrons generated from a-Si and holes generated from nc-Si layer recombine. The electrons from the bottom cell will travel to the external circuit and finally recombine with the hole in the front contact. This is how the circuit is completed. This is a brief explanation of how the multi-junction TFSSC works.

1.3. Collaboration with HyET solar

HyET solar produces industrial-scale thin-film flexible silicon solar modules on aluminium foil substrates [25]. In the year 2022, Technische Universiteit Delft(TUD) and the company HyET(High yield Energy Technologies) signed a new four-year research contract for an academic-industrial partnership to achieve high conversion efficiencies in thin-film solar modules on aluminium foil. The TUD team helps them to accelerate towards their goal of producing high efficient solar modules by fabricating and experimenting on solar cells on lab-scale. The TUD team have demonstrated high efficiencies on glass, so pursuing routes towards efficiency improvements on glass makes sense. Tu delft mainly focuses on PIN configuration solar cells as the solar modules made by HyET on aluminium foil is also on the same configuration. The behavioural trends and design rules of the solar cell layers can be obtained from the lab-scale results. These results can help HyET to create their experimental design to optimize the solar module in large-scale by following the design rules and learning from and trends that were acquired.

1.4. Research gaps

It was projected by Guha and yang in 2013, that theoretically the initial efficiency for an a-Si/nc-Si/nc-Si triple-junction can go up to 23% [26]. This was said to increase even further after acquiring

a better quality of the nc-Si material bulk material. However, practically we have only a maximum initial efficiency of 14.8% for micromorph and maximum stable efficiency for a triple junction is 13.4% [27, 28]. A huge gap can be recognised between the efficiency we could reach and what we have reached.

The theoretical limit for Jsc is 36 mA/cm2 which can be obtained by scattering through textures. However, the highest Jsc obtained is only 30.5 mA/cm2 [26]. Hence, one of the main issues that should be handled is providing more light to the absorber layer of the solar cell to obtain high Jsc. The texturing of the substrate is important to increase the path length of light in the solar cell. This will result in a high Jsc. A relation has been established between both optical gains and electrical losses as a function of substrate roughness for nc-Si films [29]. The performance of different textures on solar cell have been studied for both periodic and random textures [27, 30–33]. Nonetheless, the performances of the wide variety of textures formed with various methods were not compared with each other on a-Si/nc-Si double and a-Si/nc-Si/nc-Si triple-junction solar cells. This needs to be done to find out the optimum texture for the TFSSC.

The initial p doped layer through which the light enters is called the p window layer. This layer is seen as a highly influential layer to the solar cell. This is because it has an high influence on the incoming light to the solar cell and the electrical properties of the solar cell [34–37]. The p layer influences current and voltage to a large extent in the solar cell. The division of the p layer according to the functionality is done by many researchers. After having a better understanding of the behaviour and working of the p doped layers from work done by de Vrijer et al[38–40]. By including the learning of earlier studies, optimization of the material, thickness, and architecture of the p layer can be done by finding out it's the dependence on the optical and electronic properties of a thin-film silicon photovoltaic device. This can an important step in reaching the greater goal of improving efficiency.

After maximizing the light absorption for the solar cell, the current has to be divided between the multiple junctions of the solar cell. This is done to reach a high Jsc as an output current. Using the n-doped silicon oxide layer as a reflector to reflect the light to the other junctions. Previously, This was explored on nc-Si single junction and double junction solar cells where reflector layer was studied [41, 42]. In a particular study, the thickness dependence of the silicon oxide reflective layer and the conductive and refractive properties of the n-doped silicon oxide was studied in a micromorph device architecture [43]. However, the variation of performance of the a-Si/nc-Si micromorph with varying oxygen concentrations at different thicknesses was not extensively studied to implement in the triple junction solar cell.

1.5. Research questions

Lab-scale samples of single and multi-junction solar cells with amorphous and nanocrystalline silicon solar cells are fabricated and characterised for this thesis. The main research question for the thesis that is derived from the research gaps mentioned in the previous section is *How and to what extent can the material, architecture and texture be optimized to achieve high initial efficiency for a multi-junction thin-film solar cell?*
The research question can be broken down into four sub questions

- How to obtain a standardised and error-free EQE measurements to acquire reliable Jsc values?
- Which type of texture is best suited for the thin film micromorph and triple junction solar cells to obtain high electrical properties and maximize the absorption in the absorber layers?

- How and to what extent can the architecture, material composition and thickness of the p-doped window layer be tuned in order to obtain desired optoelectronic properties in solar cell?
- Can a shift in generated photo current between junctions in a multi junction device be realized through variations in the thickness and oxide fraction of the silicon oxide layer between junctions?

This thesis aims to answer the research questions and formulate design rules for making more efficient thin film silicon solar cells from the results gathered from the experiments that were conducted.

1.6. Report Outline

The chapter 2 covers the fundamental concepts needed to understand the working of thin-film silicon photovoltaic devices. In chapter 3, an elaborate introduction to the equipment and techniques used to deposit and measure the solar cell is given. In chapter 4, the standard procedure to fabricate solar cells and substrates are explained in detail. In chapter 5, the results obtained from the experiments conducted are shown and discussed. Finally, the conclusions and recommendations that are derived from the results from the previous chapter are discussed in chapter 6.

2

Fundamentals

In order to understand the research work in this thesis some of the fundamental principles of physics needs to be explained. The working of semiconductor devices and thin film silicon solar cells are discussed in this chapter

2.1. Solar cell

Light behaves as both wave and particle. Albert Einstein in 1905 assumed that light consists of quanta called the photons.

$$E = h\nu \tag{2.1}$$

This phenomenon is used to explain the photovoltaic effect, which is the creation of a potential difference in a junction between two different materials by absorbing the photons. The solar cell works on this effect. The photovoltaic effect can be split into three parts: generation of charge carriers, separation of charge carriers and then the collection of the charge carriers.

2.1.1. Energy band formation in semiconductors

The energy band gap shown in the figure is created in any material due to the creation of separate quantum energy states for electrons because of close inter atomic interaction between two atoms(atomic bonds). In this case it is between two silicon atoms. The splitting of energy levels into discreet states happens because according to Pauli's exclusion principle no two identical particles can occupy the same quantum state [2]. The Figure 2.1 shows the splitting of energy levels of 3S and 3P orbital, which are the valence orbitals of silicon atom, into allowed states and forbidden states. It splits as 4 quantum states for upper band and 4 for lower band.

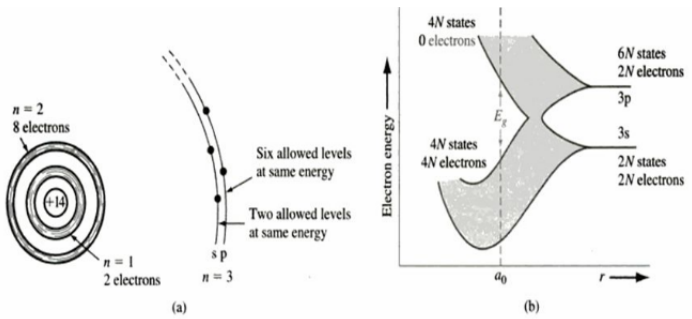

Figure 2.1: (a) Electron orbitals of silicon atom (b) Band gap states formation in silicon [2]

2.1.2. Generation of charge carriers

In Figure 2.2, a material that has an energy band gap of E_g absorbing the energy of the photon is shown. In Figure 2.2 (a), the material absorbs the photon and excites the electron from energy level E_i to energy level E_f. The energy difference between E_i and E_f equals the energy of photons. After absorbing the photon, electrons move from the valence band to the conduction band. This movement of electrons to the higher energy level creates a hole in the conduction band, this has a positive charge. This phenomenon of excitation of electrons only happens if the photon energy is more than the band gap of the semiconductor. Figure 2.2 (b) shows that the energy is lost by thermalization if the energy absorbed is greater than band gap energy.

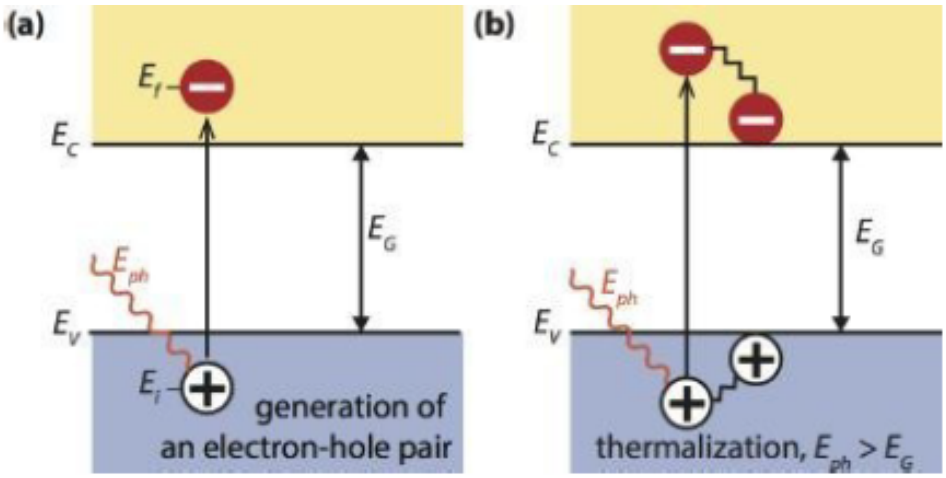

Figure 2.2: Generation of electron and hole pair in a solar cell [3]

2.1.3. Separation of charge carriers

The generated holes and electrons tend to recombine. However, to create a potential difference the electrons and holes need to be separated. The chances of recombination are smaller with shorter band gaps. The stable state of electrons is in the conduction band or the valence band. The electrons cannot exist in the energy levels of the band gap of the material as it is the forbidden state.

2.1.4. Collection of charge carriers

Collection of the charge carrier is the final step of converting chemical energy to electric energy. After the charge carriers are separated, they should be collected by the contacts to generate current in the external circuit. The complete circuit is shown in Figure 2.3. To complete the circuit the electrons recombine with the holes which are present in the material after completing the circuit.

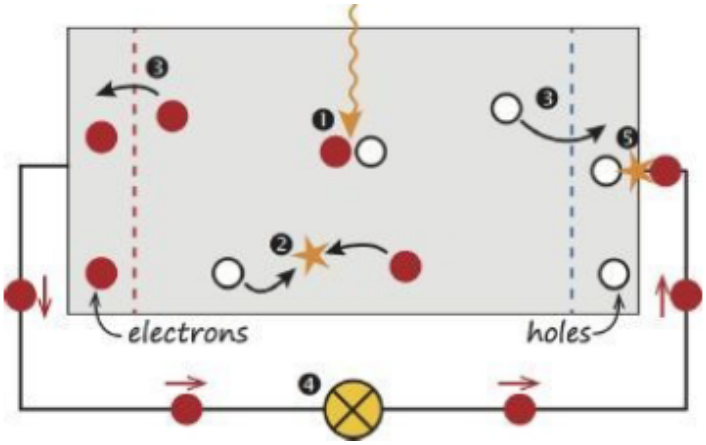

Figure 2.3: Collection of photo generated charge carriers from the solar cell[3]

2.2. Optics of flat interfaces

When light is incident on an interface it gets reflected, absorbed and transmitted. As mentioned in the section 2.1, for the solar cell to work it has to absorb the photons to generate the charge carriers. The light that gets transmitted or reflected is a loss of energy.

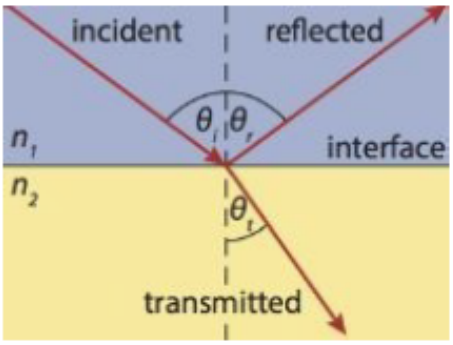

Figure 2.4: The incident, reflected and transmitted light between two optical interface [3]

The Fresnel's equation gives the relations between the magnitude of the incident, reflected and transmitted light. The Equation 2.2 and Equation 2.3 gives the Fresnel's coefficients for reflectivity. With the help of these coefficients [3], the reflectivity of unpolarized light can be calculated. Using Equation 2.4 reflectivity can be calculated. n_1 and n_2 are the refractive indexes of the 2 mediums above and below the interface as shown in the Figure 2.4. θ_i is the angle of incoming light on the plane and θ_t is the angle of transmitted light through the interface. In this, the mediums are assumed to be non-absorbing.

$$r_s = \left(\frac{\xi_{0r}}{\xi_{0i}}\right)_s = \frac{n_1 \cos\theta_i - n_2 \cos\theta_t}{n_1 \cos\theta_i + n_2 \cos\theta_t} \tag{2.2}$$

$$r_p = \left(\frac{\xi_{0r}}{\zeta_{0i}}\right)_p = \frac{n_1 \cos\theta_t - n_2 \cos\theta_i}{n_1 \cos\theta_t + n_2 \cos\theta_i} \tag{2.3}$$

$$R = \frac{1}{2}\left(r_s^2 + r_p^2\right) \tag{2.4}$$

$$\sin\theta_{\text{crit}} = \frac{n_1}{n_2} \tag{2.5}$$

In the Figure 2.4 when n_2 is lower than n_1(first layer is more denser than the second layer) , there is incident angle of light above which the light do not pass interface. This angle is called critical angle (θ_{crit}) and it is given by Equation 2.5. All of the incident light which is equal to or above the critical angle will be reflected back to the same layer, this phenomenon is called total internal reflection. In a solar cell we assume that no light is transmitted. Thus, just the equations of reflectivity are covered in this section.

2.3. Current and voltage characteristics of a solar cell

The most used external solar cell parameters are the J_{sc}, V_{oc} and FF. These are also used to calculate conversion efficiency. The short circuit current density(J_{sc}) is the current per unit area when the voltage is zero. This short circuit current density is affected by the photons absorbed by the absorber layers and the optical properties of the material of the solar cell.
The open circuit voltage(V_{oc}) is measured when the current across the circuit is zero. V_{oc} depends on the recombination and other factors of the solar cell.
Fill factor(FF) is the ratio between the maximum power generated by the solar cell divided by the product of the open circuit voltage and the short circuit current of the cell. In Figure 2.5, the solar cell parameters are shown.
The efficiency of a solar cell is determined by Equation 2.6. P_{in} is the power input from the sunlight.

$$\eta = \frac{V_{oc} I_{sc} FF}{P_{in}} \tag{2.6}$$

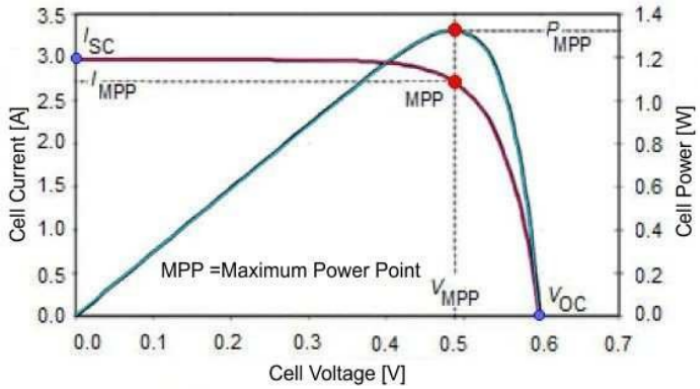

Figure 2.5: IV characteristic curves (red) and Power voltage curve (blue). Isc denotes the short circuit current and Voc denotes the open circuit voltage [4]

An illuminated solar cell has an ideal diode behaviour. This can be shown by an equivalent circuit diagram consisting of a diode and resistors connected in series and parallel to the diode. The series and parallel resistances are important factors that determines the JV curve and in turn, will also determine the fill factor of a solar cell.

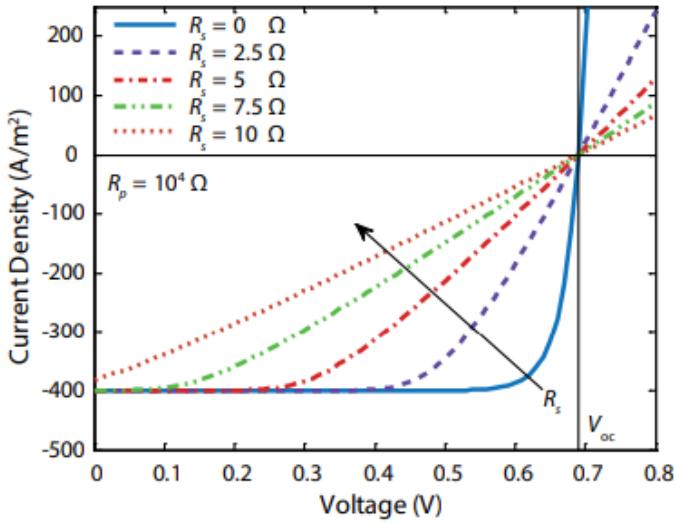

Figure 2.6: Change in current density and voltage with respect to change in series resistance of a solar cell[3]

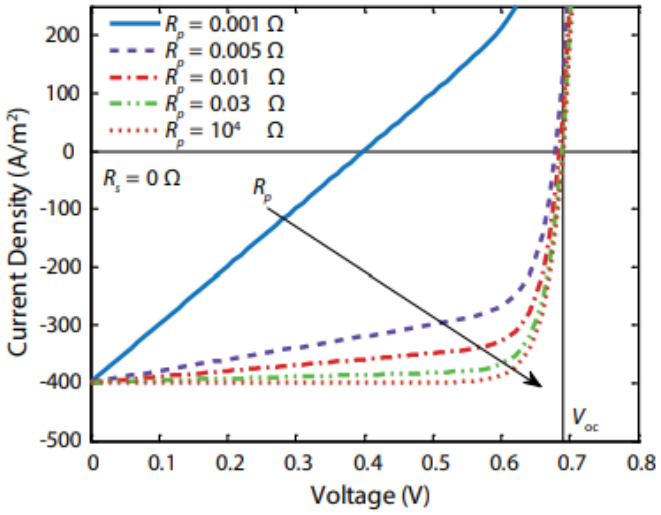

Figure 2.7: Change in current density and voltage with respect to change in shunt resistance of a solar cell[3]

In an ideal diode the shunt resistance should be very high($10^4\Omega$) and the series resistance should be as low as possible. If the shunt resistance is low, there will be a parallel circuit formed for electrons and holes to transport. This will lead to losses as the photo-generated carriers wouldn't be collected. If a solar cell is shunted, the solar cell will have a short circuit and an ohmic contact will be created. The decrease in shunt resistance will be reflected in the JV curve as an increase in the slope of the curve and will also substantially affect the maximum power point and FF. Furthermore, The series resistance should be low as the reason is direct. The resistance in the path electron and holes takes to travel should be low. From Figure 2.6 we can observe that the larger the series resistance lesser the steepness of the slope near the open circuit voltage point. From Figure 2.7 we can observe that the slope tends become positive from the short circuit current density. Hence, the increase in the series resistance and decrease in the shunt resistance will lead to a low fill factor.
The lateral conductivity is the electrical conductivity in the horizontal direction and transverse conductivity is the electrical conductivity in the vertical direction. For the n and p layers the transverse conductivity should be high so that the photo generated carriers travel in the vertical direction to

towards the front and back contact. The TCO should have high lateral conductivity so that the carriers spreads across the material and gets collected at front contact which is usually in the corner of the cell to prevent shading of the solar cell.

2.4. Losses in solar cells

The main losses in a solar cell are explained below [3].

- When the photons have lower energy than the band gap of the absorptive semiconductor material, then the energy of the photons is not sufficient to excite the electrons from the valence band to the conduction band.
- When the photons of energy are higher than the band gap, the energy of photons will generate electron and hole pair. However, there will be leftover excess energy released as thermal energy into the crystal lattice of the semiconductor material.
- Recombination of generated charge carriers in the bulk material or in the interface of layers can reduce the FF and V_{oc}. The recombination is determined by the electrical properties.
- Optical reflection of the interfaces between the layers that is explained in the previous section also leads to loss of energy.

2.5. Transparent conductive oxide

Transparent conductive oxide is the front contact layer for the solar cells. This means that only through this layer the light enters the solar cell for the photons to be absorbed and this layer also needs to be electrically conductive as it should conduct the electron or holes laterally for them to be collected in the metal contacts. Hence, the TCO should be both highly conductive and transparent.

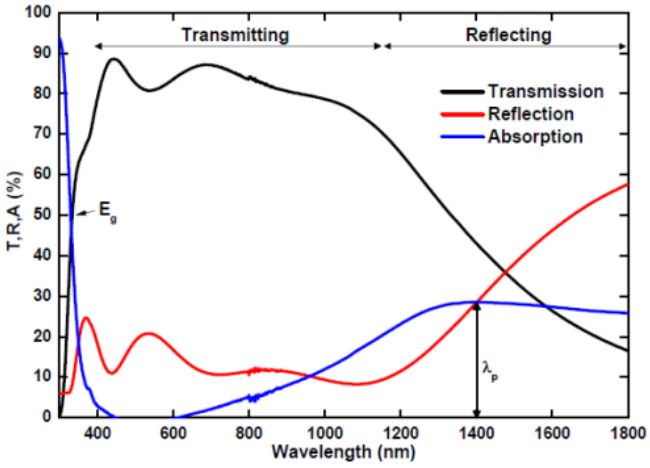

Figure 2.8: Absorption, transmittance and reflection of TCO with respect to wavelength [5]

In the short wavelength range, the absorption is high because the photon energy level is high at a shorter wavelength, therefore the energy of the photons can be greater than the band gap of the TCO. These photons will be absorbed by the TCO. This can be seen in Figure 2.8.
In the infrared region the absorption is dominant due to the Drude absorption, which also can be called as free carrier absorption. This can also be observed in the figure. The plasma frequency of the TCO is directly proportional to the density of the free carriers. When the frequency of light is lower than the plasma frequency the light is totally reflected by the material. This plasma frequency

should be low enough so that the TCO is transparent in the absorption region of the solar stack. To get a better picture an ideal TCO, it should be a transparent metal [44].

2.6. Hydrogenrated Amorphous silicon and nano crystalline silicon

The hydrogenated amorphous silicon is used to make solar cells on fleixible substrates [6]. Commonly used crystalline silicon has a tetrahedral configuration which is maintained throughout the crystal lattice. Unlike crystalline silicon, amorphous silicon has a disordered structure with varying bond angles and dangling bonds in the material [45]. There are various methods to deposit amorphous silicon. In 1975, amorphous silicon was deposited using a glow discharge technique also called plasma enhanced vapour deposition(PECVD) using silane gas. They also showed amorphous silicon can be doped with diborane and phosphine(PH3) to make n-type and p-type material [46]. It was then found out that the defective states of amorphous silicon can be passivated using hydrogen during the PECVD process which results in a less defective structure of amorphous silicon [47].

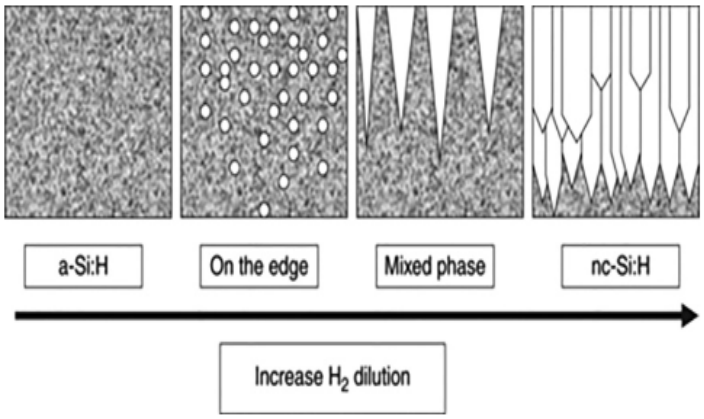

Figure 2.9: Phase transition from a-Si to nc-Si with hydrogen dilution [6]

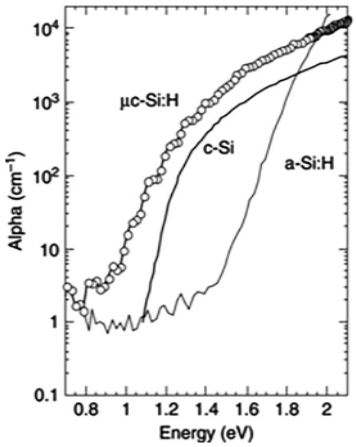

Figure 2.10: Absorption coefficient of nc-Si, c-Si and a-Si against energy[7]

In Figure 2.10 the absorption coefficients of different materials are plotted against the energy of photons. It can be seen that photons above 1.9 eV it has high absorption compared to crystalline silicon. This means it absorbs light in the lower wavelength region which is the blue part of the solar spectrum. High band gap amorphous silicon is generally used as the top cell in multi-junction solar

cells due to this reason. Even though it has high absorption, there was found to be a degradation in the photoconductivity of amorphous silicon when it was exposed to light. This reduces the efficiency of the a-si solar cells. The degradation is not indefinite, the efficiency of the solar cell will stabilize after a certain point in time. The effect is called the Staebler Wronski effect. This effect can be reversed by annealing the solar cell [48].
The solar cell configuration of thin film silicon solar cells is in the form of n-i-p or p-i-n. The n and p are the n-doped and p-doped silicon and I is the intrinsic amorphous silicon. It does not follow the usual p-n junction configuration used for crystalline silicon as for amorphous silicon as the diffusion length of charge carriers is low. Due to the large number of defects in amorphous silicon, schokley read hall recombination will dominate. The diffusion length of the charge carriers is only from 100 to 300nm. Hence, thin film silicon solar cells cannot rely on a diffusion mechanism for the transmission of charge carriers. Therefore, the N-I-P or P-I-N configuration is chosen. In such a configuration, an electric field transports the holes and electrons generated in the intrinsic amorphous silicon to the p and n doped material reducing the losses. The p and n junction is usually extremely thin which is about 90-100nm.
As shown in Figure 2.9, when the hydrogen dilution is increased, the amorphous silicon turns into nanocrystalline silicon. The nanocrystalline silicon which is made with higher dilution has high conductivity and low activation energy [49]. In a micromorph device, intrinsic nc-Si is thicker than the a-Si due to its low absorption coefficient in the red region compared to the absorption coefficient of a-si in the blue region. The usual thickness of nc-Si is about 1-4 microns to increase the path length of light which will increase the absorption. The nanocrystalline silicon consists of nanometer-sized grains. The grain growth increases with hydrogen dilution of amorphous silicon. It can be seen from Figure 2.10 that the nanocrystalline silicon has good absorption in the low-energy region. Thus, it absorbs red light more than blue as the band gap is low.

2.7. Multijunction thin film solar cell

Tandem micromorph can be a great candidate for thin film silicon solar cell which consists of amorphous silicon and nanocrystalline silicon [50]. As the amorphous silicon absorbs the light in the lower wavelength(blue light) and the nanocystalline silicon absorbs light in the higher wavelength(red and infrared region). In a multi-junction like a micromorph, it can be fabricated that the amorphous silicon is not the current limiting junction. If the amorphous silicon is the current limiting junction then the performance will eventually reduce due to Steabler Wronski effect(SWE) until stability is obtained. If a-Si is not the current limiting junction SWE will still decrease the efficiency, but the effect will be less severe since *FF* of the nc-Si plays a more dominant role than a-Si. The aim is to reduce effect of SWE.
The band gap of the nanocrystalline silicon is lower than the band gap of the amorphous silicon. Due to this light should be first passed through the Amorphous silicon solar cell and then through the nc-Si, so that the infrared light with low energy will be absorbed in the nc-Si cell(bottom cell) and blue light will be absorbed by a-Si(top cell) of the tandem or the triple junction solar cell. The blue wavelength photons have high energy and low penetration depth.
In a multi-junction solar cell, the layers are deposited in the transverse direction. They are connected in series. So the open circuit voltage of a multi-junction solar cell will be the sum of open circuit voltages of the individual junctions. The current density is limited by the junction generating the lowest current. The electrons generated by the top cell and the holes generated by the bottom cell should recombine to complete the circuit. The recombination happens in the tunnel recombination junction. At the recombination junction, an n-p junction is present. The n-p junction can create reverse voltage which can be detrimental to the cell performance. To prevent this tunneling of electrons from the n layer and holes from the p-layer takes place. The depletion region is narrow for both layers which creates a steep of the valence and conduction band so that the valence band of

the p layer is closely aligned with the conduction band of the n layer. This will allow the holes from p-layer to recombine with electrons from the n layer to recombine. The n and p layers are both very thin and should have low resistance for better recombination. This makes sure only the electron from the bottom cell is collected and holes from the top cell are collected.

3

Deposition and measurement of thin film silicon solar cell

3.1. Deposition of solar cell layers

3.1.1. AMIGO

The AMIGO machine was used to deposit the silicon layers on the substrate using plasma-enhanced vapour deposition. It has 6 chambers in it. Each chamber is used to deposit a particular type of layer. This is to prevent cross-contamination between different layers of the stack. In the first four chambers p-doped, n-doped, intrinsic a-Si:H and intrinsic μc-Si:H layer depositions can be made. Amigo uses the plasma-enhanced chemical vapour deposition process to deposit the amorphous and microcrystalline silicon layers. In the 6th chamber, aluminium doped zinc oxide can be sputtered and in the 5th chamber, silicon alloys like silicon carbides can be deposited. The AMIGO has 5 load locks in which the holders containing the substrate are placed. The load lock will be pumped down to lower pressure after the samples are placed in it. A robot arm present in the center of the chambers moves the sample from one chamber to another. For deposition of the thin film silicon, the precursor gas used is silane(siH4) and hydrogen to dilute it. With these gases, plasma is generated by using a very high frequency or radio frequency voltage between the electrodes. This disassociates the Sih4 into various radicals like SiH3, Sih2 or SiH. Then these radicals get deposited on the substrate and create a layer after reacting with it. Nanocrystalline silicon can be formed by increasing the flow of H2 gas at the right pressure, power and temperature. Di-borane and phosphine are used as a dopant to make p-type and n-type silicon layers respectively. To make silicon oxide layers carbon dioxide gas is used and fused with silane.

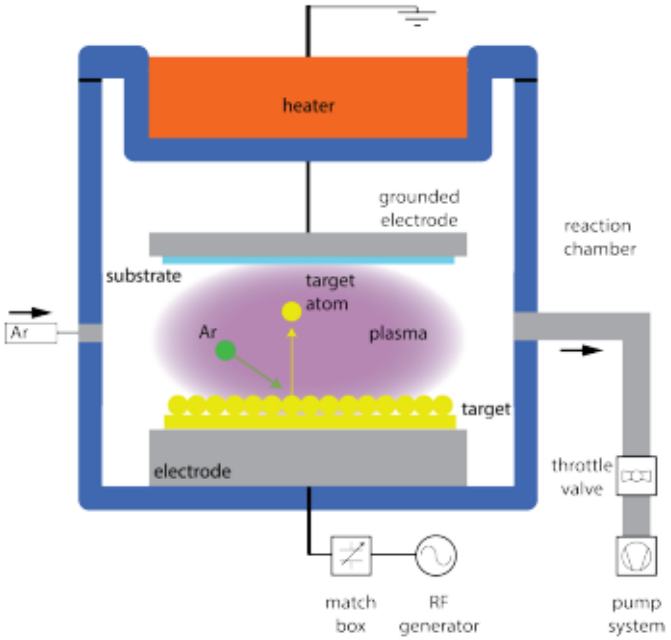

Figure 3.1: Schematic diagram of RF magnetron sputtering machine [8]

3.1.2. PROVAC

The PROVAC machine was used to deposit metallic front and back contact on the substrate using physical vapour deposition. The sample that needs to have the front contact deposited is clipped on the top to the holders. These holders are attached to a disc that rotate slowly while the deposition happens. Some of the samples are placed on a mask to make sure the silver or aluminium is deposited in a particular region. For the back contact, silver granules will be placed on a tungsten boat. Then the chamber is pumped down to low-pressure ($<2^{-5}$ mbar) to start the process. The current is then passed which heats up the boat and evaporates silver. This gets deposited on the cold samples placed above. Other materials like Aluminium and chromium, have separate crucibles. For these other materials, electron beam evaporation is used to evaporate the metal. Electrons of high energy are emitted for this process.

3.2. Measurement of solar cells

3.2.1. WACOM

The WACOM machine gives the IV curve for the solar cell. The power density of the light source is equal to the AM 1.5 spectrum, which is 1000W/m^2. The area of each cell measured is 16cm^2. The light source consists of both Xenon and Halogen bulbs. An accurate open circuit voltage and fill factor are obtained. To measure the IV curve of the solar cell two probes have to be placed on the front and back contact. Then the solar cell is illuminated by the solar simulator to measure the performance of the device. Different types of stages are used to measure the p-i-n and n-i-p device architectures. As for p-i-n the cell should be measured from the back of the cell and for n-i-p the probes need to be placed at the front part.

3.2.2. External quantum efficiency setup

The external quantum efficiency (EQE) is the ratio between the number of photo-generated carriers supplied to the external circuit by the solar cell and the number of photons incident to the solar cell [51]. The EQE is used to find the accurate short circuit current density of each junction by using the Equation 3.1 which integrates the EQE along the wavelength multiplied by the photon flux.

$$J_{sc} = -q \int_{\lambda_1}^{\lambda_2} \mathrm{EQE}(\lambda) \Phi_{ph,\lambda}^{AM1.5} d\lambda \tag{3.1}$$

Figure 3.2 shows an example of the experimental setup to measure the EQE of a sample. It can be seen that Xenon lamp is used as the probe light source. The probe light goes through the monochromator and gets periodically chopped by the chopper. The lock-in amplifiers is used to acquire a good signal to noise ratio. The reference diode is used to correct the variations in the spectral intensity of the lamp over the wavelength. Additionally, the setup in Tu delft has eight bias lights, which are not included in the figure. Bias lights with different intensities at various wavelengths bias the junctions of multi-junction solar cells.

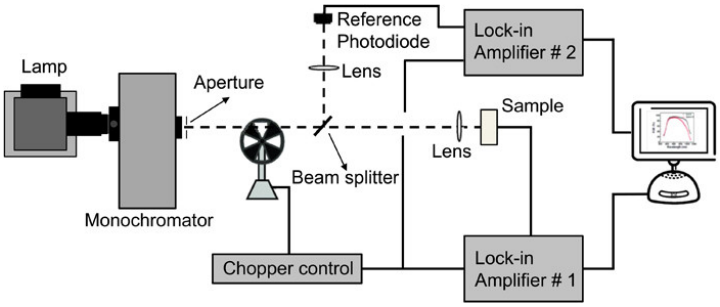

Figure 3.2: Schematic diagram of the EQE setup [9]

3.2.3. LAMBDA

The LAMBDA machine is used to measure the reflectance and transmittance of the solar cell samples. It has an white integrating sphere where the light undergoes reflections and is trapped inside until it reaches the detector. The reflectance is measured in the wavelength range of 300-1200 nm. For measuring reflectance, the sample will be placed behind the integrating sphere. The concept of this machine is that the light reflected will enter the integrating sphere and might undergo multiple reflections before the light gets detected by the detector. It is shown in Figure 3.3, the specimen which is the solar cell in our case is placed on one side of the integrating sphere and light gets reflected from the specimen and eventually gets to the detector diode. The reflectance is calculated by the amount of light received by the diode in reference to the calibration done with a closed integrating sphere. The cross-sectional area of light from the light source is reduced to fit and align into one cell of the sample using different types of slits for measuring the samples.

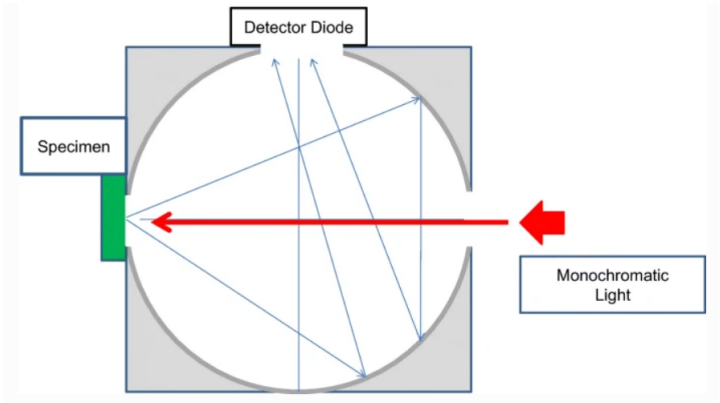

Figure 3.3: Integrating sphere inside the Lambda machine[10]

4

Methodology

Two device architectures were used in this work. The configuration was according to the deposition order of layers of the solar cell. the deposition order refers to p-i-n or n-i-p. Superstrate/substrate exclusively refers to the position of the substrate in reference to the incident light. In superstrate configuration the light passes through a transparent substrate first. First the front contact is deposited on the substrate then, the p-type, intrinsic and n-type follows in the case of thin film silicon. For substrate configuration, it is the opposite, where the deposition starts from the back contact. The deposition order of superstrate and substrate configuration are shown in Figure 4.1 and Figure 4.2
In these configurations single and multi junction devices were fabricated with amorphous silicon and nano-crystalline silicon.

Figure 4.1: superstrate configuration deposition order

Figure 4.2: substrate configuration deposition order

The samples are stored in the vacuum bulb in between the processing steps and measuring. This is to reduce the degradation of solar cell performance with the ambient exposure. this type of degradation was also not found to be fully reversible upon annealing [39].

4.1. Substrate configuration

For fabricating solar cells in substrate configuration(n-i-p), both glass and wafers were used as the substrate. An n-type polished silicon wafer with a thickness of 500 microns was used. The wafer was then textured with either honeycomb structure or smooth pyramids as explained in the previous chapter. For glass substrates, Corning Eagle XG glass was used as the glass substrate and it was cut to a dimension of $10 \times 2.5 cm^2$ to make the depositions.

4.1.1. Back contact deposition

A layer of SiO_2 with a thickness of 300nm was deposited on the textured wafer by oxidation in a furnace. The SiO_2 layer separates and insulates the deposited solar cell from the wafer. Further, On the

SiO_2, 500 nm silver and 90nm Aluminium doped zinc oxide(AZO) are deposited for high reflectivity of photons and lateral conductivity of electrons respectively. Silver and the AZO layer together make up the back contact. The deposition of Silver is done in the Provac by thermal evaporation and AZO deposition is done by sputtering in the AMIGO.

4.1.2. Photo active stack and front contacts

The next step is the deposition of the photoactive stack. In the case of a multi-junction substrate device, nc-Si layers are deposited followed by a-Si layer. In Figure 4.5 the layers of a n-i-p micromorph solar cell device is shown. For the photoactive stack, the thin n doped layer is deposited first then the intrinsic layer and finally the p doped layer.
As shown in the figure, ITO and 500 nm of Aluminum is deposited for the front contacts. The ITO is deposited by sputtering in the ZORRO machine and the Aluminium is deposited by PVD evaporated by an electron beam. Aluminium is chosen as the front contact due to its high electrical conductivity. Indium tin oxide(ITO) was used as the standard TCO for the front contact. Experiments on TCOs are carried out to find the optimum TCO for the solar cell based on its optical and electronic properties. ITO is used now due to its robustness and reproducibility. Eventually, the TCO used will be changed according to the TCO study conducted for the thin film silicon solar cell in TU delft.

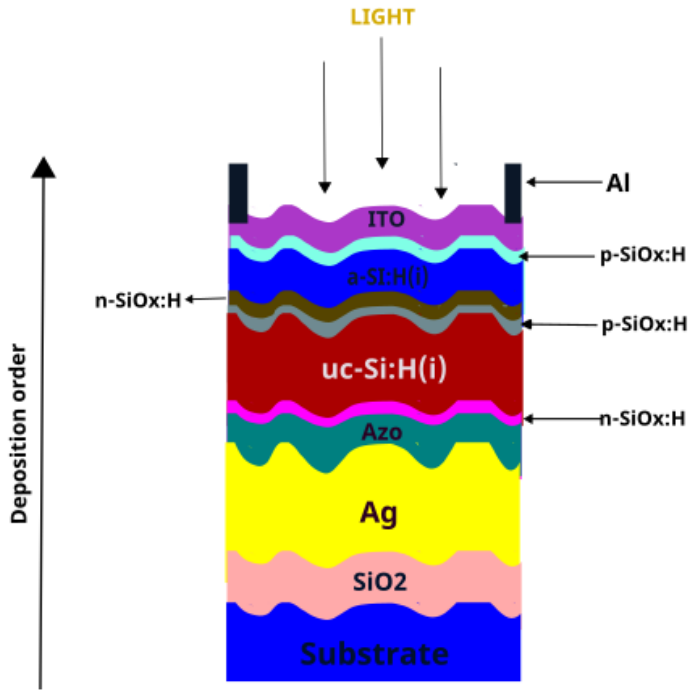

Figure 4.3: tandem n-i-p device

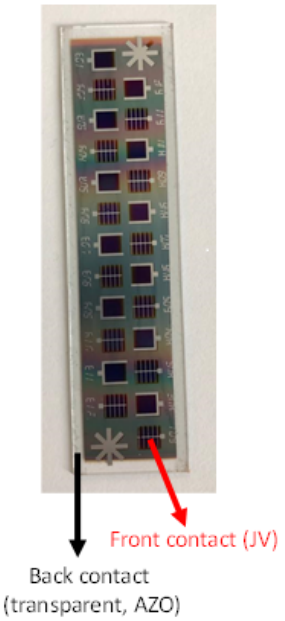

(a) Solar cell on textured glass

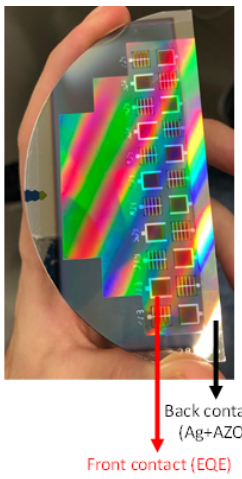

(b) solar cell on wafer with honeycomb texture

Figure 4.4: solar cells on wafer and glass in n-i-p configuration

The mask with which the Aluminium back contact is deposited has two types of design that occurs alternatively. The Figure 4.4 shows the two designs for both wafers and glass substrates. The one with the grid has a higher collection as the holes need not travel a long distance laterally to get collected on the front contact compared to the other design. This is used for optimal JV measurements. The other type of Aluminium back contact deposition is used to measure the EQE as there is no shading due to the grid structure. The front contact used for EQE and JV characteristics is also specified in the figure. It also shows for each sample of the substrate configuration 22 cells can be measured.

4.2. Superstrate configuration

For the supersaturate configuration, Asahi glass or other textured glass was used as the substrate. Asahi glass is a commercially available textured glass and already has fluorine tin oxide(FTO) as TCO deposited on it.
An 500 nm Aluminium strip is deposited as the front contact on top of the glass.
The photoactive stack is deposited on the aluminium strip in the order of p doped layer, then the intrinsic layer and then the n-doped layer. Finally, the 30 back contact squares with the dimensions 4x4mm are deposited with the help of a mask in PROVAC. The back contact consists of 800nm of Al, 30nm of Cr and 300nm of Ag. The chromium glues the silver and aluminium together. Silver for the reflectivity and Al for the conductivity. From each sample of superstrate configuration, 30 cells can be measured.

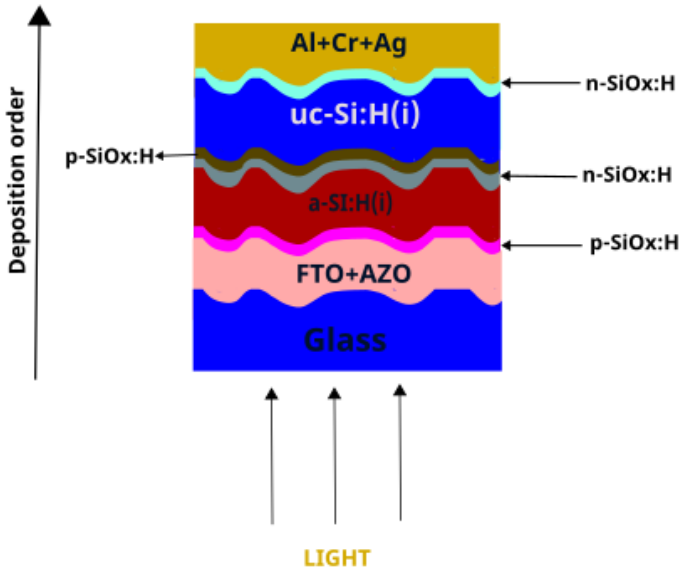

Figure 4.5: tandem p-i-n device on asahi

There are different experiments conducted to optimize different layers and textures of thin film silicon solar cells.

4.3. Texturing of substrates

Texturing is crucial to improve the efficiency of micromorph and triple junction thin film silicon cells. Texturing helps to increase the path length of the light in the absorber layers without increasing the absorber layer thickness which will lead to the absorption of more light [52] [**?**] [**?**]. This can directly increase the current density generated by the cell and in turn, increases the performance of the cell. As we can observe from the Figure 2.10 the absorption coefficient at infrared(low energy) is low even for nc-si. Different types of textures are used in this thesis namely honeycomb, smooth pyramidal, AZO and ITO textured. Hitoshi sai studied the performance of solar cells with varying the period of honeycomb texture [33]. The honeycomb textures are made on the $500\mu m$ thick silicon wafer smoothened on one side. First, 300nm SiO_2 is grown on the wafer, which is done by wet oxidation at $1100°C$ for 16min and 30sec in the furnace. Then, on the SiO_2 layer, a photoresist is deposited by lithography. After which a mask with four quadrants containing the honeycomb structure is exposed to the photoresist, which will be then developed. The development process consists of the removal of the photoresist part that is not covered by the mask by irradiation. A pattern is created in this way. The pattern is then replicated on the oxide layer and then the photoresist is completely removed using acetone at $40°C$. A poly etch is used to etch the wafer that is exposed by the pattern which creates craters on the wafer. The wafer will be dipped in the poly etch for 12mins to obtain craters. At last, the Silicon oxide is etched out at the end and the textured wafer is ready for further deposition.

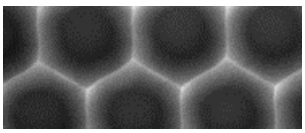

(a) SEM image of honeycomb texture

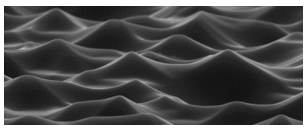

(b) SEM imgae of a smooth pyramid texture

Figure 4.6: A figure with two subfigures

Period in a honeycomb texture is the distance between two centers of the hexagon and height is the distance from one corner to the center of the hexagon, the ratio of height and period should be around 0.25 [53]. In a honeycomb texture, when the nc-Si absorber layer is more than a particular thickness threshold, crack starts to form on it. The cracks leads to collection losses. The thickness threshold depends on the period of the masks used to form the honeycomb texture. The threshold thickness increases with increase in period of the substrate. For a $0.5\mu m$ thick nc-Si absorber layer a period of $1\mu m$ was found to be ideal and for $3\mu m$ thick nc-Si a honeycomb period of $3\mu m$ to $4\mu m$ resulted in low collection losses [33].

The smoothened pyramid textures were also used to scatter light and increase light in-coupling. To make the Smooth textures on the wafers first random sharp pyramid texture is formed and then smoothened to obtain the texture. The smoothening is done because a sharp texture can result in cracks during the growth of nanocrystalline silicon on the wafer [33]. The polished silicon wafer is etched in tetramethylammonium hydroxide (TMAH) at 80C for 15 minutes to create the pyramidal texture. Then it is dipped in an acidic etch containing HF and HNO3 (69.5wt. in H2O) and water for a few minutes to smoothen the texture. The SEM image of this texture is shown in Figure 4.6b.

Different texturing roughness can also be obtained by etching indium tin oxide(ITO) and Aluminium doped zinc oxide(AZO) on glass. Textures can only be formed by anisotropic etching as isotropic etching will etch all the parts of the surface in the same way. The ITO and AZO were deposited on eagle corning glass at a temperature greater than ambient which promotes crystalline growth and will lead to anisotropic etching [27]. Asahi textured glass was also used, which is a commercially available glass for deposition of solar cells. The TEM image of Asahi is shown in Figure 4.8. It already has textures on it with a root mean square roughness of 42nm. Flourine tin oxide deposited on top of the Asahi glass. To fabricate textures by etching the TCO like ITO and AZO. The TCO on glass is Wet etched in an aqueous solution of hydrogen fluoride (HF, 49 weight percent) and hydrogen peroxide (H2O2), with a volume ratio of H2O:HF: H2O2 = 10:1:2, produced the crater-shaped micro-textures on glass. When the TCO layer etched away from the glass, the etching process was stopped, and the corning was carefully cleaned in deionized water.

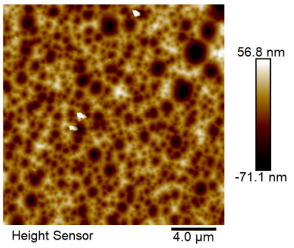

(a) AFM image of a AZO etched texture

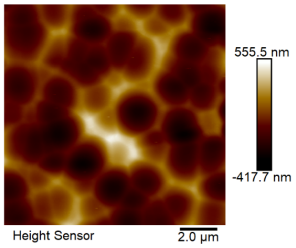

(b) AFM imgae of a ITO etched texture

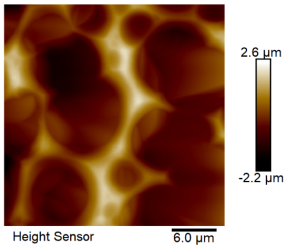

(c) AFM image of texture of Hairen tan's sample

Figure 4.7: The AFM images of ITO, AZO etched and Hairen tan's substrates

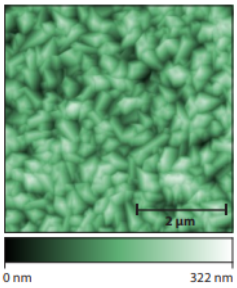

Figure 4.8: TEM image of a asahi textured glass

5

EQE study

In this section, correcting an artifact in the EQE measurement of micromorph solar cells will be discussed. The effect of variation of the bias light combinations, probe light intensity and voltage bias will be studied on a micromorph to minimize the error in the EQE measurement.

5.1. The artifact

The Figure 5.1 shows the artifact that existed in the EQE measurements of the both the junctions of the micromorph cell. An artifact is a defect or deviation from the actual measurement. Before proceeding with further experimentation, this artifact should be solved to obtain a reliable J_sc measurement. Only then we can compare the results of the experiments on solar cell, analyze it and arrive to a well grounded conclusion.

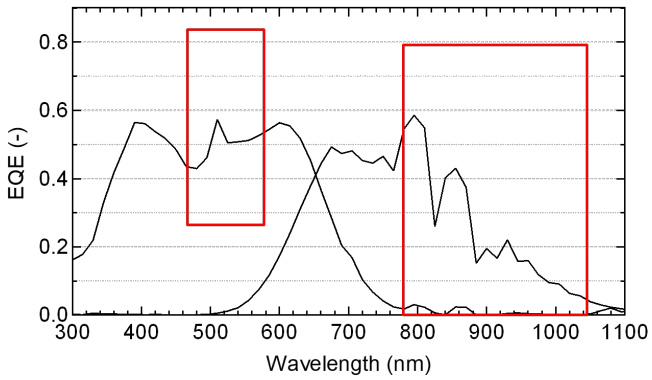

Figure 5.1: The artifacts in EQE measurement of the bottom and top cell of micromorph

In order to solve this artifact in measurement, we should know the working of the EQE setup and the how to measure the micromorph tandem cells. Then, we should find the possible causes for the artifact in measurement. Finally, attempt to solve the problem.

5.2. Measuring the EQE of a micromorph tandem device

The spectral photon flux of bias lights used in the EQE setup in the TUD lab are shown in Figure 5.2. The number on top of each of the peaks indicate the bias light switch numbers in the eqe setup. These numbers will be used in further discussions to indicate individual bias lights.

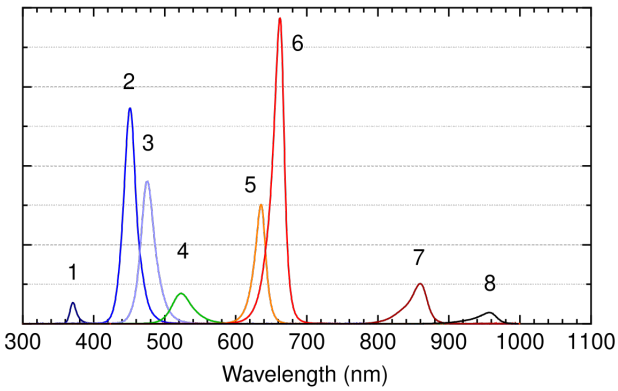

Figure 5.2: The photon flux of each of the bias lights in the EQE setup. 1-8 is the number on the bias light

The EQE of top and bottom cell cannot be measured individually in a tandem solar cell, as both the terminals of the solar cell can only be contacted together. In this thesis, the junction which is not measured is call the non-targeted cell and the junction for which the EQE needs to be measured is the targeted cell. In order to measure the EQE of a particular junction of a tandem or triple junction solar cell, the non-targeted junction should be biased with light to saturate the junction with charge carriers. The junction that generates low amount of carriers will be the current limiting junction. The output current from the solar cell is determined by the current limiting junction. Thus, the targeted junction should be limit the current of the solar cell.
The bias lights on non-targeted junction saturates the junction and starts to generate carriers constantly to make the targeted junction current limiting. To find what bias lights should be turned on to measure the tandem device, first, the solar cell should be measured with no bias. The no bias light measurement can be seen in Figure 5.4 as the black dotted line. The black dotted curve is the common area (500nm to 800nm) at which both the top and bottom cell generates carriers. This measurement shows at what wavelength the top cell stops absorbing and bottom cell starts absorbing photons. From the figure we can be sure that it is safe to light bias the bottom cell from 800nm to measure the top cell, as after that point only the bottom junction generates charge carriers. This can saturate the bottom cell. Hence, the bias lights 7 and 8 are turned on to measure the top cell. If bias lights with a wavelength less than 800nm is turned on, then we could risk top cell not being the limiting junction anymore as the top cell will also start generating carriers due to the bias light. Furthermore, this may lead to wrong measurement even though the top cell turns out to be the limiting junction, as top cell will already be generating carriers in addition to the carriers generated due to the probe light. An similar method is used to bias the top cell during bottom cell measurement. usually the bias lights 1 and 2 are used which are less than 500nm are used to bias the a-Si top cell. However, the artifacts in Figure 5.1 are from turning on the bias lights 7-8 to measure the top cell and 1-2 for measuring the bottom cell. In this thesis, the term real EQE means that the targeted cell should be the current limiting cell and should be measured at short circuit condition throughout the EQE measurement.

5.3. The problem

The intensity of the probe light is not constant with variation in wavelength. It varies due to fluctuations in the intensity of the emission spectrum of the xenon lamp used for the probe light. The probe light intensity from the xenon lamp can be seen in the Figure 5.3. The peaks in probe light intensity along the spectrum can be seen in the same figure, in the wavelength range 450nm to 550nm and 800nm to 1000nm.

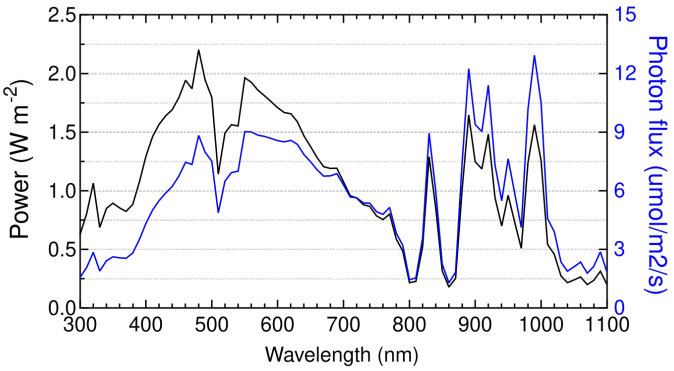

Figure 5.3: The photon flux and power of the probe light of the in house EQE setup

When we take the targeted cell as the top cell, the bottom cell is the non-targeted cell that should be light biased. The EQE of the top cell is measured from wavelength 300nm to 800nm.
The ratio between the probe light intensity and the bias light intensity is an important factor to take into account to realize the problem. The probe light xenon emission spectral peaks in intensity in the low wavelength range (450nm-550nm). This creates the possibility of the probe light intensity to exceed the bias light intensity and make the non-targeted cell as the current limiting cell, as there can be more photo-generated carriers in the targeted cell. For measuring the top cell, bias lights 7 and 8 were switched on. The intensities of these bias lights are low compared to the bias light intensities in the lower wavelengths, particularly 2 and 3. This can be seen in Figure 5.2. This can be one of the reason for the artifact. An similar reason can said for measuring the bottom cell. The probe light intensity might be more than the bias light intensity.
The main cause of the problem could be that the non-targeted bottom cell of the solar cell does not have high response in the red and infrared region. The low response of the non-targeted cell can also lead to an low generation of charge carriers compared to the targeted cell. This will eventually lead to the non-targeted cell being the limiting cell even though the bias light has more intensity than the probe light. This explanation also is in sync with the fact that only few micromorph cells had the artifact in the EQE measurement. Hence, it can also be attributed to the losses in the solar cell.
Further, for a solar cell with low shunt resistance, the real EQE cannot be obtained with only changing the bias light and probe light intensities. It can be only dealt with an additional voltage bias. The purpose of the voltage bias while measuring a EQE will be explained in the upcoming section.

5.4. Solutions

To solve this problem either the bias light intensity has to be increased or the probe light intensity should be decreased using light filters. In subsection 5.4.1 we will investigate the effect of increasing bias light intensity while in subsection 5.4.2 we will investigate the effect of decreasing probe light intensity. Before reducing the intensity of the probe light we need to check whether we can solve the problem by increasing the intensity of the bias light by using more LEDs.

5.4.1. Bias light experiment

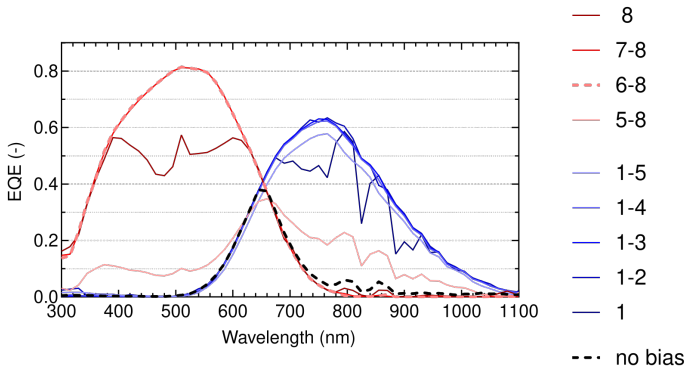

Figure 5.4: Measuring the EQE of the top and bottom junctions of a micromorph solar cell in various bias light combinations

In Figure 5.4 different bias light combinations are used to obtain the real EQE of a micromorph solar cell. The measurements were done in zero voltage bias so that we only study the effect of bias light. The study was done on a p-i-n tandem device on Asahi glass substrate. The intensity of the bias light was kept at the maximum for all readings.
We observe that only when 6-8 and 7-8 bias lights are turned on we get a smooth EQE curve for the top cell. For Properly biasing the bottom cell, 1-2 or 1-3 bias lights should be turned on as shown in the figure. Even though the number 6 bias light peaks at a wavelength of 650nm, it biases the top cell for this sample. The 6 bias light biases both junctions because it is in the intersection where both the top cell and bottom cell generates current. Since the EQE value is quite low from 650nm to 800nm wavelength range, the top cell can still be the limiting junction, as the bottom cell is now biased over the whole wavelength range of its EQE. However, it is a safe option to just use 7-8 bias light to bias the bottom junction. when an artifact appears in the EQE measurement in the 400nm to 600nm wavelength range, then the bias light 6 can be added to solve the artifact. The EQE that was obtained was limited by the targeted cell throughout the wavelength that was measured for the targeted cell. However, this EQE is most probably not measured in short circuit conditions might be because the cell is operating in reverse bias condition. Hence, the real EQE is not obtained. Nonetheless, proper light biasing conditions will take us closer to the real EQE.

5.4.2. Probe light intensity reduction

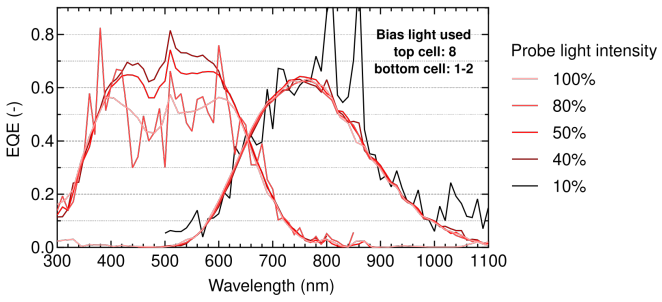

Figure 5.5: EQE with varying the probe light intensity with bias light 8 for top cell and 1-2 bias light for bottom

In Figure 5.5, a study using different probe intensities is shown. This study is done on the same sample on which the bias light study was done. In this study, to test the usefulness of changing the probe light intensity, an artifact was artificially created by improperly biasing the top cell. Only the bias light 8 was turned on to bias the bottom junction as shown in the Figure 5.4. We can observe that with decrease in the probe light intensity the top cell EQE curve is improving. The 40% reduction in the intensity has the best EQE measurement compared to the 100% probe light intensity curve. This means decreasing the probe light intensity can also be an effective way to improve the quality of the EQE measurement. It can be also observed from the figure that the noise of the EQE increases with decrease in probe light intensity. The noise is the highest with 10% probe light intensity. Hence, the reduction in probe light intensity should find a optimum trade off between signal and noise. The difference in the curve is not so much evident in the bottom cell curve as it is under proper bias light conditions thus there isn't an improvement in the curve, only the noise can be seen slowly increasing with decreasing the probe light intensity. Decreased probe light intensity together with the correct bias light settings can help us get a good measurement by making the targeted cell current limiting throughout the measured wavelengths.

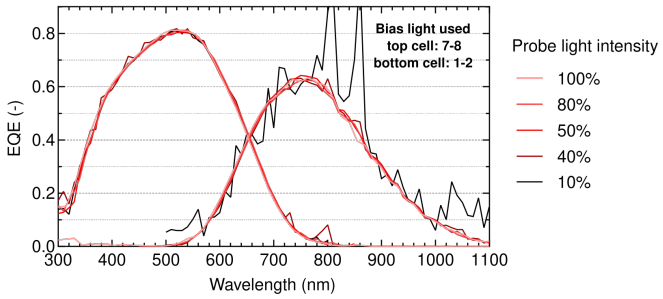

Figure 5.6: EQE measurements with variation in probe light intensity from 10% to 100% with 7-8 bias lights switched on for top cell and 1-2 bias lights switched on for bottom cell

In Figure 5.6 similar experiment was conducted as the previously discussed study. The only difference is that the 7 and 8 bias light are turned on, which properly biases the top cell. The noise on the top cell can more distinctly seen in the top cell. The EQE curve with 40% reduction in the probe light intensity has some noise on the curve and a smooth curve is obtained with 50% reduction in probe light intensity. From these experiments, an 50% reduction in probe light was made a standard for measuring the cells, as a middle ground is reached between the noise in the curve and getting the actual EQE values.

5.4.3. Voltage biasing

In Figure 5.8, it can be seen that with a negative voltage bias the EQE of the top cell increase from -1V to -3V. Whereas, for positive bias there can be seen a decrease in the EQE when a voltage of 0.5V and 1V are applied. When the a voltage greater than 1 is applied, the shape of the EQE resembles the Xenon diode spectral curve.

To explain voltage bias, a micromorph is taken as an example. The total voltage of the tandem cell is zero. The bottom cell of the micromorph is the target cell. The non-targeted cell is properly biased with light. With no voltage bias, only the non-targeted cell will be light biased when the EQE measurement is taken. Assume the wavelength of the probe light moves up with some interval from 300nm(blue) to 1100nm(infrared). When the probe light is blue, the light will only be absorbed by the top cell which is the non-targeted cell and no current will be generated in the targeted cell cell (bottom cell). As the bottom cell is limiting junction with no current generation, the operating point of the cell will be in open circuit condition. This shown in Figure 5.7 (a) and (b). when the

probe light is red, the bottom cell starts absorbing and the total current generated by the cell will be higher. Now the top cell will be operating at point above and near V_{oc} as the bottom cell will also start generating charge carriers but will be still the limiting junction. Therefore, while measuring the bottom cell, the top cell will be at forward bias voltage less than the V_{oc} of the cell. As already mentioned, the voltage of the whole tandem cell is zero. Thus, the target cell will operate in reverse bias equal to the absolute value of the operating voltage of the top cell. To truly obtain the EQE of the targeted cell at short circuit conditions(V=0), a small bias forward voltage which is less than the V_{oc} of the non targeted cell must be applied.

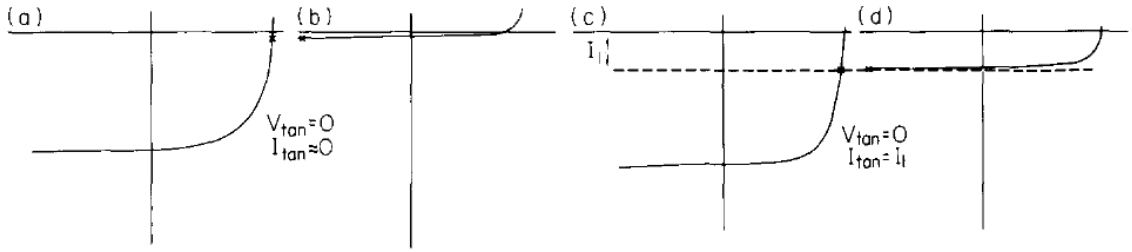

Figure 5.7: V_{tan} and I_{tan} are the voltage and current of tandem cell. Y-axis is current density(mA/cm^2) and x-axis is the voltage(V). The IV characteristics of micromorph cell Under blue bias light (a) top cell with blue probe light (b) bottom cell with blue probe light (c) top cell with red probe light (d) bottom cell with red probe light.[11]

To measure the EQE in short-circuit conditions a small positive voltage must be applied to compensate the voltage offset [54, 55]. For a a-Si/nc-Si/nc-Si triple junction solar cell, a voltage bias of 0.7V for measuring a-si:H and 1V was used for measuring nc-Si:H by Karin Söderström et al. in 2012 [55]. When a negative bias voltage is used, the operating point of the target cell will be much further from the short circuit point as the target cell is already operating in reverse bias. The effect of reverse bias will be more significant in cells with lower shunt resistance as the current increases significantly from the short circuit point along direction of the negative voltage region [56]. This can be observed in the top cell EQE in the Figure 5.8. Thus for a cell with low shunt resistance measured with no voltage bias applied will lead to an overestimated EQE curve. A typical cell with high shunt resistance will have more or less the same current as the short circuit current even with no forward bias voltage applied. For Figure 5.8, in reverse bias the bottom cell has high shunt resistance and low electrical losses, which is why the EQEs with negative voltage bias overlaps the no voltage bias EQE. Therefore, the voltage bias is only important when we measure cells with low shunt resistances. The real EQE for the top cell might be obtained for EQE measurement with 0.5V as it might be measured in short circuit condition. The precise voltage bias that should be applied cannot be found as the operating voltage of the individual cell cannot be found in a tandem.

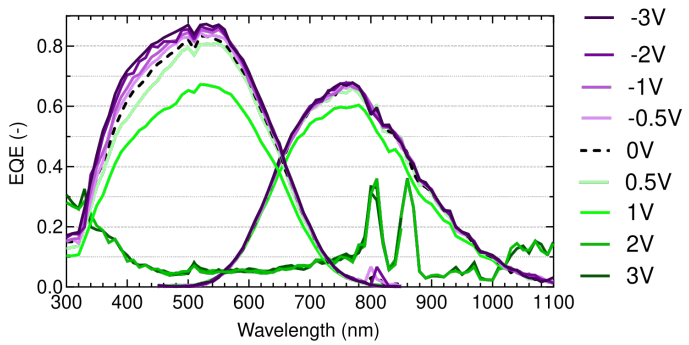

Figure 5.8: top and bottom junction EQE measured across various bias voltages with turning on 1-3 bias lights for top junction and 7-8 bias lights for bottom junction

5.5. Implementation

To solve the artifact in the EQE measurement, the learnings from the previous experiments was implemented. A solar cell that had EQE measurement error was measured again. The bias light and the probe light intensity was varied to solve the artifact.

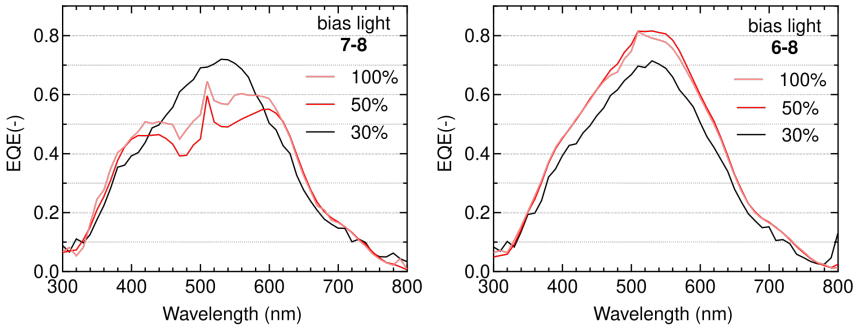

Figure 5.9: EQE of the top cell(a-Si) with variation in bias light and probe light. The probe light intensity of 30%,50% and 100% is used and bias light turned on are 7-8 and 6-8 for the graph in left and right respectively

In Figure 5.9 an attempt to rectify the observed artifact in the top cell of device using the methods previously mentioned is shown. In the left image, the intensity probe light is reduced from 100% to 30% with 7 and 8 bias light turned on. There is an improvement in the curve with decrease in the probe light intensity, but not yet the actual measurement that we want. Then, the bias light 6 was turned on. With the bias light 6-7 and 50% reduction in the probe light a smooth EQE curve was obtained. So both the methods complements each other and solves the error in the EQE measurement. Thus the reduction in the absolute EQE value is reflected on the graph.

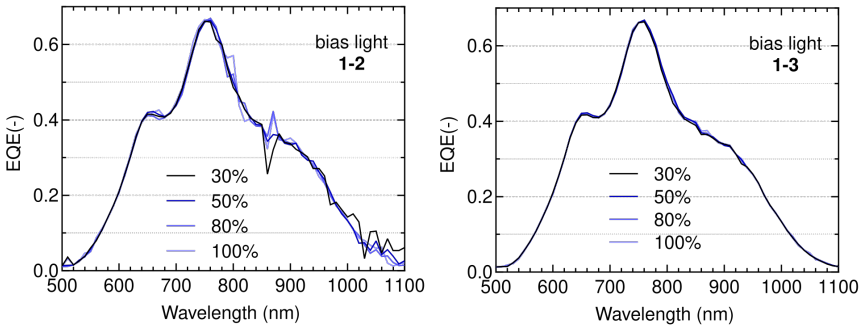

Figure 5.10: EQE of the bottom cell(nc-Si) with variation in probe light intensity and bias lights. The probe light intensities used are 30%,50%,80% and 100% and, bias lights 1-2 and 1-3 are used for the graph in left and right respectively.

A similar procedure is followed to rectify a similar problem in the bottom cell. This can be seen in Figure 5.10. The artifact was corrected in two ways. In the left graph, it can be observed that the 50% reduced probe light intensity with bias lights 1-2 turned on a smooth curve is obtained. Then, the bias lights 1-3 are turned on in the right side graph, a smooth curve is obtained irrelevant of the probe light intensity . It can also be observed that in both the Figure 5.10 and Figure 5.9, the change in bias lights has more effect on the EQE than the change in intensity of the probe light. The change in probe light intensity can be used to correct the minor errors in the EQE.

6

Optimization of p-layer

6.1. Introduction of p-layer

For optimizing the p-layer, single junction amorphous silicon solar cells were fabricated. Single junctions were chosen because the effect of structural changes to the p-layer can be better isolated better than in multi-juncitons. Also, amorphous silicon is the top cell for a multi junction thin-film silicon solar cell. p-layer for the top cell plays a crucial role to achieve high V_{oc} and great response in the blue region of the light spectrum. This will lead to high performing amorphous silicon cells. The solar cells were only deposited in p-i-n configuration. As the p-i-n configuration was the primary focus for Hyet solar, in order to replicate the recipes on aluminium foils as substrate. The desired characteristics of a p-layer from which the light enters the solar cell stack are

- High bandgap which leads to high built in voltage is required to attain high V_{oc} and also an increase in J_{sc} due to the reduction in parasitic absorption[35].
- Highly conductive contact with the TCO is preferred as it helps in achieving high *FF* [34].
- Low activation energy of p-layer will lead to increase in V_{oc} and J_{sc} due to low recombination [35].

6.2. Configuration of p-layer and materials used

In this experiment, the p-layer is divided into three layers as shown in the Figure 6.1. This was done to divide the functionalities of the p-layer within different layers.
In the order of deposition, the contact layer comes first, which is the layer after TCO. A contact layer should ideally achieve an ohmic contact with the TCO which results in in high *FF* due to low contact resistance [37]. The energy barrier between the TCO and p-layer should be low for more easier transport of holes from p-layer to TCO, this can be achieved by high conductivity and large band gap [34]. The contact layer should also have low activation energy so that the holes can easily tunnel through to the TCO [38]. It should also be thin as possible to avoid parasitic absorption. In this experiment two types of contact layer were used highly p-doped SiO_x:H and p-doped nc-Si:H (p-nc-Si). P-doped SiO_x:H (p-SiOx$^+$) was proved to have good optical and electrical to be used as a window layer [39]. p-SiO_x has structure of silicon oxide, hydrogenated amorphous silicon and also contains crystalline grains [40].
p-nc-Si is also a promising candidate for a contact layer [37]. This material is made up of amorphous silicon phase and crystalline grains. It has high transverse conductivity due its crystalline growth direction but unlike amorphous has lower optical band gap than p-SiO_x. The contact layer in a p-i-n configuration also acts a seed layer for the crystalline growth of rest of the player. Hence, the silane concentration should be low.

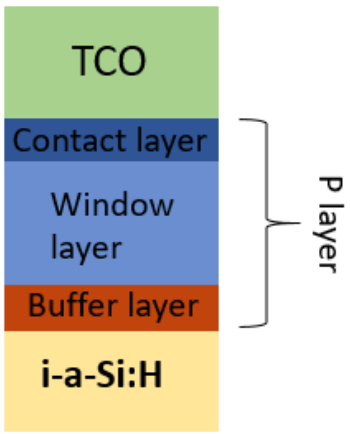

Figure 6.1: p-layer configuration consisting the contact layer, window layer and the buffer layer

The second layer is the window layer, which is expected to have high optical band gap to minimize parasitic absorption [35]. p-SiO_x:H was chosen as the window layer for this experiment due to it's good conductivity and high optical band gap[39]. The large band gap of the window layer aligns with the energy bands of the intrinsic layer, in such a way that the selectivity of holes is high [38]. The aim for this part of the layer is to obtain high selectivity for holes, high transverse conductivity and high optical transparency. The large band gap of this layer can also lead to better V_{oc} due to increase in built voltage of the material[35].

The last layer in the p-layer is the buffer layer, which is in interface between the p/i layer. The two materials that were used as the buffer layer are i-SiO_x and i-nc-Si:H. The buffer layer is expected to potentially prevent boron diffusion into i-layer and have a high band gap in the i/p interface which increases the hole selectivity and also improves the built in voltage of the cell [57].

6.3. Experimental details

The standard deposition conditions of the p-layer are show in the Table 6.1. The thickness of the absorber layer was set as 280nm. In this study the window layer was doped in both 10sccm and 30sccm F_{B2H6}.

Table 6.1: The standard deposition conditions of p-layer

p-layer		**Flow rate(sccm)**				**Pressure (mbar)**	**Power (W)**	**Thickness (nm)**	**Deposition time (secs)**
		SiH_4	H_2	B_2H_6	CO_2				
Contact layer	P-nc-Si:H	0.8	170	20		2.2	35	3	60
	P-SiOx:H+	0.8	170	50	1.2	2.2	12	3	402
Window Layer	P-SiOx:H	0.8	170	10	2.2	2.2	12	12	120
Buffer layer	i-SiOx:H	0.8	170		3.2	2.2	12	3	60
	i-nc-Si:H	0.8	170			2.2	35	3	60

In this experiment the impact on the performance of the solar cell is studied as the following properties are varied

- CO2 and diborane doping flow rate of the window layer
- Materials of contact and buffer layer
- Thickness of the contact layer, buffer and window layer

6.4. Results

In the upcoming sections d_{win} denotes the window layer thickness, d_{con} denotes the contact layer thickness, d_{buf} denotes the buffer layer thickness, F_{B2H6} denotes the diborane Flow rate and F_{CO2} denotes the CO_2 flow rate.

6.4.1. Contact layer thickness and material variation

In the Figure 6.2, it can be seen in that the V_{oc} and *FF* of the p-SiOx$^+$ (red line) material is high with approximately 0.89V and 74% respectively. This leads to an high efficiency of 10% for a single junction amorphous silicon solar cell. For the solar cell with p-SiOx$^+$ contact layer, the V_{oc} and *FF* does not vary significantly with the increase in d_{con}. However, when d_{con} is 9nm, the J_{sc} drops down from $15mA/cm^2$ to $13mA/cm^2$. Hence, the contact layer should be thin in order to decrease the parasitic absorption. There can be seen a trade off with increasing thickness with the V_{oc}, *FF* and the J_{sc}. That is, when we obtain high V_{oc}, *FF* the j_{sc} is low and the vice versa is also true. This is an important observation as this shows only an optimal point can be found between the trade off to get the best of both worlds.

The high *FF* of the solar cell with p-SiOx$^+$ might be due to the high conductivity of the material due to the high doping F_{B2H6}= 50sccm for the contact layer. The contact resistance will be reduced. The relatively high V_{oc} for the solar cell with p-SiOx$^+$ contact layer can be due the fact, it has high band gap due the oxygen content in the material [40]. The high band gap can also result from high F_{B2H6} in contact layer, as increase in F_{B2H6} results in reduction in crystallinity of the material [40]. The high band gap of the p-layer will result in increase in the built in voltage and thus lead to high V_{oc} of the solar cell. Additionally, The low activation energy due to the highly conductive p-SiOx$^+$ contact layer might also be a reason for the high V_{oc}. As the holes can tunnel through to the TCO more easily.

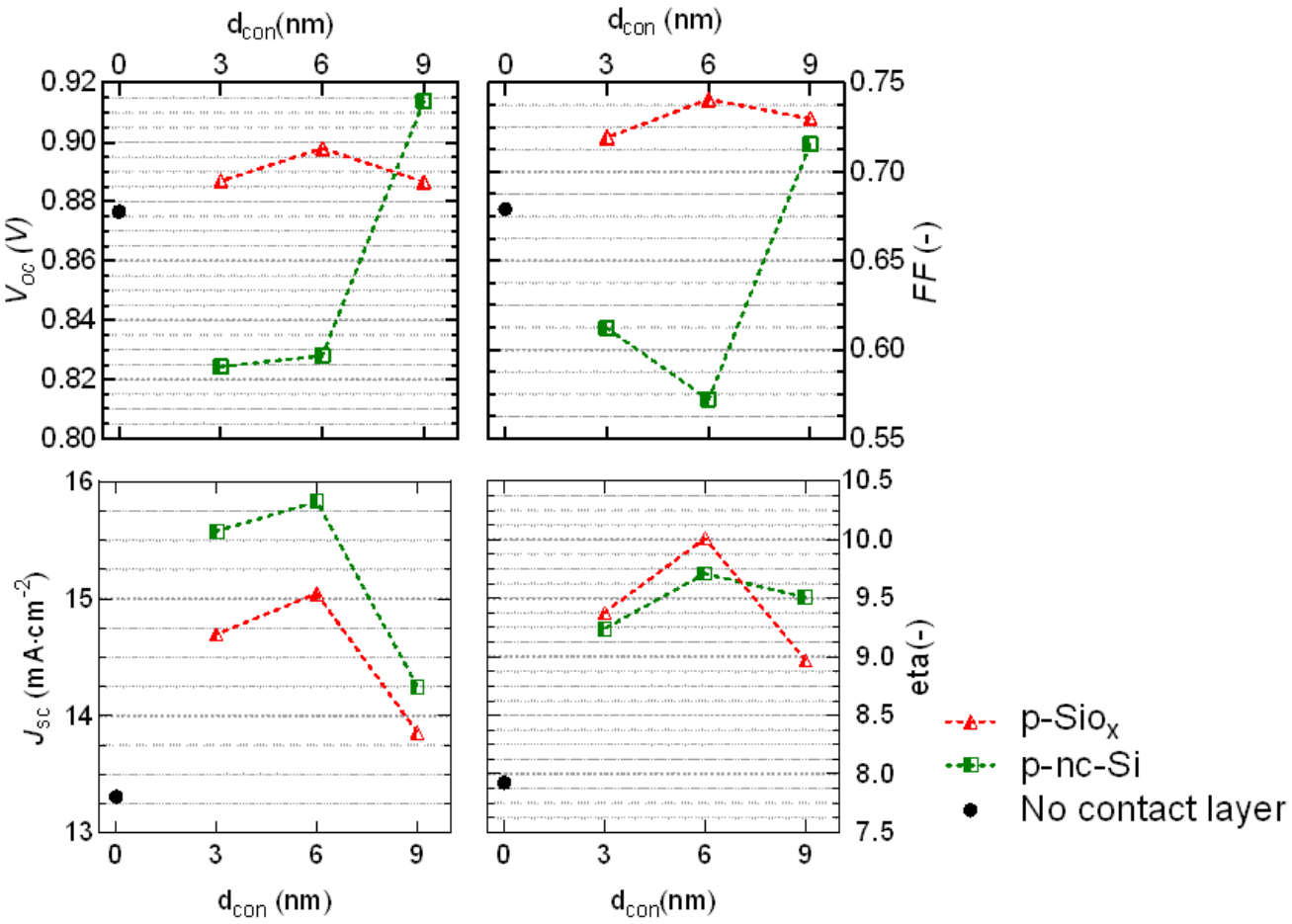

Figure 6.2: V_{oc}, FF, J_{sc} and efficiency with variation in material of contact layer and contact layer thickness (d_con) of 3,6 and 9 nm. The buffer layer is 3nm thick i-Siox and the window layer is p-SiOx with d_{win}=12nm thickness, F_{CO2}=2.2sccm and F_{B2H6}=10sccm

The Figure 6.3 shows the EQEs of the same contact layer thickness series as described in the previous paragraph. In this figure it can be seen that the in the blue light range(below 350nm) the parasitic absorption is high and the EQE value is low and with increase in contact layer thickness, the reduction in EQE can be seen clearly for the p-SiOx$^+$ material(red line) from 300nm to 500nm wavelength. Hence, a thick contact layer is not perferred due to the decrease in J_{sc}.

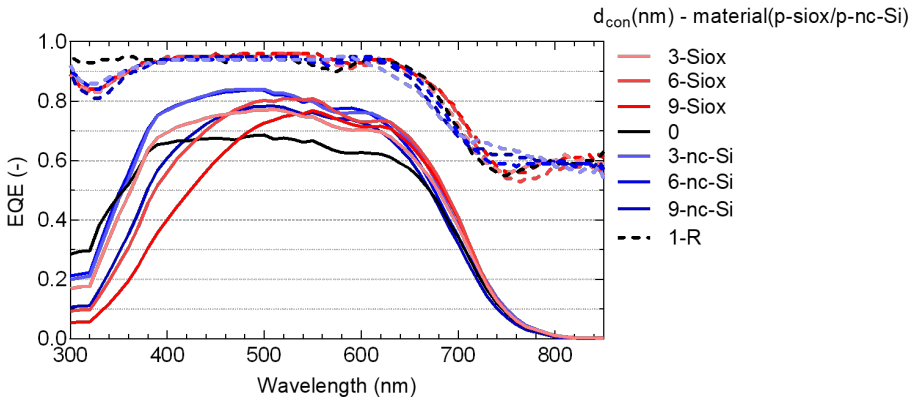

Figure 6.3: EQE of the single junction amorphous silicons with varying contact layer thickness and material

Overall, It can be said that the change in contact layer material and the thickness can vary the electrical and optical properties of the solar cell to a large extent as the V_{oc} and FF goes from 0.82V to 0.91V and 0.575% to 0.72% respectively. Same goes for the J_{sc}. Moreover, an 10% efficiency and V_{oc} above 900mV are achieved. This optimal p-layer can be eventually be used in multi-junctions to attain high efficiency. Further, thinner contact layers are preferred to reduce the parasitic absorption.

6.4.2. Buffer layer

To check the effect of the buffer layer on the performance of the cell, the thickness and the material of the buffer layer is varied.

The Figure 6.4 shows that the best efficiency is obtained with no buffer layer. It suggests that the buffer layer is not at all required for a p-i-n single junction silicon solar cell. Only the J_{sc} values of i-SiO_x is higher than the no seed layer sample. This might be due to high band gap of i-SiO_x which reduces the energy barrier for the hole transport in the interface between window layer and the buffer layer. This might also lead to the high V_{oc} in the 6nm thick i-SiO_x buffer layer sample.

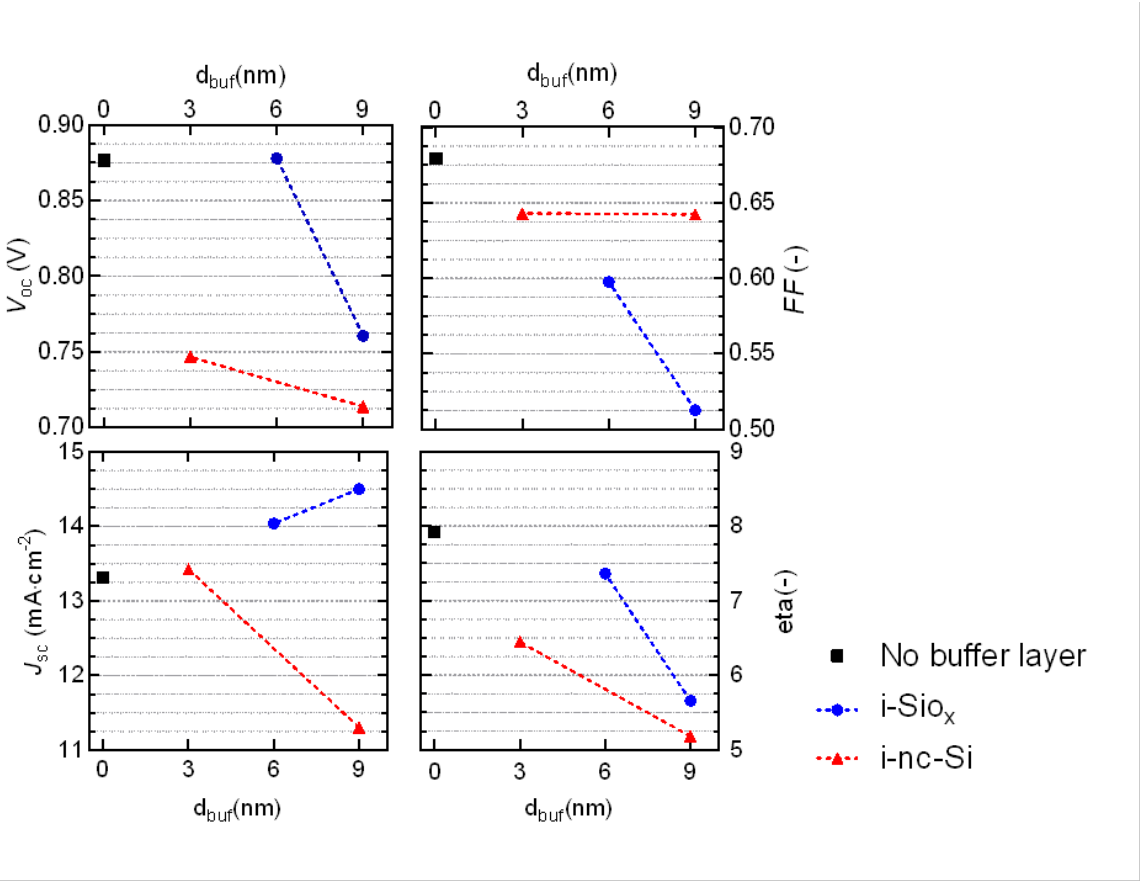

Figure 6.4: The photovoltaic optical and electrical performance with variation in buffer layer thickness(d_{buf}) of 3, 6 and 9nm is shown for both intrinsic silicon oxide(i-SiOx) and nano crystalline silicon(i-nc-Si). The contact layer is 3nm thick p-nc-Si the window layer is p-SiOx with d_{win}=12nm thickness, F_{CO2}=2.2sccm and F_{B2H6}=10sccm

6.4.3. Diborane doping of window layer

In Figure 6.5, the contact layer is p-nc-Si. It can be seen from the figure that, the cells with F_{B2H6} of 30sccm in the window layer(blue lines) have achieved efficiencies of 9.87% and 9.9%. This is due to the high V_{oc} and *FF* of 0.89 V and 71.4% respectively for the 6nm thick contact layer solar cell and the solar cell d_{con}=3nm has a high V_{oc} of 900mV and *FF* of 73.2%.
For the solar cells with window layer F_{B2H6}=10sccm the V_{oc} is lower than the solar cells with window layer F_{B2H6}=30sccm . However, the J_{sc} of the highly doped with F_{B2H6}=30sccm window layer samples are lower than the lowly doped with F_{B2H6}=10sccm window layer samples. This can be seen in the Figure 6.6. There can be seen an reduction in EQE for the 30sccm doped window layer solar cells in the 300nm to 500nm range wavelength. This reduction in the EQE can be due to the absorption due to increase in the diborane concentration in the window layer. Other possible reasons for the lower EQE might be due to the increase in parasitic absorption due to thicker window layers obtained with increase in F_{B2H6} of the window layer or it could also be due to electrical losses in the solar cell.

The high electrical performance of the F_{B2H6} =30sccm doped window layer cells can be a result of high conductivity due to the 30sccm diborane in the window layer and high band gap of the window layer. This could be reasoned by material and the electronic property relation mentioned in the subsection 6.4.1. Additionally, the window layer having a high band gap ensures high selectivity of holes from the buffer layer and leads to higher V_{oc} [35].

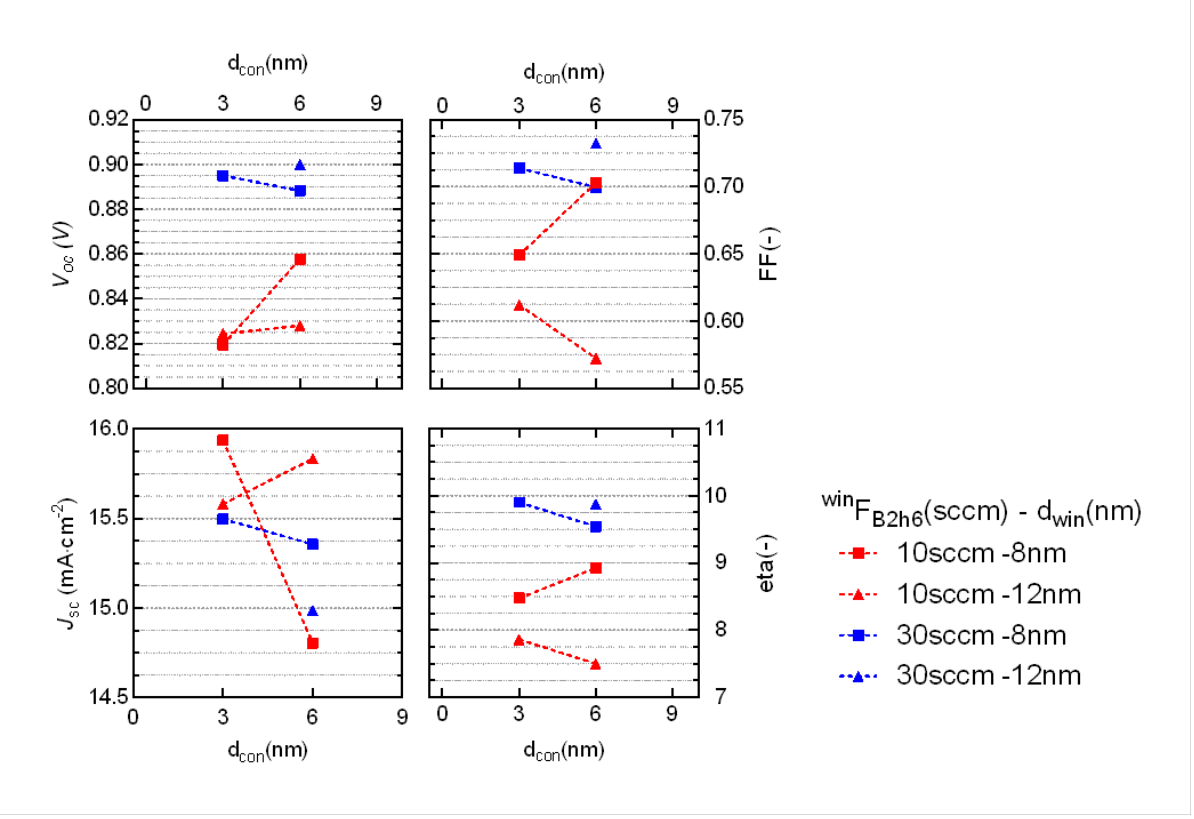

Figure 6.5: The photovoltaic electrical and optical performance of the solar cell with change in the p doping of the window layer, window layer thickness and contact layer thickness. The contact layer is p-nc-Si and $^{win}F_{CO2}$=2.2sccm. The buffer layer is 3nm thick i-Siox. $^{win}F_{B2H6}$ is the diborane flow rate in the window layer and d_{con} and d_{win} are the thicknesses of the contact layer and window layer.

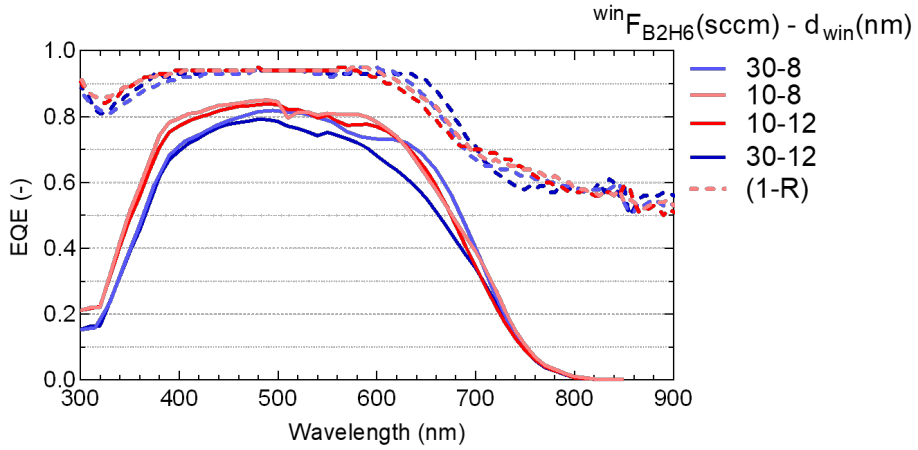

Figure 6.6: The EQE of the solar cell with varying doping flow rate and thickness of the window layer at constant thickness of buffer and contact layer of 3nm. The buffer and contact layer material used is i-Siox and p-nc-Si. $^{win}F_{B2h6}$ is the dibroane flow rate in the window layer and d_{win} is the thickness of the window layer.

The Figure 6.7 shows the same variations as the Figure 6.5, with only contact layer being changed from p-nc-Si to p-SiOx$^+$. It can be observed that, with p-SiOx$^+$ as the contact layer material, efficiency higher than 9% can be obtained for both 10sccm and 30sccm doped window layers. This is due to the high values of V_{oc} and FF with 0.88V-0.89V and 71%-74% respectively for both F_{B2H6}

of 10sccm and 30sccm doped window layer samples. This shows that p-SiOx$^+$ is better performing contact layer for a larger ranging of diborane doping flow rate of the window layer than the p-nc-Si contact layer. This also shows the importance of the contact layer. That with a good contact layer like p-Siox, high electrical performance can be achieved even with low F_{B2H6} as 10sccm. However, a 10% efficient solar cell can be achieved in both the contact layer materials by varying the diborane doping flow rate of window layer and thickness of the contact layer.

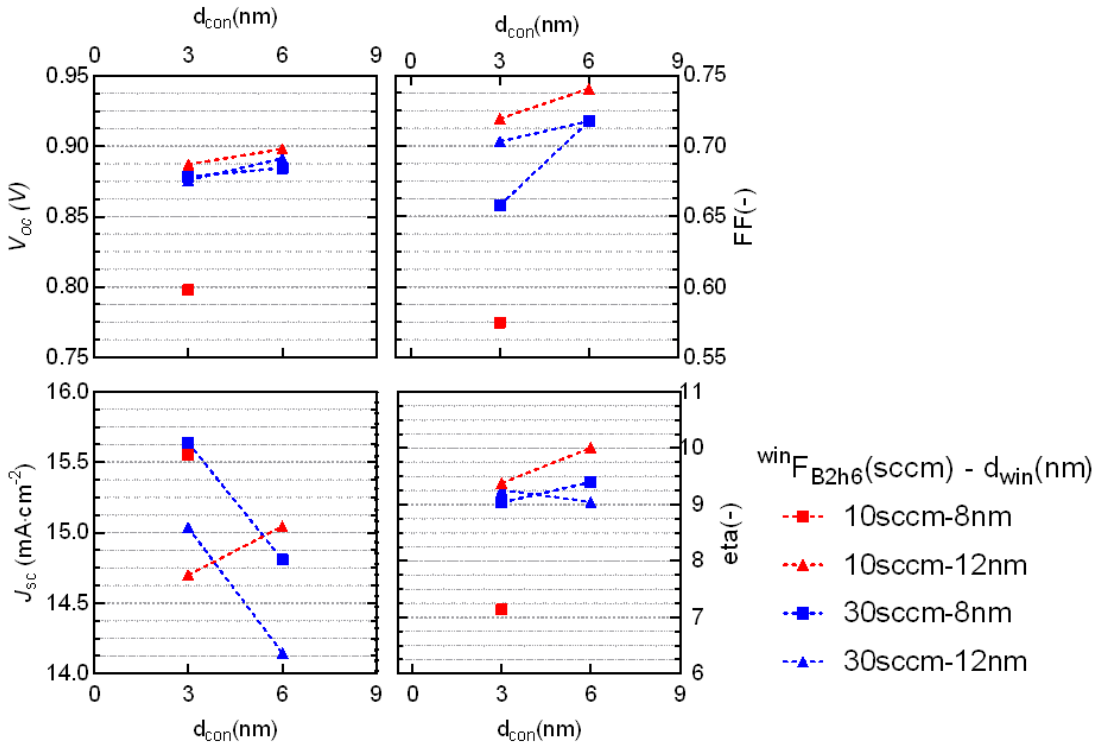

Figure 6.7: The electrical and optical performance of the solar with change in the p doping of the window layer, window layer thickness and contact layer thickness. The contact layer is p-SiOx and $^{win}F_{CO2}$=2.2sccm. The buffer layer is 3nm thick i-Siox. $^{win}F_{B2H6}$ is the diborane flow rate in the window layer and d_{con} and d_{win} are the thicknesses of the contact layer and window layer.

6.4.4. CO_2 flow rate of window layer

In the Figure 6.8, the cell with F_{CO2} =3.2sccm (blue dot) has high V_{oc} and J_{sc} but also has the lowest *FF* and efficiency. Therefore, the F_{CO2} should not be high as 3.2sccm with 16nm thick window layer for the p-layer. Further, the highest efficiency achieved in this case is 9.2% for the solar cell with 2.2sccm CO_2 flow rate and 16nm thick window layer.

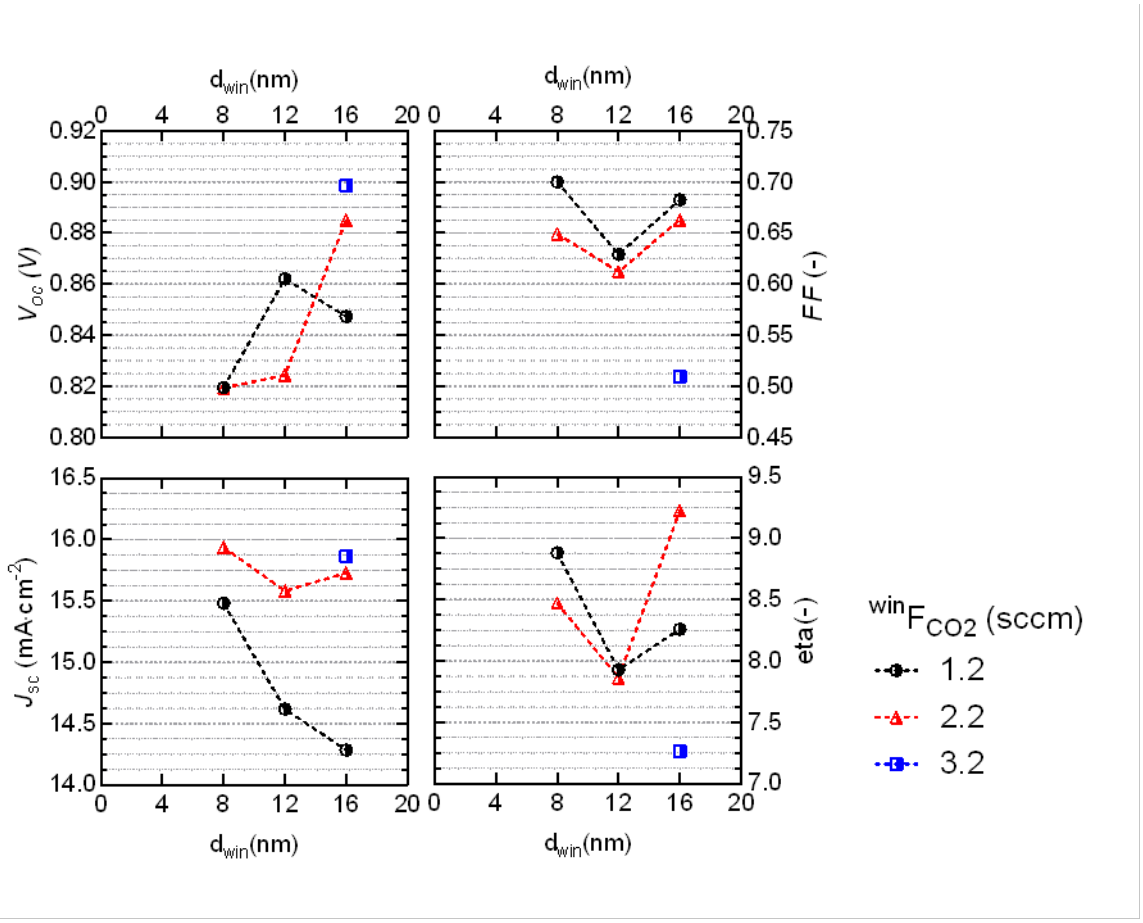

Figure 6.8: The variation in the Co_2 flow rate in the window layer with the window layer thickness at ${}^{win}F_{B2H6}$=10sccm. The buffer layer is 3nm thick i-Siox and the contact layer is p-nc-Si with 3nm thickness. ${}^{win}F_{CO2}$ is the CO_2 flow rate in the window layer and d_{win} is the thickness of the window layer.

In F_{B2H6}=30sccm doped window layer shown in Figure 6.9, it can be seen here that the single junction amorphous cells achieve high efficiencies of 9.9% and 9.6% for the window layer with 2.2sccm CO_2 flow rate. This due to the high V_{oc}, FF and J_{sc} of 0.89V, 0.71% and 15.49mA/cm^2 respectively for the 9.9% efficient device. Thus, it can be said that high efficiencies can also be achieved by changing the window layer deposition conditions without changing the contact layer thickness and material. A bi-layer configuration is needed to attain a highly efficient p-layer as both the contact layer and the window layer have a large impact on the performance of the cell. Further, The dip in the values for 12nm = d_{win} devices can be seen. Those cells were shunted due to improper deposition. The lower J_{sc} of the device having 3.2 sccm =F_{CO2} for the window layer is examined from the Figure 6.10.

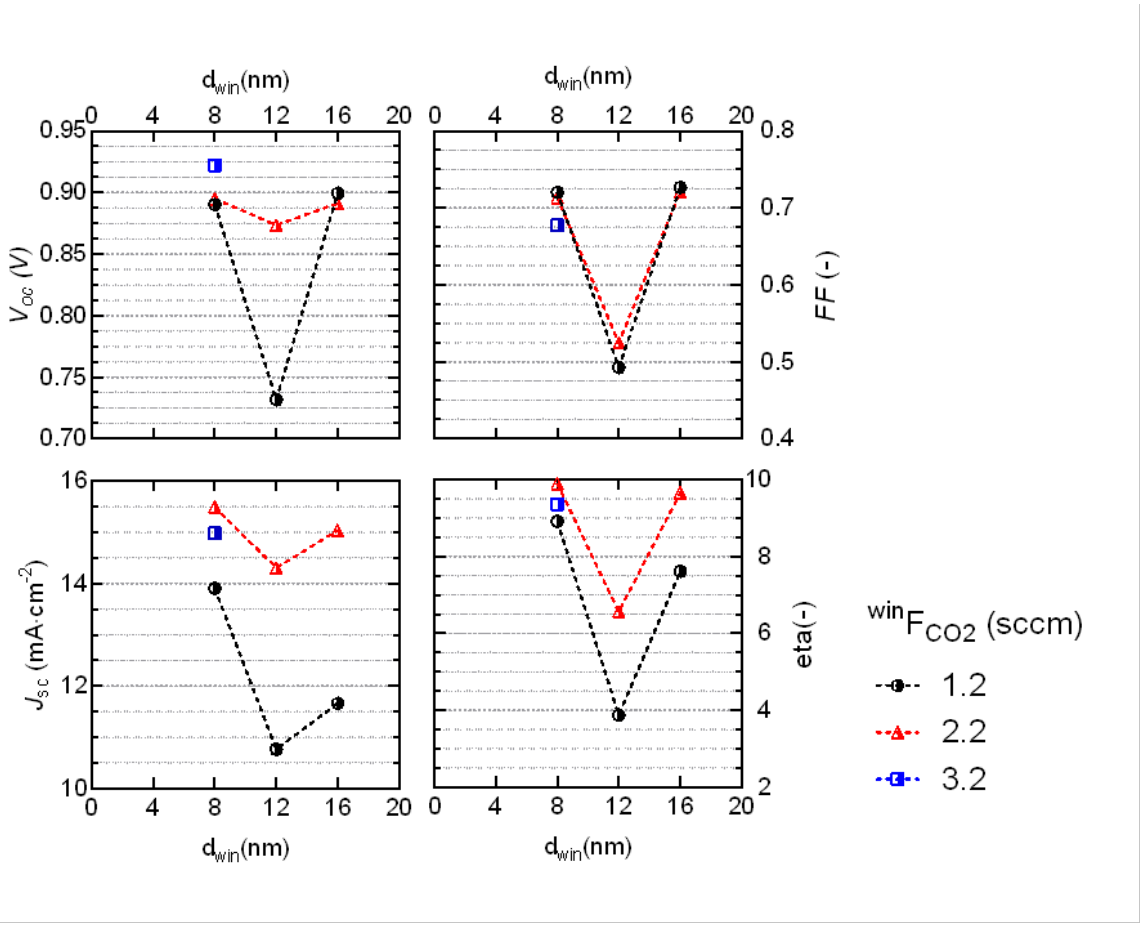

Figure 6.9: The variation in the Co_2 flow rate of the window layer with the window layer thickness at ${}^{win}F_{B2H6}$= 30sccm. The seed layer is 3nm thick i-Siox and the contact layer is p-nc-Si with 3nm thickness. ${}^{win}F_{CO2}$ is the CO_2 flow rate in the window layer and d_{win} is the thickness of the window layer.

In Figure 6.10, it can be seen that the EQE in the blue wavelength range increases as the CO_2 flow rate increases for a particular thickness of the window layer. This is due to the energy gap increase as the oxygen content in the material increases. Less light is absorbed in the p-layer with increase in band gap. However, the EQE of the cell with highest CO_2 flow rate for 8nm=d_{win} has overall low J_{sc} compared to the cell with 2.2sccm CO_2. This might be due to the low refractive index obtained due to the increases in oxygen concentration. The low refractive index can cause total internal reflection in the longer wavelengths (above 500nm) which can lead to optical losses. The increase in parasitic absorption can also be witnessed with increase in thickness of the window layer from 8nm to 16nm.

The increase of V_{oc} with the concentration of oxygen is due to the same reasons that are already explained in subsection 6.4.1. The increase in oxygen content can also lead to low electrical conductivity. [58]. This low conductivity might be the reason for the low *FF* for solar cell with F_{CO2}=3.2sccm window layer.

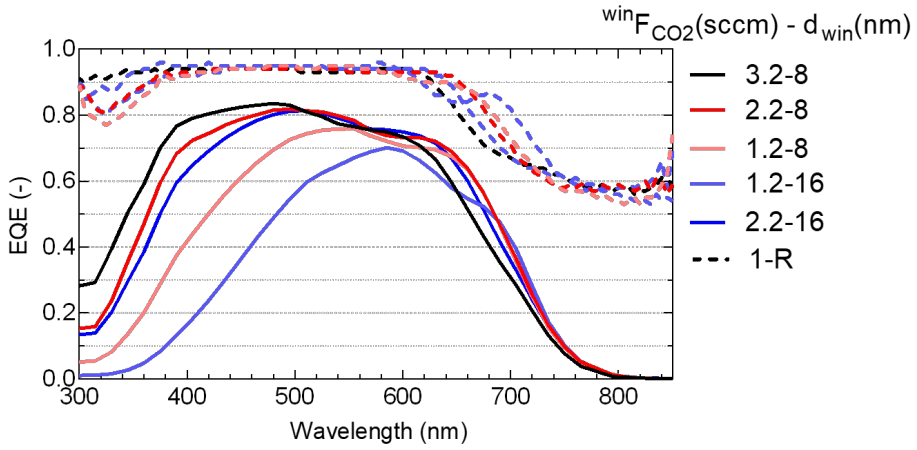

Figure 6.10: EQE of single junction amaorphous silicon cells with varying CO_2 flow rate and thickness of the window layer. Constant diborane flow rate of 30sccm in the window layer and p-Siox as the contact layer. ${}^{win}F_{CO2}$ is the CO_2 flow rate in the window layer and d_{win} is the thickness of the window layer.

6.5. Further optimization of p-layer

A new p-layer optimization study was conducted by implementing the new learnings from the previous results. In this study, single junction amorphous silicon were fabricated without any seed or buffer layer in the i/p interface. Furthermore, the contact layer material was chosen as p-SiOx$^+$. These changes were made due to conclusions drawn from the previous p-layer optimization study. In this new series the p-doping concentration on contact layer was varied with thickness of window and contact layer. This was done to test the performance of the solar cell for a range of doping concentration and to know if high amounts of dopant in the contact layer can give an extra push in the performance of the solar cell. In this approach the total p-layer thickness was kept constant and the fraction of thickness between the window and contact layer was varied. This was done to know the desired thickness of the contact and the window layer. Also, to study dependence of the behaviour of the solar cell on the thickness ratio of the p-layer.

6.5.1. Contact layer doping series

In this section we study the variation of doping concentration of the window layer and the contact layer for various thickness fraction of the p-layer.

Based on Figure 6.11, it is clear that high efficiency is obtained for solar cells with d_{con}=3nm and F_{B2H6}=10 sccm for the window layer(red line). The obtained high efficiencies are approximately 9.24% for the 20sccm and 80sccm doped contact layer. Even though the V_{oc} is low as 0.83V for contact layer with F_{B2H6}=20sccm doping, it has as high J_{sc} of 16.21mA/cm^2. This can seen in the Figure 6.12. The EQE of the solar cell with F_{B2H6}= 20sccm doped contact layer has high collection of charge carriers in the low wavelength region(300nm-500nm) compared to the other solar cells. This means it has low electrical losses compared to the other samples as the absorptance is lower for F_{B2H6}=20sccm contact layer sample than the other samples in the graph. A high V_{oc} of 900mV is achieved for the sample with F_{B2H6}=30sccm in the window layer.

There can also be seen a common trend in Figure 6.11, Figure 6.13 and Figure 6.11 of V_{oc} increasing with the increase in diborane flow rate in the contact layer when window layer is doped with F_{B2H6}=10sccm. This can be a result of increase in conductivity and decrease in activation energy due to increase in F_{B2H6} in the contact layer. Refer to subsection 6.4.1.

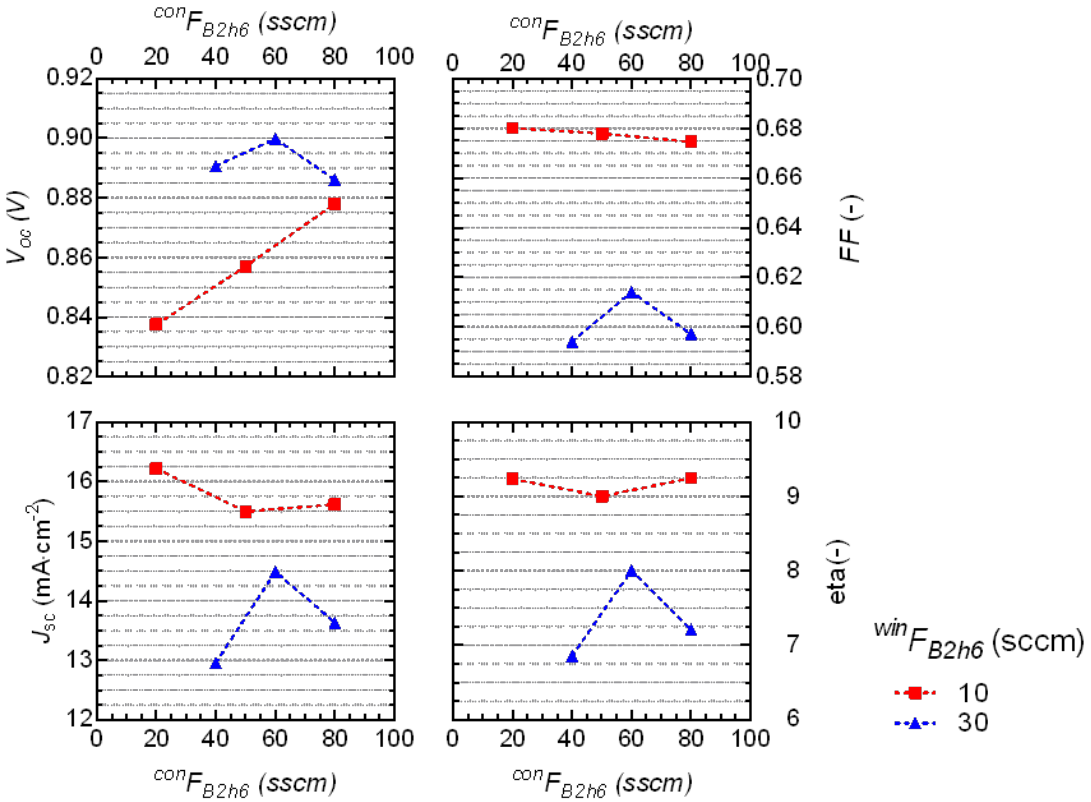

Figure 6.11: $^{win}F_{B2H6}$ and $^{con}F_{B2H6}$ are the diborane flowrate in the window layer and contact layer respectively. Variation of $^{win}F_{B2H6}$ and $^{con}F_{B2H6}$ with optical and electrical performance of the solar cell. d_{con}=3nm and d_{win}=13nm

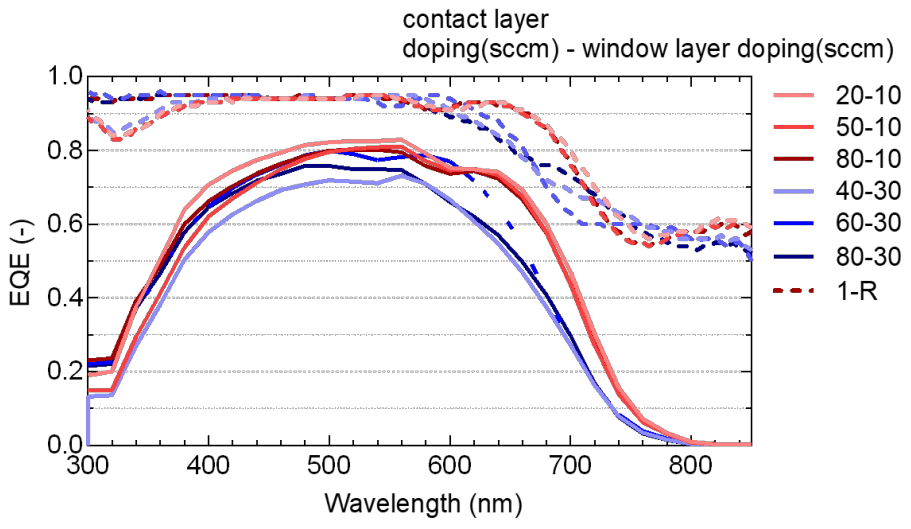

Figure 6.12: EQE and absorptance curve of the solar cells with variation in dibronae flow rate of the window and the contact layer. d_{con}=3nm and d_{win}=13nm

For the a-Si solar cell with d_{con}=6nm in Figure 6.13, it can be observed that the solar cells with F_{B2H6}=30sccm and F_{B2H6}=10sccm window layers perform similarly in this case. Both doping flow rates attained similar maximum efficiencies of 9.25% and 9.16% respectively. A thicker contact layer and thinner window layer than in Figure 6.11 is used. This means that the contact layer thickness and the diborane doping flow rate of the window layer is related. In Figure 6.13 there can also be seen a decrease in performance with increase in F_{B2H6} after 50sccm of contact layer for the F_{B2H6}=10sccm doped window layer cells.

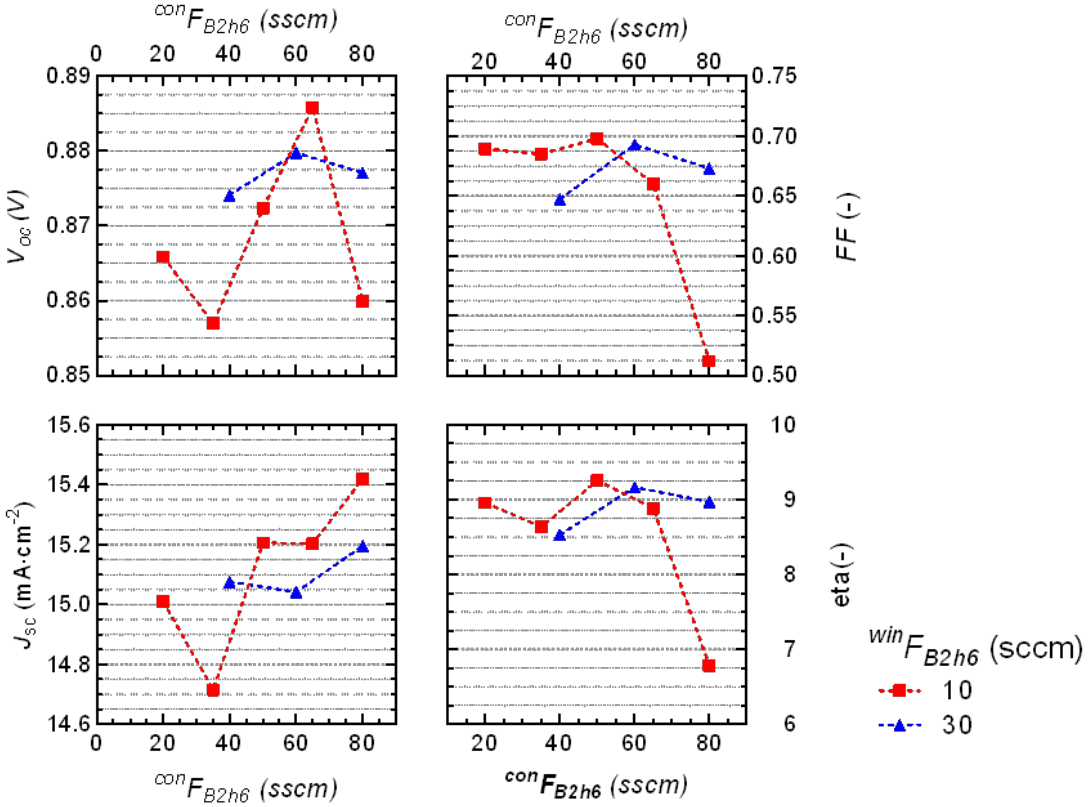

Figure 6.13: ${}^{win}F_{B2H6}$ and ${}^{con}F_{B2H6}$ are the diborane flowrate in the window layer and contact layer respectively. Variation of ${}^{win}F_{B2H6}$ and ${}^{con}F_{B2H6}$ with optical and electrical performance of the solar cell. d_{con}=6nm and d_{win}=10nm

The solar cells with F_{B2H6}=10sccm doped window layer has low efficiency from 7.6% to 6.2% efficiency for 8nm =d_{win}=d_{con}. This can be observed in Figure 6.14. Therefore, for contact layer as thick as 8nm with F_{B2H6}=10sccm doped window layer leads to low efficiency compared to the solar cells with other two thickness fraction. The thicker contact layer needs F_{B2H6}=30sccm doped window layer to achieve higher efficiencies. However, the highest efficient solar cell with 8nm thick contact layer is below 9%. Whereas, the 3nm thick contact layer solar cell attained an efficiency of 9.2%. The difference in efficiency can be due to the value of J_{sc}. The J_{sc} in Figure 6.11 for the F_{B2H6}=10sccm doped window layer is above $15mA/cm^2$ but, J_{sc} for the 8nm contact layer in Figure 6.14 is lower than $15mA/cm^2$. This is due to the increase in parasitic absorption due to thicker contact layer. This can be seen in Figure 6.15. As the contact layer thickness reduces, the EQE in the wavelength range 300nm to 550nm increases.

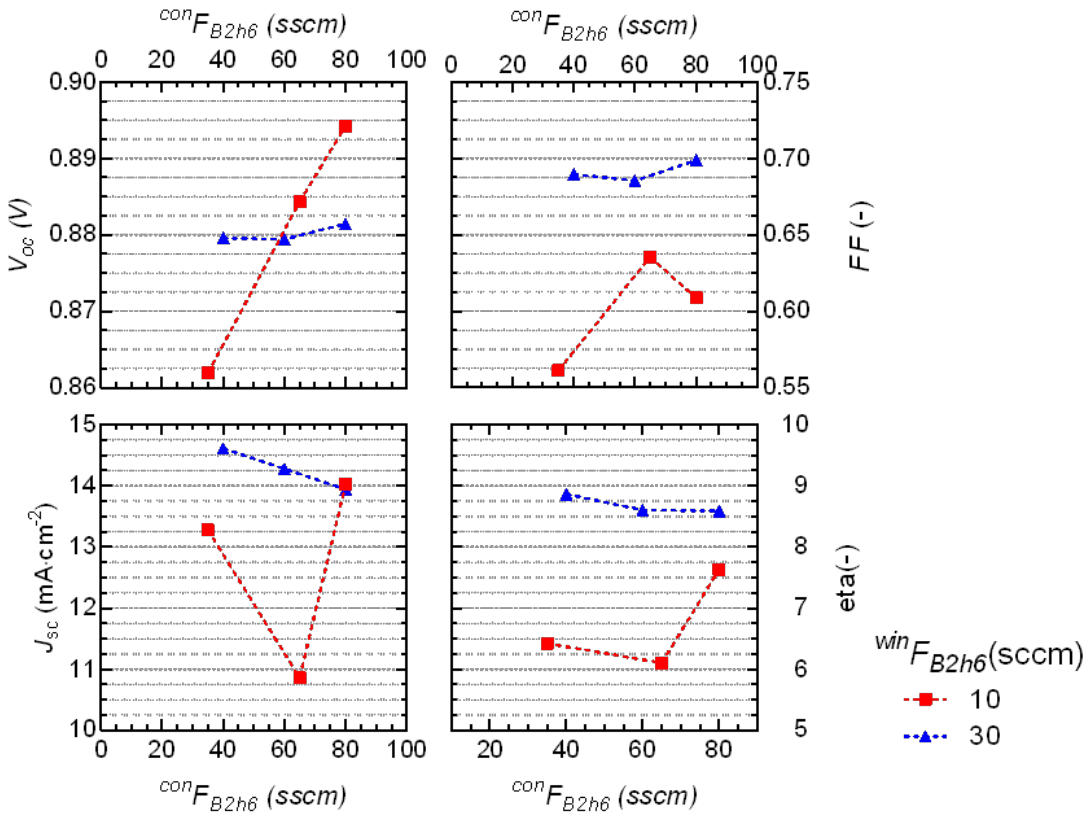

Figure 6.14: $^{win}F_{B2H6}$ and $^{con}F_{B2H6}$ are the diborane flowrate in the window layer and contact layer respectively. Variation of $^{win}F_{B2H6}$ and $^{con}F_{B2H6}$ with optical and electrical performance of the solar cell. d_{con}=8nm and d_{win}=8nm.

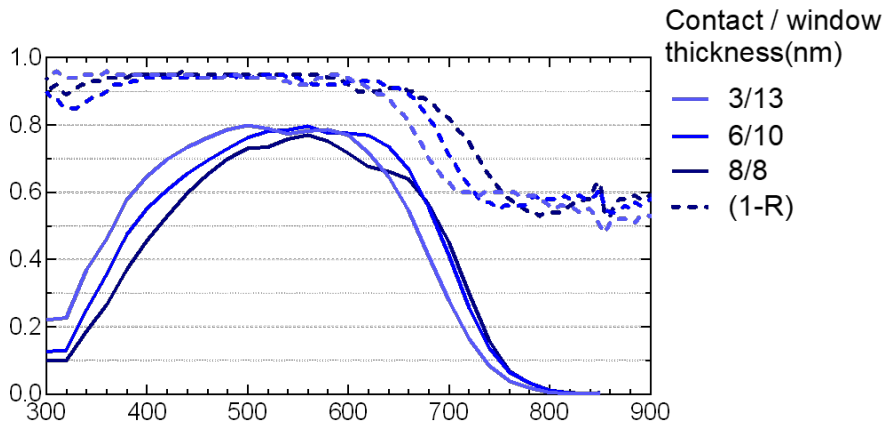

Figure 6.15: EQE and absorptance curve of different thickness fraction of the p-layer with a constant doping flow rate of 30sccm and 60sccm for the window and contact layer respectively

It can also be said that for a thicker contact layer the efficiency can be improved with increasing the diborane flow rate of the window layer. Perhaps, further increasing the doping flow rate of the

window layer might lead to higher efficiency than the efficiency that is obtained now at 8nm thick contact and window layer.
with low thickness (8nm) of the window layer might have a high crystalline fraction compared to the thicker window layers. As the window layer thickness increases the crystalline fraction reduces. The crystal growth cannot be maintained over greater thicknesses in the transverse direction. The positive effects of diborane are obtaining high band gap and increasing the conductivity for the p-layer. However, increasing concentration of the dopant will also lead to a reduction in the crystallinity of the material [38].
The current trend observed might be due to the fact that in the 13nm thick window layer with high F_{B2H6} of 30sccm affects the crystalline growth and leads to less cyrstallinity of the material. As the window layer is thick (13nm), proper crystalline growth might not be maintained along-with the thickness of the material. The increase in doping concentration might add to this effect. This effect will dominate the performance of the p-layer than the decrease in activation energy and increase in band gap due to higher doping concentration. When window layer is as thin as 8nm, which results in maintaining, proper crystalline growth throughout the material thickness and high doping flow rate such as 30sccm is handled without much reduction in crystallinity in the window layer. Thus, the decrease in activation energy and increase in band gap dominates and has less effect on the cyrstallinity of the material as it is thin and leads to better performance for the 30sccm doped window layer.

Overall, through the p-layer optimization experiments an a-Si single junction solar cell with a conversion efficiency of 10% and a V_{oc} of 910mV was obtained. It was also observed that the addition of the buffer layer did not show any significant improvement in the performance of the solar cell. Further, both the window layer and contact layer of the p-layer had a high influence on the performance of the solar cell. Hence, a bi-layer configuration is required for the p-layer. p-SiOx$^+$ contact layer resulted in good performing solar cells for larger range of F_{B2H6} in the window layer than p-nc-Si contact layer.
In further optimization of the p-layer, the best efficiencies of 9.24% were obtained for a thin contact layer of 3nm and 13nm thick window layer with F_{B2H6}=50sccm to F_{B2H6}=65sccm doped contact layer and 10sccm doped window layer. However, a thick contact layer can be compensated by increasing the F_{B2H6} doping of window layer. Consequently, there are multiple ways to attain a optimal p-layer. These are the main takeaways despite the sample to sample variations within each run.

7

Comparison of textures

The objective of this study was to compare the performance of different textures in micromorph and triple junction (a-Si/nc-Si/nc-Si) solar cells. This was done to find out the best suitable texture for obtaining high performance. The texture should cause a large amount of light scattering in the absorber layers and also should not be detrimental to the electrical properties of the solar cell. The performance of nc-Si:H solar cells are significantly influenced by the substrate morphology. Rough textures act as a good scatterer of light in the solar cells which significantly improves the optical performance of the solar cell. However, v-shaped rough and sharp textures creates cracks during the growth of nc-Si:H. This leads to recombination losses which leads to reduction V_{oc} and FF [29]. These cracks are formed at the focal point between the slopes of textured features. Hence, discovering the optimal texture for micromorph and triple junction solar cell by exploring different textures obtained by various methods is important.

7.1. Introduction to the textures used

Few of the textures that were chosen for the experiments are shown in Table 7.1.
Hitoshi Sai in 2013 achieved a J_{SC} of 30 mA/cm^2 in a 3μm thick cell and an active area efficiency of 10.7% in a 2μm thick absorber layer cell, in a nc-Si single junction solar cell with the honeycomb periodic. This demonstrates a significant potential benefit for periodic honeycomb textures [32, 33]. Honeycomb texture is a micro texture with periods of few microns as mentioned in chapter 4.

Thierry in 2021 showed that a crack free growth of nc-Si on acid etched pyramidal texture [31]. The pyramids are smoothened as when it was etched for 5 mins. He has also showed it has excellent scattering properties [31].Multiple reflection events dominates the reflection mechanism through which light-incoupling is realized. These reflection events will be reduced as the etching time increases due to the decrease in slope of the feature. To explore and compare the performance of this texture with the other textures, solar cells with this particular texture was fabricated.

Kluth in 1999 showed that morphologies with different crater sizes can be obtained by etching AZO that is deposited with different pressures. The sharpness of the textures increases with the pressure. A feature size of 200–600nm was obtained by etching a AZO layer deposited at 5 mtorr pressure using RF magnetron sputtering [30]. High efficiencies in a-si and nc-si single junction and micromorph devices are shown with AZO texture having feature size near 200nm [30, 59, 60].

Microtextures acquired on the glass substrate through the etching of a sacrificial ITO layer using the technique mentioned in the chapter 4. This technique was used by Hairen Tan in 2015 to make

the same microtextures. Yet, we obtained a different morphology and roughness in the substrate compared to the Hairen tan's substrate(HT). The AFM image of both the substrate can be seen in chapter 4. All these textures were proven to improve efficiency of the thin-film silicon solar cells. Hence, we selected these textures to make a comparison between their performance.

7.2. Experimental details

In the n-i-p configuration the smooth pyramidal and the honeycomb textures were made by etching as mentioned in chapter4. The smooth pyramidal texture was etched for 3 different times 5, 8 and 11 minutes. The solar cells with smooth pyramidal textures are named S11,S8 and S5. 'S' denotes the smoothened pyramid texture and the number denotes the etching time.
Honeycomb textures with two different masks with varied periods were fabricated. The two periods were $3\mu m$ and $2\mu m$. The etching time for the small period was 12 minutes, which was also the standard etching time for honeycomb. The honeycomb texture with larger period was etched for 16 minutes. The solar cells with honeycomb texture were named as H12S and H16L. 'H' denotes the honeycomb texture, number denotes the etching time and, the 'L' and 'S' denotes the large ($3\mu m$) and small period ($2\mu m$) respectively.
The substrates with ITO and AZO etched textures were used to deposit the photo active stack. The ITO was deposited at room temperature as the heater inside the ZORRO machine was not working. However, the ITO was annealed at 400°C. AZO was deposited in the AMIGO by sputtering. It was deposited at 400°C, with power of 400W for 3600secs. The Hiren Tan(Ht) glass is the substrate with which the record efficiency of thin-film silicon solar cell was made in pin configuration [27]. The Figure 4.7 shows the AFM image of all three textures. It can be seen that the roughness of the Ht textured substrate is the highest and the AZO textured sample is the lowest. The solar cells on the actual texture made by Hairen Tan is called 'Ht' sample.
Annealing the ITO leads to growth of polycrystalline material which make the ITO hetrogenous. Due to this, texturing is possible as the chemical will etch it anisotropically. Nonetheless, The ITO and AZO etched substrate did not not have uniform texture all over the substrate. The substrate was textured in some parts and also had flat glass in some parts. This might be because of the annealing of the substrate after deposition. The annealing may have lead to crystallisation of only some parts of the TCO. Hence, the texture was not so significant for some part compared to other regions. The table contains the data of the rough and textured region.
For the n-i-p configuration, HT, AZO, ITO, smooth pyramidal and honeycomb textured substrates were used for the deposition of the solar cell. Only the HT, AZO, ITO and Asahi textured substrates were used to fabricate p-i-n solar cells. This was because of the honeycomb and smooth pyramidal textures were only made on silicon wafers. Additionally, as the Asahi glass has FTO on top of the textured part of the glass, it cannot be further utilized for n-i-p configuration. The micromorphs were fabricated with absorber layer thicknesses of 230nm for the top cell and the bottom cell was fabricated with two thicknesses of $1.5\mu m$ and $2.5\mu m$. The top, middle and bottom cell thicknesses of the triple junction device are 200nm, $1.5\mu m$ and $2.2\mu m$ respectively.

Table 7.1: The Root-mean-square roughness(R_{rms}) for the Honeycomb texture with large period and 12 minutes etched(H L12), smooth pyramidal texture with etching time of 5, 8 and 11 minutes and ITO and AZO sacrificial texture and the Hairen tan's textured substrate(HT)

Texture	R_{rms}**(nm)**
Honey L12	270
Smooth 5	228
Smooth 8	208
smooth 11	169
ITO	141
AZO	17.7
HT	707
Asahi[61]	42

7.3. Results

7.3.1. p-i-n tandem devices

In this section performance of micromorph devices on different textures in p-i-n configuration are discussed.

In Figure 7.1, it can be noticed, for the solar cells with Ht, ITO and AZO textures with 2.5μm thick bottom cell has a poor optical and electrical performance compared to the samples Asahi texture glass. The EQEs for these solar cells can be seen in Figure 7.3. Ht, ITO and AZO texture samples has a low EQE for both top and bottom cells compared to the EQE of the Asahi. This might mean that both the top and bottom cells have a common problem such as the TCO or common doped layers. Further, the series resistances were 164,72$\Omega.cm^2$ and 110$\Omega.cm^2$ for the AZO, ITO and Ht textured samples, which is high compared to the series resistance of Asahi textured solar cells with 10.28$\Omega.cm^2$.

The high performing solar cells on Asahi textured substrate with an nc-Si absorber layer thickness of 1.5μm and 2.5μm reaches efficiencies of 9.8% and 11.48% respectively. This increase in efficiency with the increase in the bottom cell thickness attributes to the increase in J_{sc} of the bottom cell. This can be seen by comparing the Figure 7.2 and Figure 7.3. The bottom cell has a better absorption for 2.5μm in the wavelength range of 700nm to 1100nm due to increase in the nc-Si absorber layer thickness. The higher *FF* of 74% for the 1.5μm thick bottom cell sample compared to the *FF* of 70.6%the 2.5μm thick bottom solar cell is achieved. This is due to the higher mismatch current between the bottom and top cell for 1.5μm thick bottom cell sample. Fill factor compensation occurs due to current mismatch. The difference in series resistance of the both solar cells are not significant. Hence, the lower *FF* is only attributed to the *FF* compensation.

The recipe used to make all the samples for different substrate were the same including Asahi substrate. Only the TCO deposited was different for the Ht, AZO and ITO textured samples compared to the Asahi substrate sample. The front contact TCO could be the reason for the poor performance of ITO, HT and AZO textured solar cells as it was not optimized to be used for a solar cell. The TCO might not have the preferred electrical and optical properties. The ITO was deposited as the TCO for ITO, AZO and Ht textured solar cells. The thickness of the ITO was found to be approximately 300nm. The 300nm on unoptimized TCO might have low sheet resistance and high free charge carrier absorption. Until the TCO is optimized, the textures used cannot be compared with the solar cell on Asahi using J_{sc} and *FF* as a metric. As Asahi substrate has FTO deposited with standard thickness of 650 nm as the TCO.

Another possible reason for the low electrical performance of the Ht, ITO and AZO textured solar cells might also be due to the metallic probes used for measuring the p-i-n configuration solar cells in WACOM. These probes can press and hit the sample too hard and might cause damage to the front

contact. The corning glass used for these textures are comparatively thinner than the Asahi glass. The damage of the solar cell during measurement can also cause the electrical losses. The Asahi glass is thicker and has very thick FTO which can withstand the metallic probes pressed against the sample.

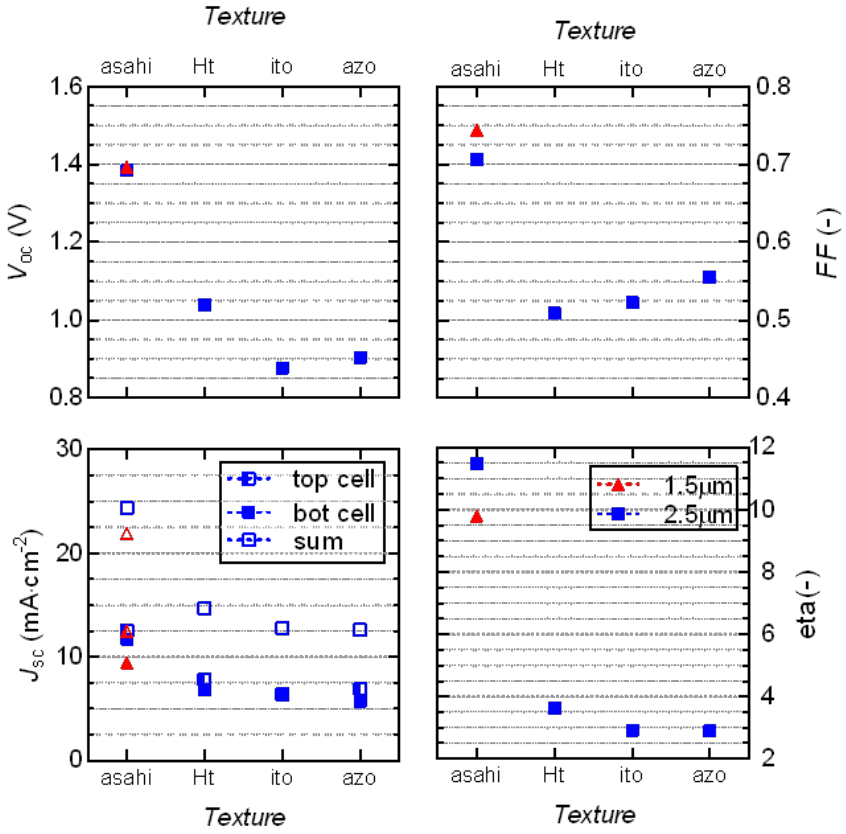

Figure 7.1: The variation of optical and electronic performance of the miromorph solar cell with Asahi texture, Hairen tan's texture(Ht), ITO etched and AZO etched on glass textures in p-i-n configuration for bottom cell thickness of 1.5μm and 2.5μm

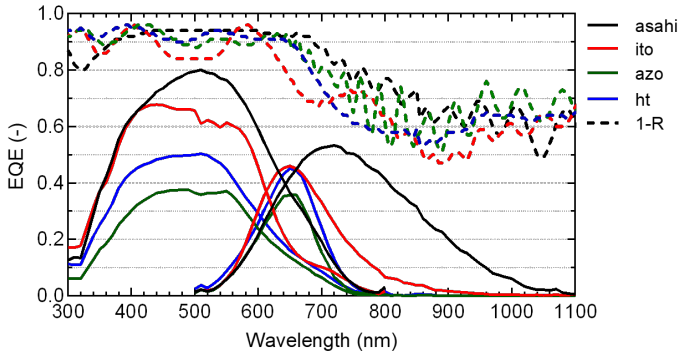

Figure 7.2: EQE of micromorphs in p-i-n configuration with 1.5μm thick absorber layer of bottom cell on various textures

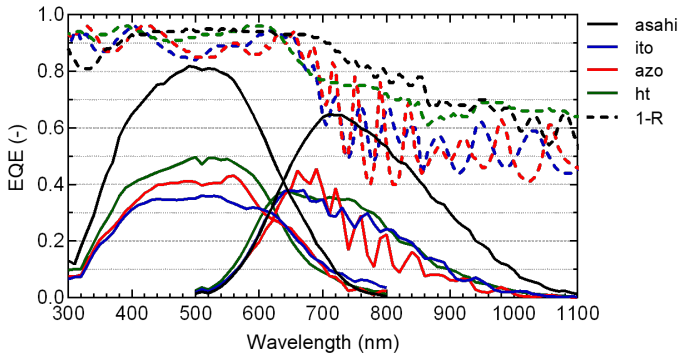

Figure 7.3: EQE of micromorphs in p-i-n configuration with 2.5μm thick absorber layer of bottom cell on various textures

7.3.2. p-i-n triple junction devices

In this section, the results from the triple junction solar cells (a-Si/nc-Si/nc-Si) which were deposited in p-i-n configuration on Ht, AZO,ITO and the Asahi substrates are discussed and analyzed. The Figure 7.4 shows that the Ht, ITO and AZO textured solar cells have low efficiencies. In the Figure 7.5, the EQE and the absorptance curve can be seen. It shows that the absorptance of the AZO, ITO and Ht textured samples in the short wavelength region is higher than the Asahi substrate solar cell, but the EQE value is significantly lower than the Asahi textured solar cell. This means the light is absorbed somewhere other than the absorber layer, it has high chance of getting absorbed by the TCO. Hence, the amount of light that enters the absorber layers decreases by a significant amount. However, in the red and infra red wavelength region there is drastic decrease in the absorptance for ITO, and AZO textured solar cell. This means that the light is mostly getting reflected as we assume the transmission is negligible through the solar cell. The light is not scattered in the red and infra red region well enough for the absorber layers to absorb the light. This is probably due to the non-uniform textured surface of both the ITO and AZO etched textures. Some parts of the substrate were flat and some parts of the substrate were textured. The AFM image in Figure 4.7 only shows the valleys and craters of the textured portion. The poor electrical performance the of the HT, AZO and ITO textured solar cells could be due to the measurement and TCO related issues as mentioned in subsection 7.3.1. Also, maybe due to high series resistance of these cells(>150 $\Omega.cm^2$).

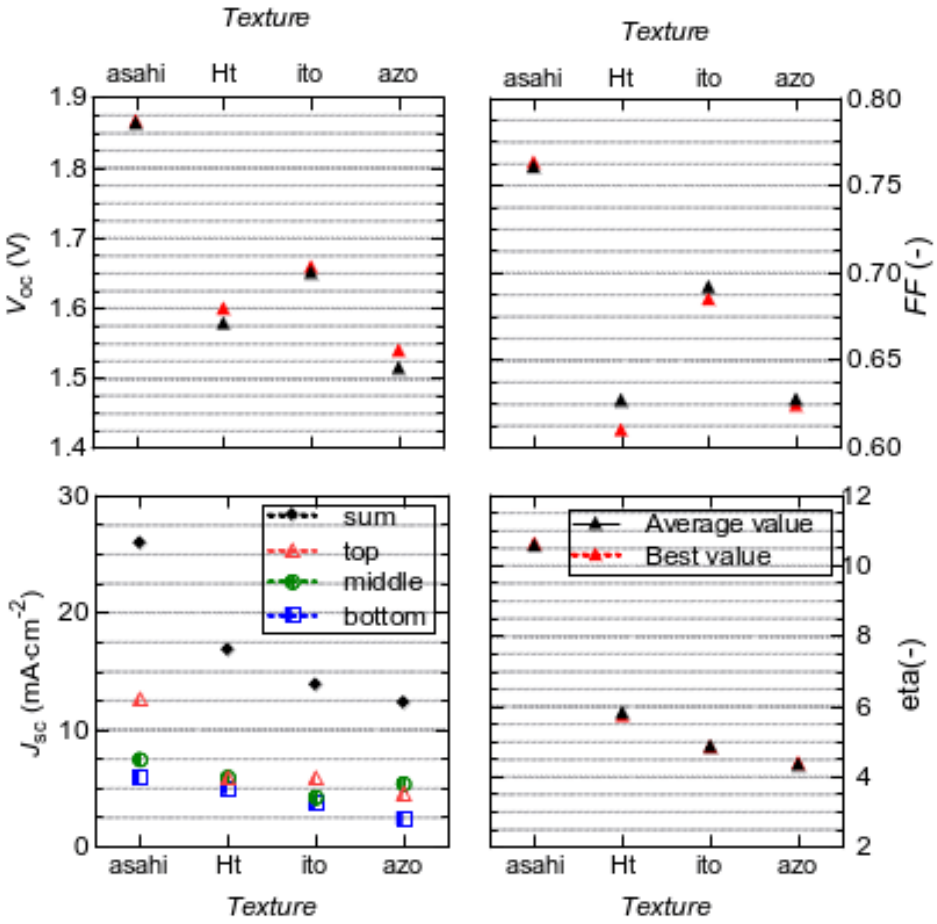

Figure 7.4: The variation in performance of the triple junction solar cell(a-Si/nc-Si/nc-Si) with Asahi, Hairen tan(Ht), ITO etched and AZO etched on glass textures in p-i-n configuration

Solar cell on Asahi substrate have great V_{oc} and FF of 1.86V and 76% respectively. The current density in the top, bottom and middle junctions are 12.59mA/cm^2, 5.8mA/cm^2 and 7.46mA/cm^2. A proper distribution of light between the middle and bottom cell needs be done so that the overlap in the production of current under the same wavelength is minimized. This will be seen in the next section where the n-doped silicon oxide layer is used as a intermediate reflector.

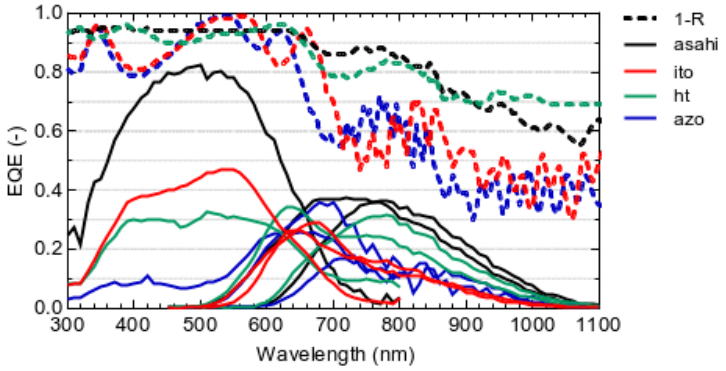

Figure 7.5: Comparing the EQE of a-Si/nc-Si/nc-Si solar cells on Asahi, HT, AZO and ITO textured substrates.

7.3.3. n-i-p tandem devices

Figure 7.6 shows that the best efficiency for a micromorph in n-i-p configuration is obtained in the smooth pyramidal textured substrate of 10.92% and 10.63% for S5 and S11. For the solar cells with $1.5\mu m$ thick bottom cell have higher *FF* than the solar cells with $2.5\mu m$ thick bottom cell. Thus, there is higher efficiencies for $2.5\mu m$ thick nc-Si solar cells. The main take away is that the nc-Si with thicknesses $1.5\mu m$ and $2.5m$ for a tandem device can be grown crack free on smooth pyramidal textured substrate. A thick bottom cell can be grown in S11 without much loss in the *FF* and V_{oc} and has a good optical property for a micromorph tandem solar cell.
Good contenders to the smooth pyramid texture are the large period honeycomb texture which was etched for 16mins(H16L) with $1.5\mu m$ nc-Si absorber layer thickness and ITO texture with $2.5\mu m$ nc-Si absorber layer thickness. They obtained a maximum efficiency of 9.7% for honeycomb texture and 10.64% for the ITO texture. The honeycomb textured solar cell samples have low *FF* compared to the high performing smooth pyramidal and ITO textured samples. This is due to the low shunt resistances of the honeycomb textured samples. The shunt resistance of the honeycomb textured samples were lower than $10k\Omega.cm^2$ whereas the other high performing textured samples had shunt resistances above $15k\Omega cm^2$. This low shunt resistance and *FF* can be attributed to the recombination losses due to development of cracks during the growth of nc-Si. In Table 7.1, the R_{rms} of the H12L texture is given as 270nm, which is greater than the roughness of all smooth pyramidal, ITO and AZO textures. Honeycomb texture of 16 minutes etching time is predicted to have higher roughness than H12L. This is due to increase in depth of the craters with etching time. Hence, a roughness of more than 270nm can lead to poor quality of nc-Si growth. However, the low shunt resistance may not be due to the feature size. It can also be unique to the honeycomb texture, the bottom cell absorber layer might have exceeded the threshold thickness and could have led to cracks.
The higher *FF* of $1.5\mu m$ thick bottom junction solar cells than the solar cells with $2.5\mu m$ thick bottom junction solar cells in Figure 7.6 can be explained by the increase in series resistance due to the increase in thickness of the absorber layer. The J_{sc} of the bottom cell increases from $9.9mA/cm^2$ to $12.1mA/cm^2$ with increase in i-nc-Si thickness for S11 textured solar cell. Therefore, it can also be because of fill factor compensation as explained in subsection 7.3.1.

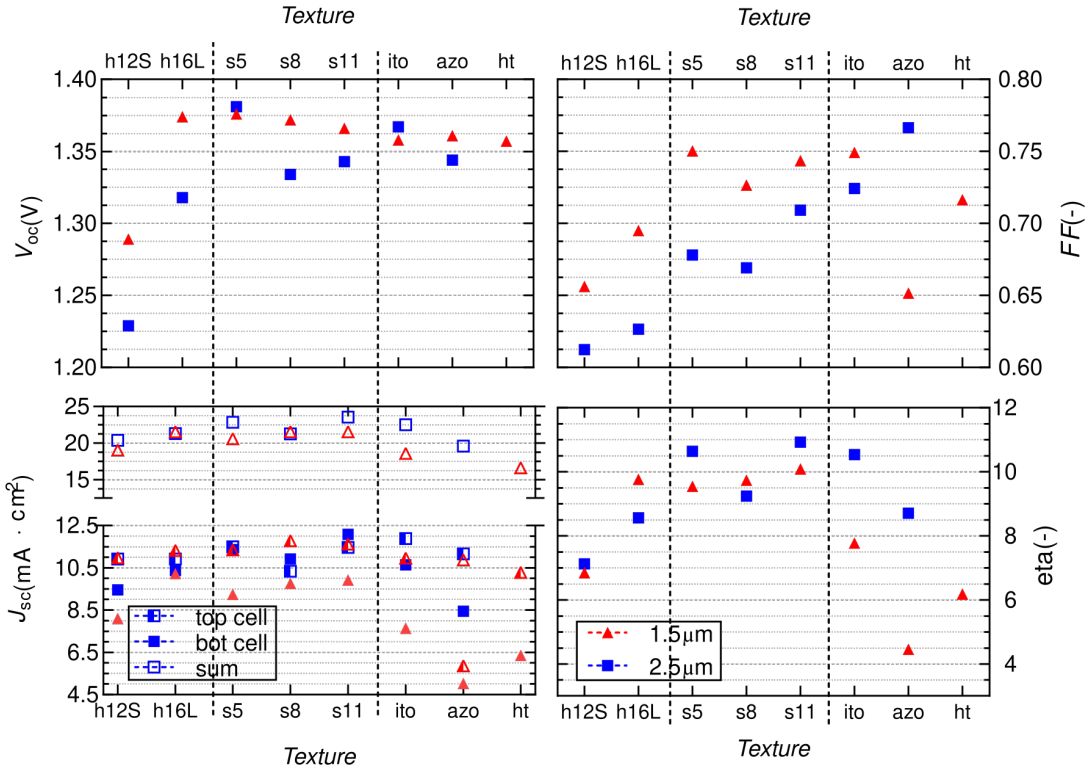

Figure 7.6: The variation in performance of the micromorph solar cell with honeycomb of small period with 12 minutes etched(h12S), honeycomb of large period with 16 minutes etched(h16L), smooth pyramidal with ecthing time of 5(S5), 8(S8) and 11(S11), Hairen tan(Ht), ITO etched and AZO etched on glass textures in n-i-p configuration for bottom cell thickness of 1.5μm and 2.5μm

In Figure 7.7, from the EQE, it can be clearly seen that the large period honeycombs textures have better response in the longer wavelengths (650nm-1100nm). Hence, small period honeycomb textures is not a proper candidate for thin-film silicon deposition.

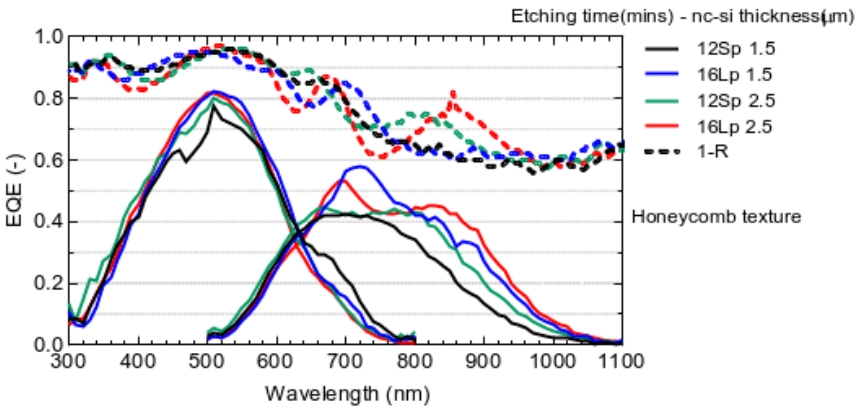

Figure 7.7: Comparing the EQE of micromorph solar cells on honeycomb textured substrates with small period etched for 12mins and large period etched for 16mins for i-nc-Si thicknesses of 1.5μm and 2.5μm

In Figure 7.8, there can be seen a shift in the spectral response of top cell with change in the type of

texture. The difference between J_{sc} of the top cell for different texture is not significant. The solar cell with smooth pyramidal texture with 2.5μm thick i-nc-Si has the highest spectral response in the wavelengths 750nm to 1100nm.

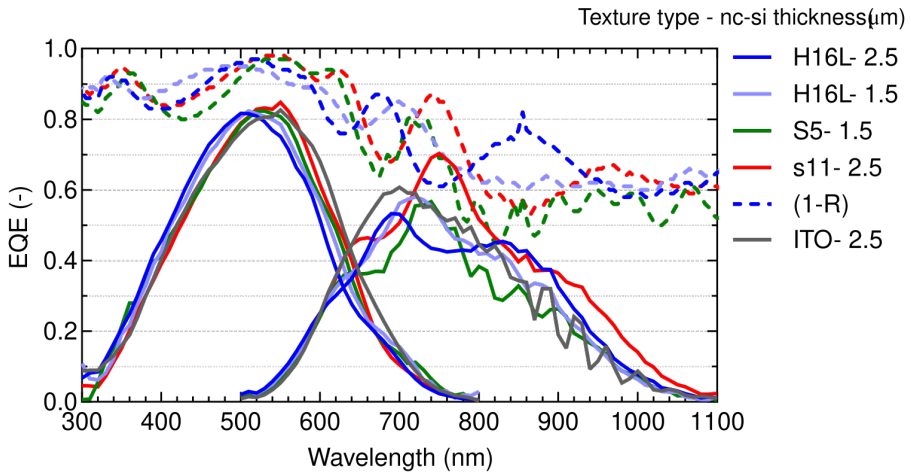

Figure 7.8: Comparing the EQE of micromorph solar cells on honeycomb(H16L), smooth pyramidal(S5,S11) and ITO textured substrates for i-nc-Si thicknesses of 1.5μm and 2.5μm

7.3.4. n-i-p triple junction devices

The smooth pyramidal texture gives the highest conversion efficiency for triple junction n-i-p. This can be seen in Figure 7.9. The honeycomb texture for triple junction has significantly low efficiency compared to the smooth pyramidal texture. This is because of the *FF* and V_{oc} of honeycomb textured solar cell is significantly low. This can be due to the same reasons mentioned in subsection 7.3.3.

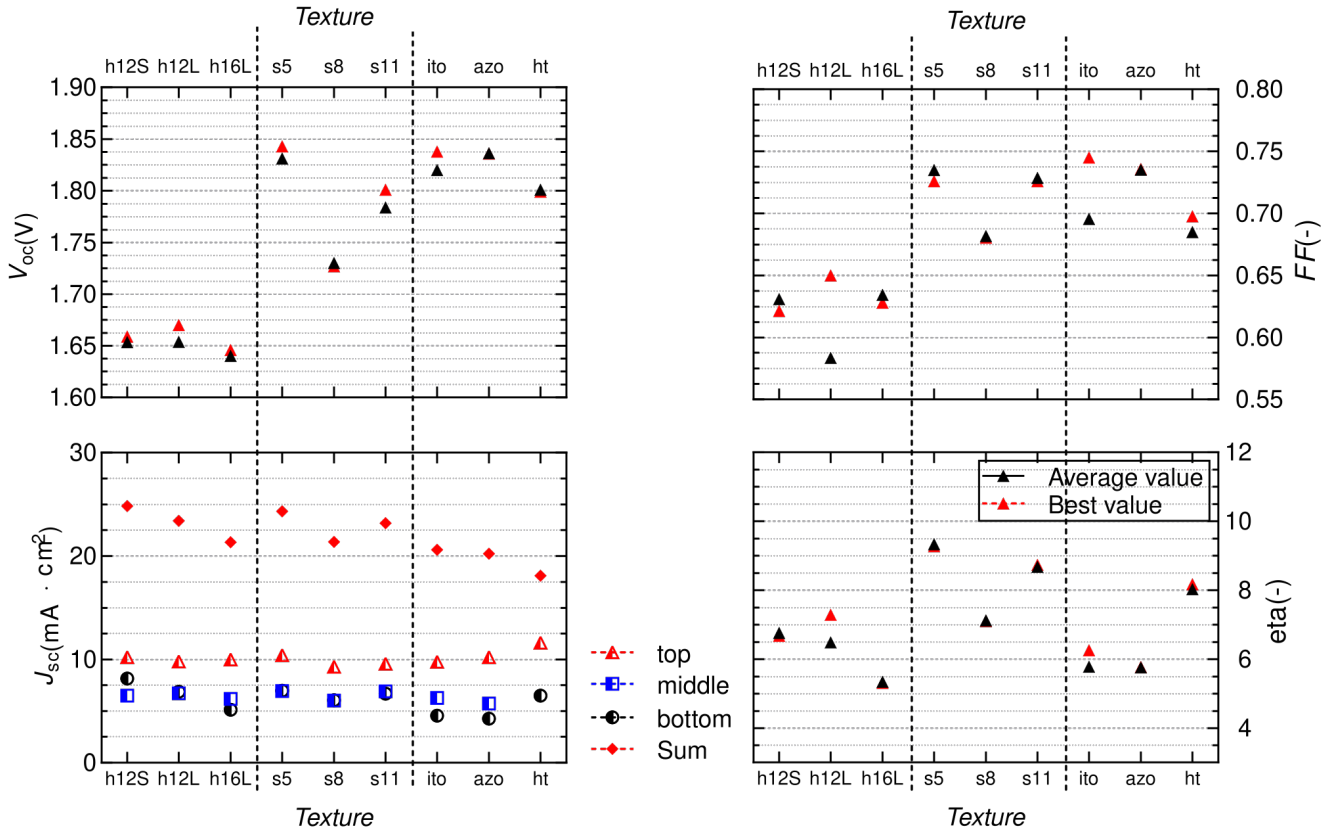

Figure 7.9: The variation in photovoltaic performance of the a-Si/nc-Si/nc-Si triple junction solar cell with honeycomb of small period with 12 minutes etched(h12S), honeycomb of large period with 16 minutes etched(h16L), smooth pyramidal with ecthing time of 5(S5), 8(S8) and 11(S11), Hairen tan textured glass(Ht), ITO etched and AZO etched on glass textures in n-i-p configuration

Overall, In the n-i-p configuration H16L and H12S textures leads to cells with low shunt resistance. Hence, a roughness greater than 270nm is not preferred as it results in shunted cells. The smooth pyramidal textures with R_{rms} from 160 to 230nm had the best performing cells in the n-i-p configuration in both tandem and triple junctions. The solar cells with smooth pyramidal textures in n-i-p configuration has the best spectral response in the infrared region. The Asahi texture with R_{rms}= 42nm had the best performance in the p-i-n configuration. The conversion efficiency of the best performing cells for tandem micromorphs in n-i-p and p-i-n configurations were 10.92% and 11.48% respectively. Further, with increase in i-nc-Si layer thickness there is a significant increase in the J_{sc} of the bottom cell.

8

Silicon oxide intermediate reflector

8.1. Introduction to silicon oxide intermidiate reflector

This section investigates the intermediate reflective layer(IRL) in micromorph solar cells. This study is done to distribute the light that enters the solar cell between the subcells. The research on IRL will help us divide the current and increase the current of the limiting junction. The intermediate reflector is used to reflect the light that is left unabsorbed by the top cell. This is required, as the top cell, the high band gap a-Si is thin in order to minimize the light induced degradation due to steabler wronski effect to achieve high *FF* and V_{oc} [48]. For a material to act as an intermediate reflector the refractive index of the reflector should be lower than the refractive index of silicon [43]. The aim is to maximize reflection at the Si-SiO_x interface. In this study the n-doped nc-Siox:H layer in the tandem recombination junction will play the role of the IRL. The n-SiO_x is chosen because there is a larger processing window for obtaining good quality n-SiO_x than for p-SiO_x [62].
The change in optical and electrical performance of the micromorph solar cell with variation in CO_2 flow rate and thickness of the SOIR layer is studied.

8.2. Results of SOIR study

8.2.1. Micromorphs with honeycomb texture

In Figure 8.1, it can be seen that the high V_{oc} of 1.348V and 1.351V are obtained for the 90nm thick n-SiOx layer. There can also be noticed that the optimum V_{oc} shifts to the higher CO_2 flow rates with the increase in thickness. The optimum V_{oc} point of the 30nm thick n doped layer might be at a CO_2 flow rate below 1.4sccm as per the observed trend. The *FF* shows decreasing trend for the 30nm thick SOIR layer because the top junction is the current limiting junction throughout the whole range of CO_2 flow rate. If the J_{sc} is limited by the bottom cell there can be observed a boost in the *FF*. The solar cell with 90nm thick with F_{CO2}=3.2sccm n-SiOx has a high V_{oc}*FF of 0.97. It has a high electrical performance compared to the solar cells with lower n-SiOx thicknesses.
90nm thick n-SiOx is comparatively thicker than the 30nm and 60nm n-SiOx layer. A thicker layer in the tandem recombination junction will most probably result in a low V_{oc} due to the increase in the series resistance for charge carrier to transport in thicker layers. However there could also be other reasons that can play role in determining the V_{oc}. The material properties of the n-SiOx might have changed or the energy barrier might of have decreased due to better band alignment which can overcompensate the effect of increase in resistance, and this can lead to an higher V_{oc}.

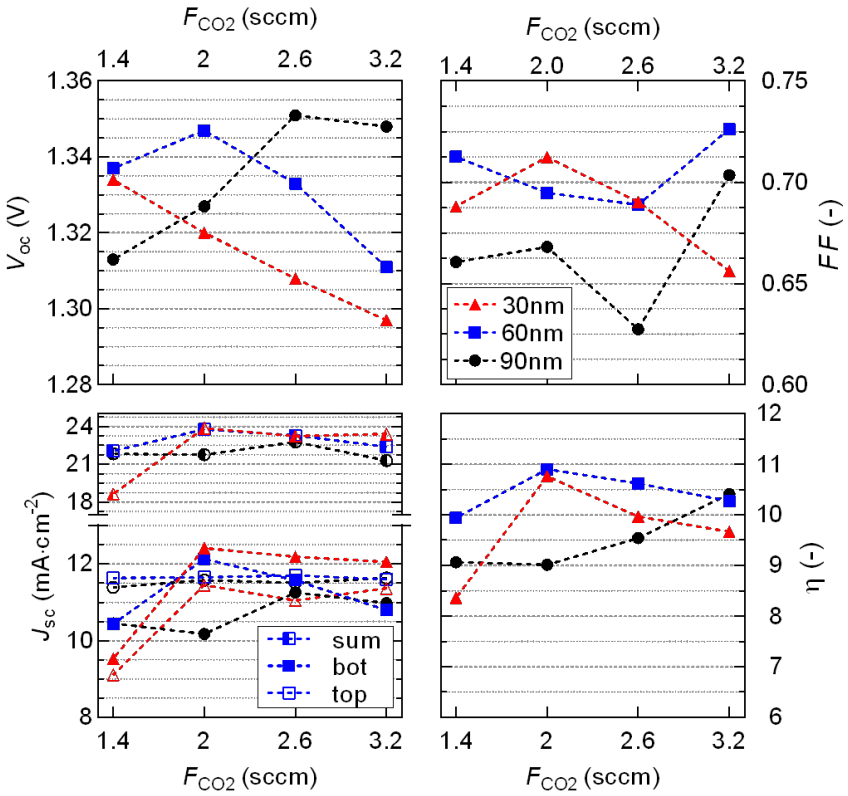

Figure 8.1: The variation in photovoltaic performance of the micromorph solar cell on honeycomb textured substrate with CO_2 flow rates of n-SiOx layer of the top cell. Thicknesses of the SOIR layer are 90,30 and 60nm. F_{CO2} is the CO_2 flow rate of the SOIR layer

Figure 8.2 shows with increase in the thickness of the SOIR there is a decrease in the EQE and the absorptance in the wavelength range 850nm-1000nm. So, this can confirm the reflective property of the layer. However, the reflection does not happen near 600nm wavelength, where the top and bottom cell EQE intersect. Due to this the reflected light cannot be absorbed by the top cell as the absorption of photon of the top cell ends at a wavelength of 800nm. This led to a loss in absorption by reflection of light. Hence, this SOIR cannot current match the tandem device but it can be used on a a-Si/nc-Si/nc-Si triple junction device to divide the current between the bottom and middle cell. The EQE intersection area of the middle and bottom junction share the same wavelength with where the light is being reflected, so current can be divided. This also shows that the refractive index of the n-SiOx layer has a strong spectral dependence and has a low refractive index in the wavelength in which it is reflecting light.

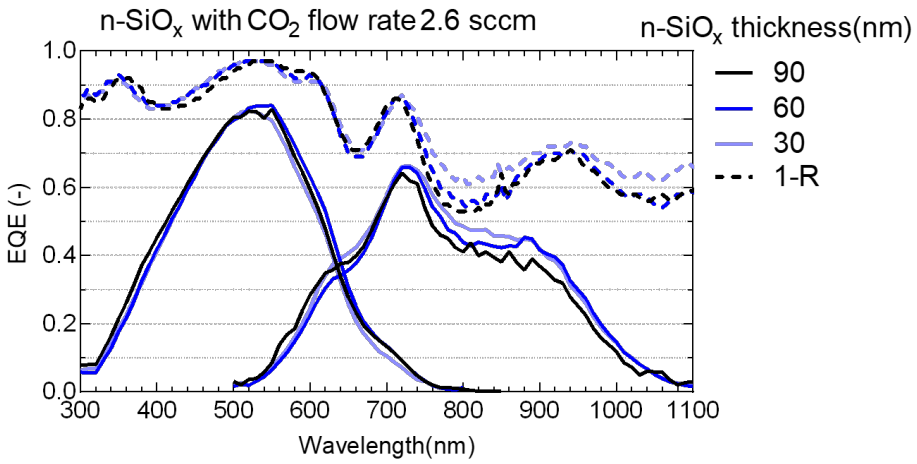

Figure 8.2: Comparing the EQEs of micromph solar cell on honeycomb texture having 90nm,60nm and 30nm thick SOIR layer with constant CO_2 flow rate of 2.6sccm

A 90nm thick SOIR with CO_2 flow rate of 2 to 2.6 can be used for a triple junction solar in order to get good V_{oc} and good reflection property. The SOIR should be between the middle and the bottom junction.

8.2.2. Micromorph with smoothened pyramidal texture

For the smoothened pyramidal textured substrate, the V_{oc} lower for the samples with the SOIR layers thicknesses 30nm and 90nm with increase in CO_2 flow rate. This can be seen in the Figure 8.3. It can be also noticed that the *FF* is not sensitive to the change in CO_2 flow rate of the n-SiOx layer. High FF^*V_{oc}=0.971 is obtained for the sample with 90nm thick SOIR and F_{CO2} of 3.2sccm.

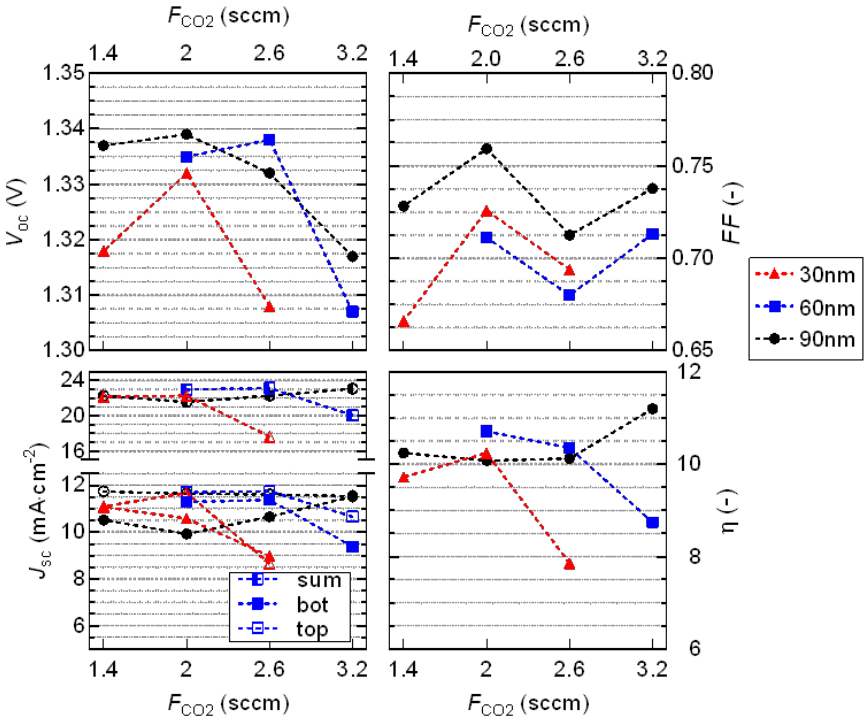

Figure 8.3: The variation in photovoltaic performance of the micromorph solar cell on smooth pyramidal textured substrate with CO_2 flow rates of n-SiOx layer of the top cell. Thicknesses of the SOIR layer are 90,30 and 60nm. F_{CO2} is the CO_2 flow rate of the SOIR layer

In the Figure 8.4, it can be seen that the thickest n-SiOx layer has the lowest bottom cell EQE. This might be because of the increase in reflection in the infrared region. The absorptance curve from the wavelengths 850nm to 1050nm, shows the decrease in absorption with increase in thickness. However, the difference in the EQE curve of the 30nm and the 60nm is not significant in the same wavelength range. If parasitic absorption is the reason for the loss in EQE in 30nm thick SOIR samples, the loss should be higher in the thicker SOIR samples. This means there is some electrical loss for the 30nm thick SOIR solar cell. The J_{sc} values indicate that the 60nm is more than the 30nm SOIR layer with CO2 flow rate of 2sccm. So, it could be said that the reflective property of the n-SiOx is not translated to J_{sc} due to the change in the material of the recombination junction.

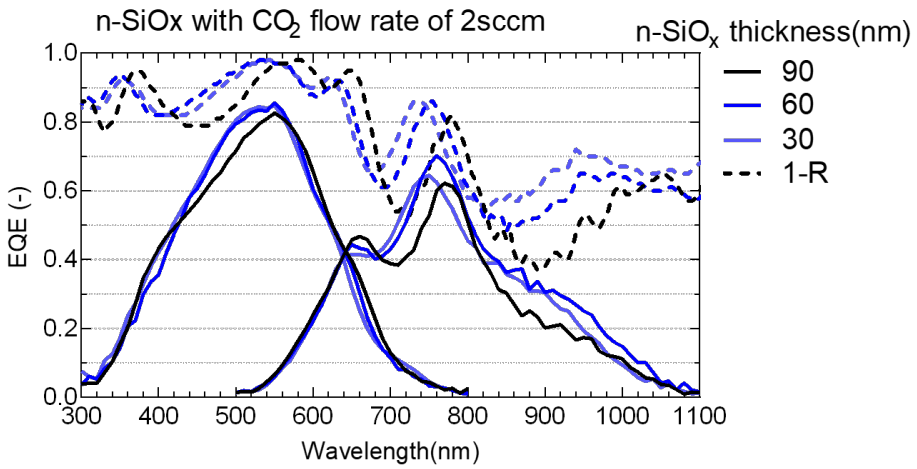

Figure 8.4: Comparing the EQEs of micromph solar cell on honeycomb texture having 90nm,60nm and 30nm thick SOIR layer with constant CO_2 flow rate of 2.6sccm

It can been seen that in both Figure 8.3 and Figure 8.1 the best performance is obtained by the solar cell with 90nm thick SOIR and with high F_{CO2} of 3.2sccm. This means the 90nm thick SOIR shows good reflective property and also a high Voc*FF of 0.94 and 0.92 is obtained for smooth pyramidal and honeycomb texture respectively with high F_{CO2}. Additionally, for 30nm and 60nm thick SOIR solar cell, the performance reduces when F_{CO2} is greater than 2sccm. This is true for the solar cells in both honeycomb texture and smooth pyramidal.
In summary, the current can be distributed between the middle and bottom junction for an a-Si/nc-Si/nc-Si solar cell with increase in thickness of the SOIR . There was no clear trend seen in EQE with change in F_{CO2}. Further, The thickest SOIR layer also gives the highest V_{oc}*FF. A thick 90nm n-SiO_x with a F_{CO2} of 3.2sccm has the best V_{oc}*FF of 0.94. Hence a thick n-SiO_x layer with high F_{CO2} of 3.2sccm is preferred for good electrical property and for distribution of current. For a thinner n-SiO_x layer increase in F_{CO2} reduces the performance of the solar cell.

9

Conclusions and Outlooks

9.1. Conclusions

This section will summarize the conclusions drawn from the results discussed in the previous section.
We have seen that to get a good EQE measurement of a micromorph device, an increase in bias light intensity and with a decrease in probe light intensity is required. The main problem was found to be that the non-targeted cell had low response in its particular wavelengths of absorption as the bias light does not bias non-targeted cell properly. To maintain a standard for the EQE measurement of micromorph devices, bias lights 1-3 should be used to bias the top junction and bias lights 7-8 should be used to bias the bottom junction combined with a 50% reduction in the probe light intensity. Further, it was found that a forward voltage bias that is slightly less than the V_{oc} of the non-targeted cell should be applied to measure the targeted cell in short circuit conditions.

The p-layer was studied on a-Si single junctions. In this study it was concluded that both the contact layer and the window layer of the p-layer have a high influence on the electrical and optical properties of the solar cell. A conversion efficiency of 10% and V_{oc} of 910mV were achieved for the a-Si single junction solar cells. Further, it was also found that there is more than one way to reach high efficiency with an optimal p-layer by changing the diborane, CO_2 flow rate, and thickness of both the contact and window layer. It was also found that p-SiOx$^+$ contact layer results in good performing solar cells for a larger range of F_{B2H6} in the window layer than p-nc-Si contact layer and the insertion of the buffer layer in the i/p interface showed no significant improvement in the performance of the solar.

By comparing the different textures it was found out that the best performance was obtained from asahi textured glass in p-i-n configuration in both double and triple junction solar cell. However, the low performance of the Ht, ITO and AZO textures might be because of the unoptimized TCO or damage caused during the measurement due to the probes. In n-i-p configuration smooth pyramidal textured solar cells had the best optical and electrical performance in both double and triple junction. Further, the honeycomb textured substrate with R_{rms} around 270nm is not suitable to deposit double and triple junction solar cell as it resulted in solar cells with low shunt resistance.

The SOIR that was used can be used in the a-Si/nc-Si/nc-Si triple junction solar cell to divide current within the middle and bottom junctions. The reflection of light increases in the infrared region with the increase in the thickness of the n-SiOx layer. A thick(90nm) n-SiOx layer with high F_{B2H6}(3.2sccm) gives the best electrical performance and current distribution property for a solar cell.

9.2. Future Outlooks

There is more room for further optimization of the thin-film silicon solar cell to achieve higher efficiency.

The quality of i-nc-Si can be optimized to increase the absorption of light in red and infrared wavelength range. The crystallinity of i-nc-Si of can be focused to find the the best deposition conditions to obtain a certain cyrstallinity which results in ideal optical and electrical performance for the solar cell.

The TCO material can be optimised so that it has high mobility of charge carriers, low sheet resistance and low drude absorption. The decrease in drude absorption will allow more red light to be absorbed by the solar cell. This can increase the electrical and optical performance by a significant amount.

The FF compensation can be studied in the future, to characterize the influence of the mismatch in J_{sc} on the *FF* in a multi-junction cell. This study can find the optimum between the increase in FF and decrease in J_{sc} of the current limiting cell.

Appendices

A

Experimental values

Table A.1: solar cell performance of single junction a-Si with different thicknesses(nm), material and flow rate of CO2 and B2H6 (sccm) of contact layer, window layer and buffer layer. The p-SiOx conditions is the conditions of the window layer of the p-layer

dcontact (nm)	dwindow (nm)	dbuffer (nm)	contact / seed	psiox conditions(sccm)	Jsc (mA/cm^2)	Voc (V)	FF	Eta(%)	Rs	Rsh
3	12	9	p-nc-Si / i-SiOx	10-2.2 B2h6 - CO2	14.50	0.76	0.51	5.66	10.54	3844.92
3	12	6	p-nc-Si / i-SiOx	10-2.2 B2h6 - CO2	14.04	0.88	0.60	7.37	8.91	6075.95
3	12	0	p-nc-Si / -	10-2.2 B2h6 - CO2	14.06	0.85	0.70	8.39	6.55	6182.38
3	12	9	p-nc-Si / i-nc-Si	10-2.2 B2h6 - CO2	11.31	0.71	0.64	5.18	11.03	3026.48
3	8	3	p-SiOx / i-SiOx	10-2.2 B2h6 - CO2	15.55	0.80	0.57	7.13	16.62	4940.49
3	8	3	p-SiOx / i-SiOx	30.2.2 B2h6 - CO2	15.64	0.88	0.66	9.04	15.30	5171.60
3	12	3	p-SiOx / i-SiOx	30.2.2 B2h6 - CO2	15.04	0.88	0.70	9.26	12.46	6892.23
6	8	3	p-SiOx / i-SiOx	30.2.2 B2h6 - CO2	14.81	0.88	0.72	9.40	11.24	6913.89
6	12	3	p-SiOx / i-SiOx	30.2.2 B2h6 - CO2	14.15	0.89	0.72	9.05	11.56	6334.58
6	8	3	p-nc-Si / i-SiOx	10-2.2 B2h6 - CO2	14.81	0.86	0.70	8.93	11.71	6713.46
6	8	3	p-nc-Si / i-SiOx	30.2.2 B2h6 - CO2	15.36	0.89	0.70	9.54	10.09	6622.52
6	12	3	p-nc-Si / i-SiOx	30.2.2 B2h6 - CO2	14.99	0.90	0.73	9.88	12.21	7335.78
9	12	3	p-SiOx / i-SiOx	10-2.2 B2h6 - CO2	13.86	0.89	0.73	8.97	13.27	7087.63
6	12	3	p-SiOx / i-SiOx	10-2.2 B2h6 - CO2	15.04	0.90	0.74	10.01	11.02	8070.43
3	12	3	p-SiOx / i-SiOx	10-2.2 B2h6 - CO2	14.70	0.89	0.72	9.38	10.78	8422.66
0	12	3	- / i-SiOx	10-2.2 B2h6 - CO2	13.32	0.88	0.68	7.93	14.48	7829.18
9	12	3	p-nc-Si / i-SiOx	10-2.2 B2h6 - CO2	14.26	0.91	0.72	9.33	12.88	6141.82
6	12	3	p-nc-Si / i-SiOx	10-2.2 B2h6 - CO2	15.83	0.83	0.57	7.50	20.40	4066.54
3	12	3	p-nc-Si / i-SiOx	10-2.2 B2h6 - CO2	15.58	0.82	0.61	7.86	16.92	4087.70
3	12	3	p-nc-Si / i-SiOx	10-1.2 B2h6 - CO2	14.62	0.86	0.63	7.93	52.47	8613.94
3	8	3	p-nc-Si / i-SiOx	10-1.2 B2h6 - CO2	15.48	0.82	0.70	8.88	11.91	5629.84
3	8	3	p-nc-Si / i-SiOx	10-2.2 B2h6 - CO2	15.94	0.82	0.65	8.47	11.86	6493.51
3	8	3	p-nc-Si / i-SiOx	30-1.2 B2h6 - CO2	13.91	0.89	0.72	8.92	14.16	12618.30
3	8	3	p-nc-Si / i-SiOx	30-2.2 B2h6 - CO2	15.50	0.90	0.71	9.90	11.00	9378.66
3	8	3	p-nc-Si / i-SiOx	30-3.2 B2h6 - CO2	14.98	0.92	0.68	9.36	19.20	10403.12
3	16	3	p-nc-Si / i-SiOx	10-1.2 B2h6 - CO2	14.28	0.85	0.68	8.26	17.52	5629.84
3	16	3	p-nc-Si / i-SiOx	10-2.2 B2h6 - CO2	15.73	0.89	0.66	9.23	16.45	5298.01
3	16	3	p-nc-Si / i-SiOx	10-3.2 B2h6 - CO2	15.86	0.90	0.51	7.26	62.71	3033.75
3	16	3	p-nc-Si / i-SiOx	30-1.2 B2h6 - CO2	11.66	0.90	0.73	7.63	15.01	8359.46
3	16	3	p-nc-Si / i-SiOx	30-2.2 B2h6 - CO2	15.04	0.89	0.72	9.67	12.76	6779.66

Table A.2: shows the values of performance of tandem and triple junction of the solar cell in n-i-p configuration with the textures AZO, ITO, HT, Honeycomb with large period etched for 16min and small period etched for 12mins and smooth pyramidal etched for 5, 8 and 11 mins. The a-si absorber layer thickness is given in 'nm',the i-nc-Si thickness is given in 'μm', the Jsc is given in 'mA/cm^2' and the Rs is the series resitance and Rsh is the shunt resistance and is given in $\Omega.cm^2$

Textures	**i-a-si thickness**	**i-ncSi thickness**	**i-ncSi thickness**	**Jsc_top**	**Jsc _mid**	**Jsc _bot**	**Voc (V)**	**FF**	**Efficiency (%)**	**Rs**	**Rsh**
AZO	230.00	1.50		5.86		5.02	1.36	0.65	4.45	13.82	8120.65
ITO	230.00	1.50		10.96		7.64	1.36	0.75	7.77	11.36	16581.13
HT	230.00	1.50		10.28		6.35	1.36	0.72	6.18	7.58	12490.24
AZO	200.00	2.50		11.16		8.46	1.34	0.77	8.71	4.62	25719.53
ITO	230.00	2.50		11.89		10.65	1.37	0.72	10.54	7.01	15509.60
honey L16	230.00	1.50		11.33		10.23	1.37	0.70	9.77	11.39	11093.50
Honey S12	230.00	1.50		10.98		8.10	1.29	0.66	6.85	15.19	8376.55
smooth 5	230.00	1.50		11.35		9.25	1.38	0.75	9.55	8.34	23555.80
smooth 8	230.00	1.50		11.78		9.77	1.37	0.73	9.73	10.29	22913.26
smooth11	230.00	1.50		11.62		9.93	1.37	0.74	10.08	7.16	23307.44
honey L16	230.00	2.50		10.92		10.37	1.32	0.63	8.57	16.45	6351.13
Honey S12	230.00	2.50		10.92		9.46	1.23	0.61	7.12	15.19	5933.04
smooth 5	230.00	2.50		11.50		11.36	1.38	0.68	10.64	12.19	10619.47
smooth 8	200.00	2.50		10.35		10.91	1.33	0.67	9.24	13.93	17743.98
smooth11	200.00	2.50		11.47		12.09	1.34	0.71	10.92	7.91	9194.40
AZO	200.00	1.50	2.20	10.22	5.74	4.27	1.84	0.74	5.77	68.04	18461.54
ITO	200.00	1.50	2.20	9.78	6.27	4.57	1.84	0.75	6.26	42.04	21063.19
HT	200.00	1.50	2.20	11.60		6.51	1.80	0.70		88.58	19626.17
honey L16	200.00	1.50	2.20	10.01	6.19	5.14	1.65	0.63	5.31	27.28	14568.16
Honey S12	200.00	1.50	2.20	10.20	6.48	8.16	1.66	0.62	6.68	41.58	10838.71
smooth 5	200.00	1.50	2.20	10.40	6.94	6.98	1.84	0.73	9.28	71.49	27888.45
smooth 8	200.00	1.50	2.20	9.29	6.04	6.06	1.73	0.68	7.10	45.97	13337.57
smooth11	200.00	1.50	2.20	9.60	6.90	6.68	1.80	0.73	8.73	65.60	21852.24

Table A.3: shows the values of performance of tandem and triple junction the solar cell in p-i-n configuration with the textures AZO, ITO, HT, and asshi glass. The a-si absorber layer thickness is given in 'nm',the i-nc-Si thickness is given in 'μm', the Jsc is given in 'mA/cm^2' and the Rs is the series resitance and Rsh is the shunt resistance and is given in $\Omega.cm^2$

Textures	**a-si absorber**	**ncSi absorber**	**ncSi absorber**	**Jsc_top**	**Jsc _mid**	**Jsc _bot**	**Voc (V)**	**FF**	**Efficiency (%)**	**Rs**	**Rsh**
asahi	230.00	1.50		12.48		9.45	1.39	0.74	9.80	11.22	11134.68
AZO	230.00	1.50		5.54		2.93	1.44	0.51	2.16	164.58	18424.28
ITO	230.00	1.50		9.82		5.18	1.42	0.55	4.03	72.40	9748.17
HT	230.00	1.50		7.20		3.94	1.41	0.49	2.72	110.00	20593.28
asahi	200.00	2.50		12.58		11.74	1.38	0.71	11.48	10.28	10695.19
AZO	200.00	2.50		6.90		5.74	0.90	0.56	2.88	60.57	18083.96
ITO	230.00	2.50		6.43		6.35	0.88	0.52	2.91	52.68	11140.58
HT	230.00	2.50		7.81		6.87	1.04	0.51	3.63	74.78	14117.65
asahi	200.00	1.50	2.20	12.60	7.46	5.88	1.87	0.76	8.38	59.59	32233.31
AZO	200.00	1.50	2.20	4.57	5.39	2.37	1.54	0.62	2.27	149.14	31578.95
ITO	200.00	1.50	2.20	5.85	4.26	3.72	1.66	0.69	4.23	182.84	42075.74
HT	200.00	1.50	2.20	5.87	5.92	5.02	1.60	0.61	4.89	162.17	31049.01

Table A.4: Photovoltaic performance of micromorph with honeycomb texture. a-Si, nc-Si absorber layer and n-SiOx thickness are given in nm, F_{CO2} is given sccm, Jsc is given in mA/cm^2, Voc is given V, Rs and Rsh are the series and shunt resistance of the cell given in $\Omega.cm^2$

a-Si absorber	**nc-Si absorber**	**n-SiOx** F_{CO2}	**n-SiOx thickness**	**Jsc_top**	**Jsc _bottom**	**Voc**	**FF**	**Rs**	**Rsh**	**efficiency**
280.00	2.50	3.20	90.00	10.24	11.04	1.35	0.70	23.36	13392.86	9.71
280.00	2.50	2.60	90.00	11.50	11.26	1.35	0.63	18.25	6708.19	9.54
280.00	2.50	2.00	90.00	9.39	10.17	1.33	0.67	40.92	10869.57	8.32
280.00	2.50	1.40	90.00	11.38	10.45	1.31	0.66	10.76	10201.60	9.07
280.00	2.50	3.20	60.00	9.41	10.79	1.31	0.73	21.58	22471.91	8.96
280.00	2.50	2.60	60.00	9.92	11.57	1.33	0.69	7.89	9838.37	9.11
280.00	2.50	2.00	60.00	11.65	12.12	1.35	0.69	6.45	14324.69	10.90
280.00	2.50	1.40	60.00	11.59	10.11	1.34	0.71	4.45	17661.90	9.63
280.00	2.50	3.20	30.00	11.36	12.05	1.30	0.66	9.42	7984.79	9.67
280.00	2.50	2.60	30.00	11.04	12.18	1.31	0.69	6.61	12571.09	9.97
280.00	2.50	2.00	30.00	11.28	8.82	1.32	0.71	12.79	9397.02	8.30
280.00	2.50	1.40	30.00	8.52	7.01	1.33	0.69	6.49	12280.70	6.44

Table A.5: photovoltaic performance of micromorph with smooth pyramidal texture. a-Si, nc-Si and n-SiOx absorber thickness are given in nm, F_{CO2} is given sccm, Jsc is given in mA/cm^2, Voc is given V, Rs and Rsh are the series and shunt resistance of the cell given in $\Omega.cm^2$

a-Si absorber	**nc-Si absorber**	**nsiox co2**	**nsiox thickness**	**Jsc_top**	**Jsc _bottom**	**Voc**	**FF**	**Rs**	**Rsh**	**efficiency**
280.00	2.50	3.20	90.00	9.86	11.53	1.32	0.74	19.52	28301.89	9.58
280.00	2.50	2.60	90.00	9.16	10.83	1.33	0.71	23.00	15267.18	8.69
280.00	2.50	2.00	90.00	9.48	9.92	1.34	0.76	22.32	30612.24	9.64
280.00	2.50	1.40	90.00	9.63	10.52	1.34	0.73	8.94	18534.86	9.37
280.00	2.50	3.20	60.00	9.31	11.07	1.31	0.71	5.29	13422.82	8.68
280.00	2.50	2.60	60.00	11.75	11.38	1.34	0.68	10.51	14893.62	10.35
280.00	2.50	2.00	60.00	11.70	11.28	1.34	0.71	7.23	23255.81	10.71
280.00	2.50	1.40	60.00	5.71	3.82	1.65	0.50	51.31	9705.82	3.13
280.00	2.50	3.20	30.00	11.57	12.17	1.33	0.71	5.15	17979.45	10.94
280.00	2.50	2.60	30.00	8.65	8.97	1.31	0.69	5.44	10429.60	7.85
280.00	2.50	2.00	30.00	9.62	11.50	1.33	0.73	18.39	24896.27	9.30
280.00	**2.50**	1.40	30.00	11.10	7.87	1.32	0.67	11.93	11884.55	6.91

Table A.6: The total p layer thickness is 16nm,i-a-Si thickness is 280nm and the contact layer p-$SiOx^+$. The contact layer and window layer thickness are given in 'nm',the contact layer diborane flow rate and window layer diborane flow rate are givein in 'sccm', the Voc is given in volts, the Jsc is given in 'mA/cm^2' and the Rs is the series resitance and Rsh is the shunt resistance and is given in $\Omega.cm^2$

dcontact	dwindow	Contact p-siox diborane flow rate	Window psiox diborane flow rate	Jsc	Voc	FF	Efficiency	Rs	Rsh
6.00	10.00	20.00	10.00	150.11	0.87	0.69	8.96	19.48	4165.74
6.00	10.00	35.00	10.00	147.15	0.86	0.68	8.64	13.25	3599.83
6.00	10.00	50.00	10.00	152.06	0.87	0.70	9.26	15.62	3828.16
6.00	10.00	65.00	10.00	126.42	0.89	0.72	8.05	16.46	6501.62
6.00	10.00	80.00	10.00	154.19	0.88	0.62	8.38	25.21	2123.55
6.00	10.00	40.00	30.00	150.76	0.87	0.65	8.53	11.20	2155.62
6.00	10.00	60.00	30.00	150.41	0.88	0.69	9.17	11.86	3971.01
6.00	10.00	80.00	30.00	151.96	0.88	0.67	8.97	16.39	3224.23
3.00	13.00	20.00	10.00	162.17	0.84	0.68	9.24	9.16	2488.43
3.00	13.00	50.00	10.00	154.97	0.86	0.68	9.00	16.17	3413.00
3.00	13.00	80.00	10.00	156.13	0.88	0.67	9.25	20.61	5039.44
3.00	13.00	40.00	30.00	129.57	0.89	0.59	6.86	41.86	3099.34
3.00	13.00	60.00	30.00	144.86	0.90	0.61	8.01	39.44	3968.08
3.00	13.00	80.00	30.00	136.32	0.89	0.60	7.21	29.16	2224.92
8.00	8.00	35.00	10.00	132.76	0.86	0.56	6.42	25.64	2335.46
8.00	8.00	65.00	10.00	108.61	0.88	0.64	6.10	31.28	5213.26
8.00	8.00	80.00	10.00	140.21	0.89	0.61	7.63	42.38	2917.88
8.00	8.00	40.00	30.00	146.11	0.88	0.69	8.87	16.11	3474.84
8.00	8.00	60.00	30.00	142.79	0.88	0.69	8.61	12.17	3429.68
8.00	8.00	80.00	30.00	139.46	0.88	0.70	8.59	10.56	3778.95

Bibliography

[1] Max Roser Hannah Ritchie and Pablo Rosado. Energy. *Our World in Data*, 2020. https://ourworldindata.org/energy.

[2] Donald Neamen. *Semiconductor Physics And Devices*. McGraw-Hill, Inc., USA, 3 edition, 2002. ISBN 0072321075.

[3] Arno Smets, Klaus Jäger, Olindo Isabella, René van Swaaij, and Miro Zeman. *Solar Energy: The physics and engineering of photovoltaic conversion, technologies and systems*. UIT Cambridge Limited, 2016. ISBN 978-1-906860-32-5.

[4] Jose Ramos, J.J. Campayo, Ekaitz Zulueta, Oscar Barambones, Pablo Eguia, and I. Zamora. Obtaining the characteristics curves of a photocell by different methods. *Renewable Energy and Power Quality Journal*, pages 814–819, 03 2013. doi: 10.24084/repqj11.455.

[5] Sonya Calnan, H. Uphadhyaya, Stephan Buecheler, G Khrypunov, A Chirila, Alessandro Romeo, R Hashimoto, T Nakada, and A. Tiwari. Application of high mobility transparent conductors to enhance long wavelength transparency of the intermediate solar cell in multi-junction solar cells. *Thin Solid Films*, 517, 12 2008. doi: 10.1016/j.tsf.2008.11.007.

[6] S. Guha, J. Yang, and B. Yan. Amorphous and nanocrystalline silicon solar cells and modules, 2016.

[7] A.V Shah, J Meier, E Vallat-Sauvain, N Wyrsch, U Kroll, C Droz, and U Graf. Material and solar cell research in microcrystalline silicon. *Solar Energy Materials and Solar Cells*, 78(1): 469–491, 2003. ISSN 0927-0248. doi: https://doi.org/10.1016/S0927-0248(02)00448-8. URL `https://www.sciencedirect.com/science/article/pii/S0927024802004488`. Critical review of amorphous and microcrystalline silicon materials and solar cells.

[8] Babal.P. Doped nanocrystalline silicon oxide for use as (intermediate) reflecting layers in thin-film silicon solar cells, 2014.

[9] Pedro Hierrezuelo-Cardet, Anderzon F. Palechor-Ocampo, Jorge Caram, Federico Ventosinos, Daniel Pérez-del Rey, Henk J. Bolink, and Javier A. Schmidt. External quantum efficiency measurements used to study the stability of differently deposited perovskite solar cells. *Journal of Applied Physics*, 127(23):235501, 2020. doi: 10.1063/5.0011503. URL `https://doi.org/10.1063/5.0011503`.

[10] Sma-Air Ritchie, Raymond J. and Suhailar. Using integrating sphere spectrophotometry in unicellular algal research. *Journal of Applied Phycology*, 32, 2020. ISSN 1573-5176. doi: https://doi.org/10.1007/s10811-020-02232-y.

[11] J. Burdick and T. Glatfelter. Spectral response and i-v measurements of tandem amorphous-silicon alloy solar cells, Sep 1986.

[12] Ronald Lee. The outlook for population growth. *Science*, 333(6042):569–573, 2011. doi: 10.1126/science.1208859. URL `https://www.science.org/doi/abs/10.1126/science.1208859`.

[13] J. Lelieveld, K. Klingmüller, A. Pozzer, R. T. Burnett, A. Haines, and V. Ramanathan. Effects of fossil fuel and total anthropogenic emission removal on public health and climate. *Proceedings of the National Academy of Sciences*, 116(15):7192–7197, 2019. doi: 10.1073/pnas.1819989116. URL https://www.pnas.org/doi/abs/10.1073/pnas.1819989116.

[14] Loiy Al-Ghussain. Global warming: review on driving forces and mitigation. *Environmental Progress & Sustainable Energy*, 38(1):13–21, 2019. doi: https://doi.org/10.1002/ep.13041. URL https://aiche.onlinelibrary.wiley.com/doi/abs/10.1002/ep.13041.

[15] Valery P. Oktyabrskiy. A new opinion of the greenhouse effect. *St. Petersburg Polytechnical University Journal: Physics and Mathematics*, 2(2):124–126, 2016. ISSN 2405-7223. doi: https://doi.org/10.1016/j.spjpm.2016.05.008. URL https://www.sciencedirect.com/science/article/pii/S2405722316300779.

[16] Umair Shahzad. The need for renewable energy sources. *International Journal of Information Technology and Electrical Engineering*, 2012. ISSN 2306-708X.

[17] A. Demirbas. Global renewable energy projections. *Energy Sources, Part B: Economics, Planning, and Policy*, 4(2):212–224, 2009. doi: 10.1080/15567240701620499. URL https://doi.org/10.1080/15567240701620499.

[18] Roger G. Little and Michael J. Nowlan. Crystalline silicon photovoltaics: the hurdle for thin films. *Progress in Photovoltaics: Research and Applications*, 5(5):309–315, 1997. doi: https://doi.org/10.1002/(SICI)1099-159X(199709/10)5:5<309::AID-PIP180>3.0.CO;2-X.

[19] Mohd Arbaz, Ujjwal Tyagi , Eswara Prasad. Thin-film solar cell market outlook - 2030, 2022. URL https://www.alliedmarketresearch.com/thin-film-solar-cell-market/.

[20] A. Shah, P. Torres, R. Tscharner, N. Wyrsch, and H. Keppner. Photovoltaic technology: The case for thin-film solar cells. *Science*, 285(5428):692–698, 1999. doi: 10.1126/science.285.5428.692. URL https://www.science.org/doi/abs/10.1126/science.285.5428.692.

[21] Jeyakumar Ramanujam and Udai P. Singh. Copper indium gallium selenide based solar cells – a review. *Energy Environ. Sci.*, 10:1306–1319, 2017. doi: 10.1039/C7EE00826K. URL http://dx.doi.org/10.1039/C7EE00826K.

[22] Hossein Movla. Optimization of the cigs based thin film solar cells: Numerical simulation and analysis. *Optik*, 125(1):67–70, 2014. ISSN 0030-4026. doi: https://doi.org/10.1016/j.ijleo.2013.06.034. URL https://www.sciencedirect.com/science/article/pii/S0030402613008917.

[23] A. Shah, P. Torres, R. Tscharner, N. Wyrsch, and H. Keppner. Photovoltaic technology: The case for thin-film solar cells. *Science*, 285(5428):692–698, 1999. doi: 10.1126/science.285.5428.692. URL https://www.science.org/doi/abs/10.1126/science.285.5428.692.

[24] Arvind Shah. Thin-film silicon solar cells, edited by arvind shah and published in 2010 by the epfl press, lausanne [1], with contributions by horst schade and friedhelm finger. for further specialized study and for details, the reader is referred to this book. pages 235–307, 2018. doi: https://doi.org/10.1016/B978-0-12-809921-6.00008-2. URL https://www.sciencedirect.com/science/article/pii/B9780128099216000082.

[25] Hyet solar, flexible light weight modules, 2022. URL https://www.hyetsolar.com/.

[26] Subhendu Guha, Jeffrey Yang, and Baojie Yan. High efficiency multi-junction thin film silicon cells incorporating nanocrystalline silicon. *Solar Energy Materials and Solar Cells*, 119:1–11, 2013. ISSN 0927-0248. doi: https://doi.org/10.1016/j.solmat.2013.03.036. URL https://www.sciencedirect.com/science/article/pii/S0927024813001499. Thin-film Photovoltaic Solar Cells.

[27] Hairen Tan, Etienne Moulin, Fai Tong Si, Jan-Willem Schüttauf, Michael Stuckelberger, Olindo Isabella, Franz-Josef Haug, Christophe Ballif, Miro Zeman, Arno H. M. Smets, and et al. Highly transparent modulated surface textured front electrodes for high-efficiency multijunction thin-film silicon solar cells, Jun 2015. URL https://onlinelibrary.wiley.com/doi/10.1002/pip.2639.

[28] Soohyun Kim, Jin-Won Chung, Hyun Lee, Jinhee Park, Younho Heo, and Heon-Min Lee. Remarkable progress in thin-film silicon solar cells using high-efficiency triple-junction technology. *Solar Energy Materials and Solar Cells*, 119:26–35, 2013. ISSN 0927-0248. doi: https://doi.org/10.1016/j.solmat.2013.04.016. URL https://www.sciencedirect.com/science/article/pii/S0927024813001876. Thin-film Photovoltaic Solar Cells.

[29] Martin Python, Evelyne Vallat-Sauvain, Julien Bailat, Didier Dominé, Luc Fesquet, Arvind Shah, and Christophe Ballif. Relation between substrate surface morphology and microcrystalline silicon solar cell performance. *Journal of Non-Crystalline Solids*, 354(19):2258–2262, 2008. ISSN 0022-3093. doi: https://doi.org/10.1016/j.jnoncrysol.2007.09.084. URL https://www.sciencedirect.com/science/article/pii/S0022309307014160. Amorphous and Nanocrystalline Semiconductors.

[30] O Kluth, B Rech, L Houben, S Wieder, G Schöpe, C Beneking, H Wagner, A Löffl, and H.W Schock. Texture etched zno:al coated glass substrates for silicon based thin film solar cells. *Thin Solid Films*, 351(1):247–253, 1999. ISSN 0040-6090. doi: https://doi.org/10.1016/S0040-6090(99)00085-1. URL https://www.sciencedirect.com/science/article/pii/S0040609099000851.

[31] Thierry Vrijer and Arno Smets. Advanced textured monocrystalline silicon substrates with high optical scattering yields and low electrical recombination losses for supporting crack-free nano- to poly-crystalline film growth. *Energy Science Engineering*, 9, 03 2021. doi: 10.1002/ese3.873.

[32] Hitoshi () Sai, Kimihiko () Saito, and Michio () Kondo. Enhanced photocurrent and conversion efficiency in thin-film microcrystalline silicon solar cells using periodically textured back reflectors with hexagonal dimple arrays. *Applied Physics Letters*, 101(17):173901, 2012. doi: 10.1063/1.4761956. URL https://doi.org/10.1063/1.4761956.

[33] Hitoshi ( ) Sai, Kimihiko ( ) Saito, Nana () Hozuki, and Michio ( ) Kondo. Relationship between the cell thickness and the optimum period of textured back reflectors in thin-film microcrystalline silicon solar cells. *Applied Physics Letters*, 102(5):053509, 2013. doi: 10.1063/1.4790642. URL https://doi.org/10.1063/1.4790642.

[34] Ping-Kuan Chang, Fu-Ji Tsai, Chun-Hsiung Lu, Chih-Hung Yeh, Na-Fu Wang, and Mau-Phon Houng. Improvement of azo/p-a-sic:h contact by the p-c-si:h insertion layer and its application to a-si:h solar cells. *Solid-State Electronics*, 72:48–51, 2012. ISSN 0038-1101. doi: https://doi.org/10.1016/j.sse.2012.01.002. URL https://www.sciencedirect.com/science/article/pii/S0038110112000044.

[35] Hairen Tan, Pavel Babal, Miro Zeman, and Arno H.M. Smets. Wide bandgap p-type nanocrystalline silicon oxide as window layer for high performance thin-film silicon multi-junction solar cells. *Solar Energy Materials and Solar Cells*, 132:597–605, 2015. ISSN 0927-0248. doi: https://doi.org/10.1016/j.solmat.2014.10.020. URL https://www.sciencedirect.com/science/article/pii/S0927024814005510.

[36] Arup Dasgupta, Andreas Lambertz, O. Vetterl, F. Finger, R. Carius, U. Zastrow, and H. Wagner. P-layers of microcrystalline silicon thin film solar cells. *Proceedings of the 16th European Photovoltaic Solar Energy Conference*, pages 557–560, 01 2000.

[37] Ping-Kuan Chang, Fu-Ji Tsai, Chun-Hsiung Lu, Chih-Hung Yeh, Na-Fu Wang, and Mau-Phon Houng. Improvement of azo/p-a-sic:h contact by the p-c-si:h insertion layer and its application to a-si:h solar cells. *Solid-State Electronics*, 72:48–51, 2012. ISSN 0038-1101. doi: https://doi.org/10.1016/j.sse.2012.01.002. URL https://www.sciencedirect.com/science/article/pii/S0038110112000044.

[38] Thierry de Vrijer, David van Nijen, Harsh Parasramka, Paul A. Procel Moya, Yifeng Zhao, Olindo Isabella, and Arno H.M. Smets. The fundamental operation mechanisms of nc-siox0:h based tunnel recombination junctions revealed. *Solar Energy Materials Solar Cells*, 236, 2022. ISSN 0927-0248. doi: 10.1016/j.solmat.2021.111501.

[39] Thierry de Vrijer, Fai Tong Si, Hairen Tan, and Arno H.M. Smets. Chemical stability and performance of doped silicon oxide layers for use in thin film silicon solar cells. In *2018 IEEE 7th World Conference on Photovoltaic Energy Conversion (WCPEC) (A Joint Conference of 45th IEEE PVSC, 28th PVSEC 34th EU PVSEC)*, pages 3477–3480, 2018. doi: 10.1109/PVSC.2018.8548192.

[40] Thierry de Vrijer and Arno H.M. Smets. The relation between precursor gas flows,thickness dependent material phases, andopto-electrical properties of dopeda/nc-siox0:h films. *IEEE Journal of Photovoltaics*, 11(3):591–599, 2021. ISSN 2156-3381. doi: 10.1109/JPHOTOV.2021.3059940.

[41] Soohyun Kim, Hongcheol Lee, Jin-Won Chung, Seh-Won Ahn, and Heon-Min Lee. n-type microcrystalline silicon oxide layer and its application to high-performance back reflectors in thin-film silicon solar cells. *Current Applied Physics*, 13(4):743–747, 2013. ISSN 1567-1739. doi: https://doi.org/10.1016/j.cap.2012.11.017. URL https://www.sciencedirect.com/science/article/pii/S1567173912004646.

[42] K. Sriprapha, C. Piromjit, A. Limmanee, and J. Sritharathikhun. Development of thin film amorphous silicon oxide/microcrystalline silicon double-junction solar cells and their temperature dependence. *Solar Energy Materials and Solar Cells*, 95(1):115–118, 2011. ISSN 0927-0248. doi: https://doi.org/10.1016/j.solmat.2010.05.010. URL https://www.sciencedirect.com/science/article/pii/S0927024810002928. 19th International Photovoltaic Science and Engineering Conference and Exhibition (PVSEC-19) Jeju, Korea, 9-13 November 2009.

[43] P. Buehlmann, J. Bailat, D. Dominé, A. Billet, F. Meillaud, A. Feltrin, and C. Ballif. In situ silicon oxide based intermediate reflector for thin-film silicon micromorph solar cells. *Applied Physics Letters*, 91(14):143505, 2007. doi: 10.1063/1.2794423. URL https://doi.org/10.1063/1.2794423.

[44] Tadatsugu Minami. Transparent conducting oxide semiconductors for transparent electrodes. *Semiconductor Science and Technology*, 20(4):S35–S44, mar 2005. doi: 10.1088/0268-1242/20/4/004. URL https://doi.org/10.1088/0268-1242/20/4/004.

[45] Xunming Deng. Eric A. Schiff. Amorphous silicon based solar cells. 97:505 – 565. doi: 10.1063/1.3488023.

[46] W.E. Spear and P.G. Le Comber. Substitutional doping of amorphous silicon. *Solid State Communications*, 17(9):1193–1196, 1975. ISSN 0038-1098. doi: https://doi.org/10.1016/0038-1098(75)90284-7. URL https://www.sciencedirect.com/science/article/pii/0038109875902847.

[47] Guha. Substitutional doping of amorphous silicon. *Applied physics*, 2(9):859, 1981.

[48] D. L. Staebler and C. R. Wronski. Reversible conductivity changes in discharge-produced amorphous si. *Applied Physics Letters*, 31(4):292–294, 1977. doi: 10.1063/1.89674. URL https://doi.org/10.1063/1.89674.

[49] Xiaojing Liu, Wei Zi, and Shengzhong (Frank) Liu. p-layer bandgap engineering for high efficiency thin film silicon solar cells. *Materials Science in Semiconductor Processing*, 39:192–199, 2015. ISSN 1369-8001. doi: https://doi.org/10.1016/j.mssp.2015.04.011. URL https://www.sciencedirect.com/science/article/pii/S1369800115002632.

[50] J. Meier, S. Dubail, R. Platz, P. Torres, U. Kroll, J.A. Anna Selvan, N. Pellaton Vaucher, Ch. Hof, D. Fischer, H. Keppner, R. Flückiger, A. Shah, V. Shklover, and K.-D. Ufert. Towards high-efficiency thin-film silicon solar cells with the "micromorph" concept. *Solar Energy Materials and Solar Cells*, 49(1):35–44, 1997. ISSN 0927-0248. doi: https://doi.org/10.1016/S0927-0248(97)00173-6. URL https://www.sciencedirect.com/science/article/pii/S0927024897001736.

[51] M.Z. Farah Khaleda, B. Vengadaesvaran, and N.A. Rahim. Chapter 18 - spectral response and quantum efficiency evaluation of solar cells: a review. In S.J. Dhoble, N.Thejo Kalyani, B. Vengadaesvaran, and Abdul Kariem Arof, editors, *Energy Materials*, pages 525–566. Elsevier, 2021. ISBN 978-0-12-823710-6. doi: https://doi.org/10.1016/B978-0-12-823710-6.00014-5. URL https://www.sciencedirect.com/science/article/pii/B9780128237106000145.

[52] Hitoshi () Sai and Michio () Kondo. Effect of self-orderly textured back reflectors on light trapping in thin-film microcrystalline silicon solar cells. *Journal of Applied Physics*, 105(9):094511, 2009. doi: 10.1063/1.3108689. URL https://doi.org/10.1063/1.3108689.

[53] E. Manea, E. Budianu, M. Purica, D. Cristea, I. Cernica, R. Muller, and V. Moagar Poladian. Optimization of front surface texturing processes for high-efficiency silicon solar cells. *Solar Energy Materials and Solar Cells*, 87(1):423–431, 2005. ISSN 0927-0248. doi: https://doi.org/10.1016/j.solmat.2004.06.013. URL https://www.sciencedirect.com/science/article/pii/S0927024804003605. International Conference on Physics, Chemistry and Engineering.

[54] Joseph Burdick and Troy Glatfelter. Spectral response and i–v measurements of tandem amorphous-silicon alloy solar cells. *Solar Cells*, 18(3):301–314, 1986. ISSN 0379-6787. doi: https://doi.org/10.1016/0379-6787(86)90129-8. URL https://www.sciencedirect.com/science/article/pii/0379678786901298.

[55] Karin Söderström, Grégory Bugnon, Rémi Biron, Céline Pahud, Fanny Meillaud, Franz-Josef Haug, and Christophe Ballif. Thin-film silicon triple-junction solar cell with 12.5% stable efficiency on innovative flat light-scattering substrate. *Journal of Applied Physics*, 112(11):114503, 2012. doi: 10.1063/1.4768272. URL https://doi.org/10.1063/1.4768272.

[56] Fai Tong Si, Olindo Isabella, and Miro Zeman. Artifact interpretation of spectral response measurements on two-terminal multijunction solar cells. *Advanced Energy Materials*, 7(6):1601930, 2017. doi: https://doi.org/10.1002/aenm.201601930. URL https://onlinelibrary.wiley.com/doi/abs/10.1002/aenm.201601930.

[57] A. Belfar and H. Aït-Kaci. Effect of incorporating p-type hydrogenated nanocrystalline silicon buffer layer on amorphous silicon n–i–p solar cell performances. *Thin Solid Films*, 525:167–171, 2012. ISSN 0040-6090. doi: https://doi.org/10.1016/j.tsf.2012.10.060. URL https://www.sciencedirect.com/science/article/pii/S0040609012013302.

[58] Rémi Biron, Celine Pahud, Franz-Josef Haug, Jordi Escarré, Karin Söderström, and Christophe Ballif. Window layer with p doped silicon oxide for high voc thin-film silicon n-i-p solar cells. *Journal of Applied Physics*, 110(12):124511, 2011. doi: 10.1063/1.3669389. URL https://doi.org/10.1063/1.3669389.

[59] C Beneking, B Rech, S Wieder, O Kluth, H Wagner, W Frammelsberger, R Geyer, P Lechner, H Rübel, and H Schade. Recent developments of silicon thin film solar cells on glass substrates. *Thin Solid Films*, 351(1):241–246, 1999. ISSN 0040-6090. doi: https://doi.org/10.1016/S0040-6090(98)01793-3. URL https://www.sciencedirect.com/science/article/pii/S0040609098017933.

[60] J. Hüpkes, B. Rech, O. Kluth, T. Repmann, B. Zwaygardt, J. Müller, R. Drese, and M. Wuttig. Surface textured mf-sputtered zno films for microcrystalline silicon-based thin-film solar cells. *Solar Energy Materials and Solar Cells*, 90(18):3054–3060, 2006. ISSN 0927-0248. doi: https://doi.org/10.1016/j.solmat.2006.06.027. URL https://www.sciencedirect.com/science/article/pii/S0927024806002170. 14th International Photovoltaic Science and Engineering Conference.

[61] Klaus Jäger, Dane Linssen, Olindo Isabella, and Miro Zeman. Optimized nano-textured interfaces for thin-film silicon solar cells: Identifying the limit of randomly textured interfaces. volume 9140, 04 2014. doi: 10.1117/12.2057596.

[62] Akiharu Morimoto, Minoru Matsumoto, Masahiro Yoshita, Minoru Kumeda, and Tatsuo Shimizu. Doping effect of oxygen or nitrogen impurity in hydrogenated amorphous silicon films. *Applied Physics Letters*, 59(17):2130–2132, 1991. doi: 10.1063/1.106102. URL https://doi.org/10.1063/1.106102.